THE INCIDENCE OF POLAR RING GALAXIES IN WALLABY PILOT FIELDS

L'INCIDENCE DES GALAXIES À ANNEAU POLAIRE DANS LES CHAMPS PILOTES WALLABY

A Thesis Submitted to the Division of Graduate Studies
of the Royal Military College of Canada
by

Reanna L. Palleske, BEng
Second Lieutenant

In Partial Fulfillment of the Requirements for the Degree of
Master of Science in Physics

May, 2023

To Megatron & Grimlock

Acknowledgements

I would like to first express my gratitude to my incredible supervisor and mentor, Dr. Kristine Spekkens, for her guidance and patience while I explored the field of space science. I'd also like to thank Dr. Nathan Deg for tirelessly answering my questions about complex programs and offering his advice whenever my code malfunctioned. On a personal note, I would like to acknowledge the unwavering support of my parents, Cyndy and Loring, as well as my siblings, Rowan, Gaelen, and Saige. Finally, I would like to thank Jessica Perigo, Elizabeth Ricker, Brianna Lane, Mina Lee, Avery Stover, and all of my other close friends for their constant encouragement and unshakeable faith in my academic competence.

All members of the WALLABY survey include the following acknowledgement in their work: This scientific work uses data obtained from Inyarrimanha Ilgari Bundara / the Murchison Radio-astronomy Observatory. We acknowledge the Wajarri Yamaji People as the Traditional Owners and native title holders of the Observatory site. The Australian SKA Pathfinder (ASKAP) is part of the Australia Telescope National Facility (https://ror.org/05qajvd42) which is managed by the Commonwealth Scientific and Industrial Research Organisation (CSIRO). Operation of ASKAP is funded by the Australian Government with support from the National Collaborative Research Infrastructure Strategy. ASKAP uses the resources of the Pawsey Supercomputing Centre. Establishment of ASKAP, the Murchison Radio-astronomy Observatory and the Pawsey Supercomputing Centre are initiatives of the Australian Government, with support from the Government of Western Australia and the Science and Industry Endowment Fund.

Statement of Co-Authorship

The data analyses and results included in Chapter 5 were entirely the work of the author.

The work conducted in Chapter 3 was collaborative with the authors of Deg et al. (2023), "WALLABY Pilot Survey: The Potential Polar Ring Galaxies NGC 4632 and NGC 6156" *Monthly Notices of the Royal Astronomical Society, in Press.* The two polar ring galaxy candidates found in WALLABY Public Data Release 1 were discovered by Dr. Nathan Deg. The tilted ring best fit models of NGC 4632 and NGC 6156 were created by Dr. Nathan Deg. In addition, the matrix formalism presented in Chapter 4 that was used to project polar ring galaxies into the sky plane was first derived by Dr. Nathan Deg. Further information regarding related analyses can be found in Chapters 3 and 4, as well as in Deg et al. (2023).

Abstract

Polar ring galaxies with two distinct atomic gas (HI) components are some of the most unique objects in the local Universe, but their rarity remains difficult to ascertain. This thesis presents an investigation of polar ring galaxy detectability, using detections from the pilot phase of the Widefield ASKAP L-band Legacy All-sky Blind surveY (WALLABY) on the Australian SKA Pathfinder (ASKAP) telescope. This analysis used HI detections in conjunction with mock data cubes, created to model a variety of observation conditions, to estimate the universal incidence of polar ring galaxies. Kinematic models of two polar ring galaxy candidates from WALLABY's Public Data Release 1 (PDR1) were projected at different orientations and resolutions to constrain the incidence of polar ring galaxies from detection statistics. The morphology and kinematics of Public Data Release 2 (PDR2) detections were then studied to determine which among them showed signs of these gaseous misalignments. Three potential polar ring galaxies were identified in PDR2, which implied an overall incidence of $\sim$1.5%, consistent with the estimate made using PDR1 data alone. These results suggest that gas-rich polar ring galaxies could be significantly more common in the local Universe than previously estimated.

Résumé

Les galaxies à anneau polaire avec deux composantes distinctes de gaz atomique (HI) sont parmi les objets les plus uniques de l'univers local, mais leur rareté reste difficile à déterminer. Cette thèse présente une étude de la détectabilité des galaxies à anneau polaire, en utilisant les détections de la phase pilote du ≪Widefield ASKAP L-band Legacy All-sky Blind surveY≫ (WALLABY) sur le télescope australien SKA Pathfinder (ASKAP). Cette analyse a utilisé des détections HI en conjonction avec des cubes de données fictifs, créés pour modéliser une variété de conditions d'observation, afin d'estimer l'incidence universelle des galaxies à anneau polaires. Les modèles cinématiques de deux candidats de galaxies à anneau polaire de la Publication de Données Publiques 1 (PDR1) de WALLABY ont été projetés à différentes orientations et résolutions pour estimer l'incidence des galaxies à anneau polaire à partir des statistiques de détection. La morphologie et la cinématique des détections de la Publication de Données Publiques 2 (PDR2) ont ensuite été étudiées pour déterminer lesquelles d'entre elles présentaient des signes de ces désalignements gazeux. Trois galaxies à anneau polaire potentielles ont été identifiées dans PDR2, ce qui impliquait une incidence globale d'environ 1,5%, qui correspond à l'estimation faite en utilisant uniquement les données de PDR1. Ces résultats suggèrent que les galaxies à anneau polaire riches en gaz pourraient être beaucoup plus fréquentes dans l'univers local qu'en était estimé auparavant.

Contents

List of Figures

List of Tables

List of Abbreviations

Abbreviation	Definition
ASKAP	Australian Square Kilometre Array Pathfinder
BA	Beams Across
HI	Atomic Neutral Hydrogen
MCG	MockCubeGenerator
Mom0	Moment Zero
Mom1	Moment One
PAF	Phased-Array Feed
PDR	Public Data Release
PRG	Polar Ring Galaxy
RA	Right Ascension
SDSS	Sloan Digital Sky Survey
S/N	Signal-to-Noise Ratio
W1255	WALLABY J125548+041805 (NGC 4808)
W1300	WALLABY J130056-135640 (NGC 4899)
W1309	WALLABY J130943-163617
WALLABY	Widefield ASKAP L-Band Legacy All-sky Blind surveY

List of Variables

Variable	Definition	Units
α	Orientation of the Ring Relative to the Galaxy	degrees
β	Ring Orientation Angle	degrees
ϕ	Vertical Angle Between Ring's Major Axis and Galaxy Plane	degrees
ρ_{HI}	HI Density	$M_\odot/pc^2$
Σ_b	Summation Across Resolution Bins	
θ (Equation 2.1)	Cylindrical Coordinate Relative to Major Axis	degrees
$\theta_{g/r}$	Main Disk (g)/Polar Ring (r) Position Angle ($PA_{g/r}$ + 90°)	degrees
c	Cosine Function	
D_f	Detectability Fraction	
f	Initial to Final Ring Radius Fraction	
f_i	Gas-Rich PRG Incidence Estimate	
i	Inclination	degrees
N_b	Number of Elements in Resolution Bin	
$N_{detected}$	Number of PRGs Detected in Data Set	
PA	Position Angle	degrees
r_{mid}	Distance Between Ring and Galaxy's Centre	arcsec
R_{out}	Distance Between Outer Ring and Galaxy's Centre	arcsec
R_{out_i}	Initial Outer Ring Radius	arcsec
r_{wid}	Lateral Width of the Ring	arcsec
$R_{x/y/z}$	Rotation About x/y/z Axes	
res	Resolution	BA
s	Sine Function	
t	Tan Function	
V_{LOS}	Line of Sight Velocity	km/s
V_{rot}	Rotational Velocity	km/s
V_{sys}	Systemic Velocity	km/s
$\mathbf{x_{s/g/r}}$	Sky (s), Galaxy (g), or Ring (r) Plane Coordinates	
z	Redshift	

1 Introduction

Polar ring galaxies (PRGs) are unusual systems that have a ring of gas, stars, and dust rotating in a plane perpendicular to the galaxy's main body. Polar disk galaxies are the same concept applied to a disk of orthogonally rotating material, rather than a ring. The only difference between the two is the lateral thickness of the polar component and the size of the gap between the displaced gas and the main galaxy body. Examples of both polar structures are included in Figure 1.1. Both polar rings and polar disks must be rotating in a plane offset from that of the galactic disk by an angle very near to 90° in order to be considered stable. Kinematically misaligned components with planes of rotation too close to the main galaxy body are in an unstable, transitioning state. The misaligned component will eventually be torqued to align with the angular momentum generated by the primary plane of rotation, assimilating its axis to align with the rest of the galaxy's matter. In Figure 1.1, NGC 4650a is likely stable while the lower offset angle of NGC 660's polar ring may indicate the beginning stages of transition.

It has been theorized that polar rings/disks are part of an evolutionary sequence that leads to warped disks (Brook et al., 2008; Combes, 2006), and that all symmetrical kinematically misaligned components likely have similar origins. This theory essentially means that polar rings slowly transition to align with the galaxy, eventually forming an extreme warp in the main galaxy disk rather than a separate ring/disk component. Then it assimilates further, becoming only a slight warp, before conforming entirely with the main galactic disk. Warped disks are kinematically misaligned gaseous components that exhibit a smooth transition from the main galaxy body to its plane of rotation, whereas polar disks have a clear and distinct discontinuity between the components.

There are no confirmed formation methods for galaxies with polar structures. Due to their rarity (Reshetnikov et al., 2011) and variety, it is difficult to categorize all PRGs into a single method of creation. Some theories posit that they form through cold gas accretion from the surrounding intergalactic

(a) (b)

Figure 1.1: Comparative example of a polar ring galaxy (a) and a polar disk galaxy (b). The polar ring galaxy, NGC 660 (Rector, 2014), displays more space between the polar component and the main galaxy body than the polar disk galaxy, NGC 4650a (Laustsen and West, 1980). The polar disk appears to be offset from the main galaxy body by nearly 90° while the polar ring appears to be slightly less perpendicular.

medium (Brook et al., 2008; Spavone et al., 2011; Snaith et al., 2012; Macciò et al., 2006; Stanonik et al., 2009), the same way the main galaxy body was formed. These theories are supported by cosmological simulations (Brook et al., 2008; Macciò et al., 2006) and have gained traction more recently than those regarding galactic interactions. In the context of polar structure formation mechanisms, the galactic interactions deemed most plausible are the tidal

stripping of material from a passing galaxy or a galaxy collision (Schweizer et al., 1983; Taniguchi et al., 1990; Reshetnikov et al., 1996). Tidal stripping occurs when the gravity of a larger galaxy pulls the matter from a second galaxy or object because of the differential force at the object's edge relative to its centre. If this object, for example a small galaxy infalling into a larger one, were to be passing the other over its poles, the tidally stripped material could begin its orbit of the galactic centre in an entirely different plane. The collision of two galaxies could also create a polar structure through an orthogonal collision (Bekki, 1998). A smaller galaxy colliding with a larger one at a near-90 degree offset could manifest in the larger galaxy as a polar disk in itself. Each PRG discovered provides further insight into potential formation theories, making it an ever-changing field of study.

There are three general classes of kinematic misalignments in galaxies: gas-star misalignments, star-star misalignments, and gas-gas misalignments. The vast majority of detected misalignments are between the main stellar body of a galaxy and an offset gaseous component. The next most common form of misalignments are between two stellar components, but even these have an incidence of only $\sim$2% (Cao et al., 2022). The third type of kinematic misalignment does not have an established incidence estimate because there is less available data on gas-gas displacements, but the most recent literature value is $\sim$0.1% (Reshetnikov et al., 2011). Estimating the incidence of gas-gas polar misalignments is a focus of this thesis.

An effective way to explain PRGs is through the use of canonical examples. Figure 1.1b shows a Hubble Space Telescope image of NGC 4650a. This image depicts the morphology of a typical PRG, although it would be classified as a star-star, or gas-star, misalignment due to the age and depletion of the main galaxy body. NGC 660, shown in Figure 1.1a, is a better representation of a gas-gas misalignment due to the relatively gas-rich main body (Van Driel et al., 1995). Technically, NGC 4650a is a polar disk galaxy, but it displays a near-orthogonal plane of rotation that is not replicated by NGC 660. NGC 4650a also provides evidence in support of the theory that polar components are not formed at the same time as the rest of the galaxy (Bournaud and Combes, 2003). Some astronomers believe that when a galaxy forms, it could accrete cold gas from the intergalactic medium both in its main galactic plane as well as in a polar configuration. Since PRGs exist in a variety of forms and each possess their own unique qualities, it is difficult to disprove any theory entirely. However, NGC 4650a clearly demonstrates that at least not all polar components are formed during the galaxy's birth. As can be seen in Figure 1.1b, the main galaxy body is a faded, orange and yellow lenticular galaxy. There is very little gas, dust, or newer blue stars to be found. The polar disk,

conversely, contains a plethora of gas and very many blue stars. This indicates that the polar disk was formed much later in the galaxy's evolution than the main body, and was thus accreted over time or created through some form of galaxy interaction that occurred separately from its original formation.

The difficulty with observing and identifying gas-rich PRGs is that the observation conditions can easily mask the presence of the polar component. Limited spatial resolution alone is capable of completely obscuring the misalignment in both the morphological and kinematic maps, to a degree that will be investigated further throughout this thesis. Resolution in extragalactic radio astronomy can be measured in terms of the number of beams across (BA), which is the number of telescope resolution elements that can fit edge-to-edge across the major axis of an observed object. The more beams that can fit, the more detail can be observed. An object observed at 10 BA is considered very well resolved, while an object observed at 3 BA is considered to be poorly resolved.

The sky projection of both the main body and the polar ring can also pose a challenge to the identification of gas-rich PRGs. Throughout this thesis, the detectability of the polar component was examined when the inclination and position angle of the main galaxy were projected differently on the sky. The inclination refers to the angle between the edge of the galaxy and the line-of-sight of the observer. An inclination of 0° corresponds to a face-on galaxy, and an inclination of 90° corresponds to an edge-on galaxy (from the perspective of the observer). The position angle refers to the angle between the galaxy's major axis and the north celestial pole. Essentially, the position angle indicates the galaxy's orientation on the sky.

Figure 1.2 depicts a rendition of one of the gas-rich PRG candidates that was discovered during the first pilot phase of the WALLABY survey that is underway on the Australian SKA Pathfinder telescope (see Figure 1.3). The optical component is the main galaxy body, and the ring that was detected in the radio regime was superimposed over the image to demonstrate the orientation. The optical image of the main galaxy indicates that NGC 4632 is a spiral galaxy with many blue-shaded star forming regions. This means that there is still gas being converted into stars within the main disk (the associated atomic neutral Hydrogen (HI) is not shown in Figure 1.2), classifying this galaxy as a gas-rich PRG or a gas-gas polar misalignment.

In order to identify gaseous polar rings, the HI morphology and kinematics of galaxy observations had to be studied. Some radio astronomers focus their studies on the neutral Hydrogen present within an object, or the 21-cm HI line. This is a common radio wavelength for astronomers to observe due to the "spin-flip" transition: the atomic transition of electrons between two hyperfine

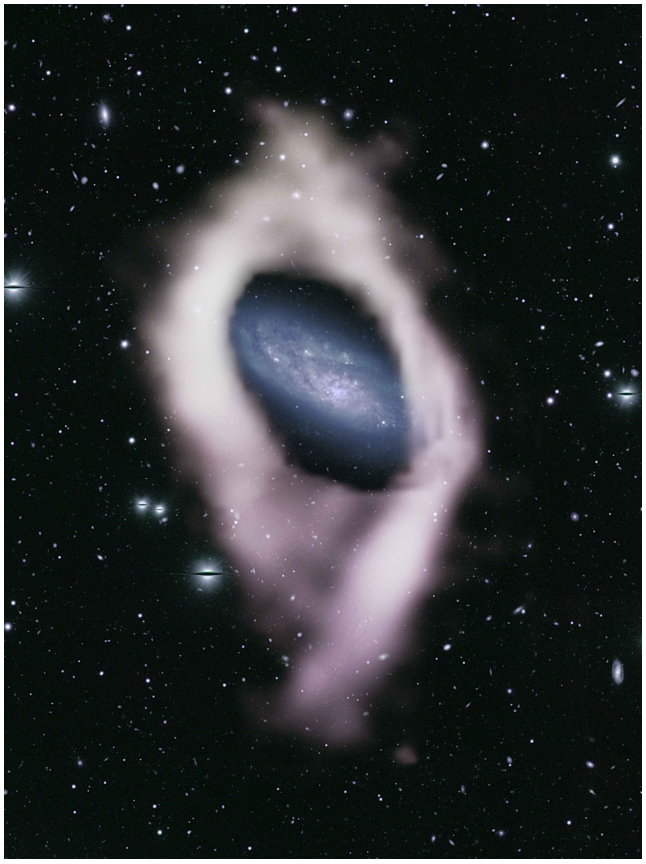

Figure 1.2: A composite g, r, and z-band image of NGC 4632 from the Hyper Suprime-Cam Subaru Strategic Program (HSC-SSP, Aihara et al. (2018)) overlayed with its HI polar component. The trend in the HI towards purple denotes relatively blueshifted gas (near the bottom) and the trend towards yellow denotes redshifted gas (near the top). The misaligned HI gas clearly has a different orientation from that of the main galaxy body. This figure was created for the first public data release PRG research paper; Deg et al. (2023).

levels of the atom's ground state. This transition emits electromagnetic energy that can be observed from large distances. The "spin-flip" transition happens relatively rarely, however there is such a large quantity of atomic gas in galaxies that it becomes a reliable method of observation. The research conducted in this thesis used atomic hydrogen observations from a radio telescope array located in Western Australia.

Radio astronomy is the observation of electromagnetic radiation emitted

by objects across the Universe on frequencies between 10 MHz and 300 MHz (Marr et al., 2016) which corresponds to wavelengths between approximately one and 30 metres. The main differences between optical astronomy and radio astronomy are simply the mechanisms used and the wavelengths being observed. The visible spectrum, for comparison, is on the scale of hundreds of nanometres. The wide range of radio frequencies allowed for the discovery and further study of a variety of astronomical phenomena that had not been available with the much smaller range of visible emissions. Objects too cold to emit light can be observed through spectral-line emission and thermal continuum emission (Marr et al., 2016), which includes the interstellar medium in the Milky Way and other galaxies. The cosmic microwave background does not produce visible light, but it is detectable through the long wavelengths observed by radio astronomers. Supernova remnants and quasars (quasi-stellar radio sources) were able to be studied for the first time through a phenomenon called synchrotron emission, which is also detectable in the radio frequency range. Synchrotron emission is the electromagnetic radiation emitted through accelerated electrons (Ballet, 2006).

Radio astronomy is not in competition with optical astronomy, and one is often used to complement the other. Objects that are faint in the optical spectrum may be well-illuminated in the radio spectrum, allowing for a more in-depth study when the two methods are combined. Radio astronomy offers observations that are complementary to a variety of wavelength regimes, such as X-rays, gamma rays, ultraviolet (UV) light, and infrared (IR) light (Marr et al., 2016). Astronomy at wavelength regimes outside of the radio or visible ranges must be done from space, however, because the atmosphere of the Earth is not transparent to those emissions. Due to the cost of launching telescopes into space and the wide range of wavelengths still observable through radio astronomy, most telescopes are located on the ground (Marr et al., 2016).

Presently, radio astronomy has reached the same level of operation as optical astronomy which allows for astronomers worldwide to utilize a suite of relatively new radio telescopes for their research.

One such radio facility is ASKAP, the Australian Square Kilometre Array (SKA) Pathfinder, a radio telescope array located in a radio quiet zone in Western Australia. ASKAP consists of 36 x 12 metre dishes that are equipped with Phased-Array Feeds (PAFs), a novel technology that increases the interferometer's field of view and is able to achieve extremely high survey speeds (Koribalski et al., 2020). An interferometer, or radio telescope array, is an instrument that uses the interference of radio waves to make precise measurements. This makes ASKAP one of the best instruments in the world for mapping the sky in the radio regime (Hotan, 2022). In the next five years,

Figure 1.3: Image of the Australian Square Kilometre Array Pathfinder located in a radio quiet zone in Western Australia (Hotan, 2022). The radio antennas are able to operate effectively during both the day and night, unlike optical wavelength telescopes.

ASKAP will carry out a host of widefield radio surveys to study objects ranging from our own Milky Way to distant quasars. WALLABY is the largest of those surveys, and stands for the Widefield ASKAP L-Band Legacy All-sky Blind surveY (Koribalski et al., 2020). The WALLABY research team consists of international collaborators that investigate the gathered data for different scientific purposes.

The nature of WALLABY is important to the incidence calculations that were conducted in this study. Having an all-sky untargeted survey meant that no specific galaxies were selected for observation, allowing for a data set that represents the diversity of gas-rich objects in the local Universe. In the context of this thesis, the local Universe extends to redshift z $\sim$0.1. z is the variable for the redshift of radio astronomy detections, where the larger the z value the longer the waves have been travelling towards the observer. This is also a good indication of the object's distance, such that z $\sim$0.1 corresponds to a distance of approximately 1.4 billion light years. Using the Australian SKA Pathfinder to examine and document a microcosm of the Universe provides high quality observations to be assessed and categorized without the bias of expectation. With a targeted study, the galaxies would have had to be chosen

for a reason and likely would have been at higher resolutions. This would have skewed the incidence calculation and altered the results.

Through galaxy modelling, WALLABY data, and statistical extrapolation, this thesis determined the incidence of gas-rich PRGs across the local Universe for the first time. This number was generated from the first phase of the WALLABY pilot survey, and was reinforced when the study was conducted a second time using data from the second phase of the WALLABY pilot survey. Knowing the quantity of these polar kinematic misalignments will allow astronomers to refine formation theories for all types of PRGs, and potentially provide a new perspective from which to study galaxy interactions. The dynamics of gas-gas misalignments could also be used to examine any correlations between the characteristics of a polar component and the galaxy's dark matter halo (Khoperskov et al., 2014a,b; Combes, 2006).

The outline of this thesis is as follows: Chapter 2 presents background information from previous studies that was deemed relevant to the analyses conducted in the following chapters. Chapter 3 discusses the work done by Deg et al. (2023) regarding gas-rich PRGs in WALLABY, as well as any work conducted collaboratively with other WALLABY members. Chapter 4 presents the moment panel plots used to determine the resolution-dependent detectability fraction of PRGs and explains the analyses undertaken to determine the incidence of gas-rich PRGs in WALLABY Public Data Release 1 (PDR1). Chapter 5 discusses the PRG candidates that were identified in WALLABY Public Data Release 2 (PDR2), and uses this information in order to estimate the incidence of gas-rich PRGs in PDR2. Chapter 5 also includes a discussion section that compares the results from the PDR1 and PDR2 incidence calculations, and details the limitations of this thesis as well as areas for future study.

2 Literature Review

Chapter 2 presents a review of relevant topics from previously published studies that will provide sufficient background information to enable the comprehension of future chapters. The Literature Review aims to summarize the supporting research that contributes to the study of polar ring galaxies (PRGs). Section 2.1 presents an overview of PRGs, including their history and the theories surrounding formation mechanisms. Subsection 2.1.1 discusses gas-rich PRGs specifically. Section 2.2 provides a brief introduction to the methods of modelling PRGs, focusing on the most relevant example: tilted ring modelling. Section 2.3 discusses previous incidence estimates that have been generated through numerous studies. Section 2.4 presents additional detail with respect to the WALLABY survey, and Section 2.5 outlines the goals of this thesis.

2.1 Polar Ring Galaxies

PRGs first began to be studied in the 1980s, when astronomers began to note the presence of these strange objects in sky surveys. Their methods of formation were also speculated upon, and the first formation theories that involved galaxy interactions were developed. The tidal stripping of gas from a passing galaxy was at the forefront of early PRG formation theories (Schweizer et al., 1983), involving no merger but rather a close pass of two galaxies. After a variety of PRG identifications Whitmore et al. (1990) catalogued images of PRGs and related objects, including kinematically confirmed PRGs, good morphological candidates, possible candidates, and possibly related objects. Whitmore et al. (1990) proposed that PRGs formed from mergers between two galaxies, and that this mechanism is fundamental to the comprehension of galactic behaviour. The authors also proposed that PRGs could offer insight into the behaviour of dark matter and dark matter halos.

Figure 2.1 shows a model PRG at various orientations projected onto a sky plane from Whitmore et al. (1990), which partially inspired the work

presented in this thesis. This was done for five different ring rotations (α) and five subsequent disk rotations (β), and only depicted the projected sky morphology. For the optical identification of PRGs, this figure was especially useful as it allowed astronomers to extrapolate how many PRGs may exist that cannot be identified due to their orientation. For example, at an orientation of $\alpha = 45°$, $\beta = 0°$ the polar component is completely obscured by the angle of the main galaxy's projection. It also demonstrated the different presentations of the polar configuration, which may not always be perfectly orthogonal.

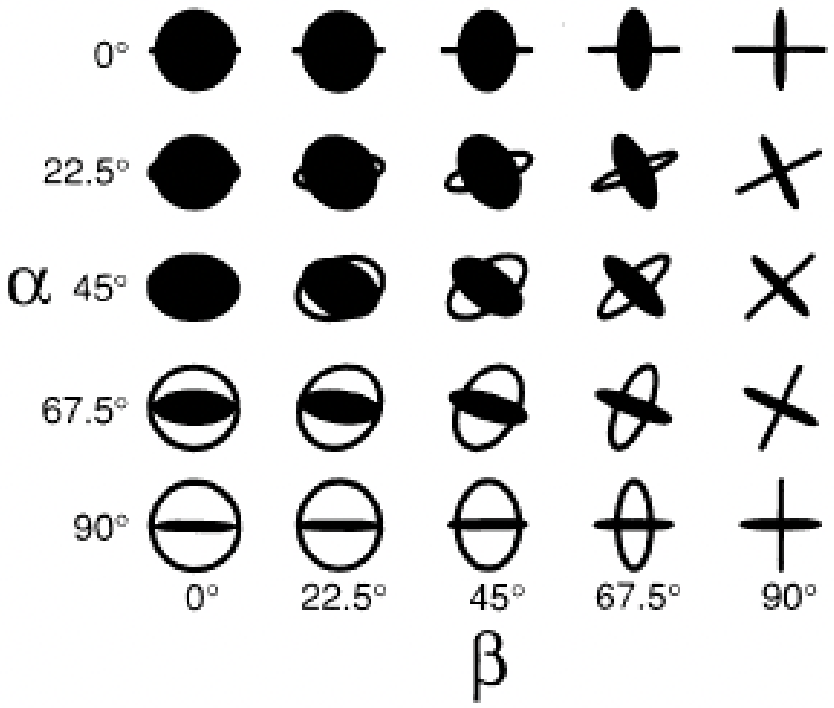

Figure 2.1: Sky-plane morphology of the same model PRG projected at different orientations (Whitmore et al., 1990). This diagram demonstrates the variety of appearances that PRGs can have, some of which make the polar structure exceedingly difficult to identify.

PRGs continued to be studied in terms of their structure and methods of formation, and began to be modelled through gas dynamical simulations (Reshetnikov and Sotnikova, 1997) in attempts to explain what galaxy features, if any, determine the shape and size of the polar component. Reshetnikov and Sotnikova (1997) determined that galaxies with massive dark matter

halos and main galaxy bodies, such as spiral galaxies, form rings that are wider and more extended than those formed around S0 type galaxies. S0 galaxies are lenticular galaxies, classified as an intermediate stage between spiral galaxies and elliptical galaxies. They have very little gas remaining and consist mostly of dust and older stellar populations.

Other formation theories emerged and gained support, such as the galaxy merger theory (Bekki, 1998). This theory posited that the polar component is formed through the orthogonal collision of two galaxies, wherein the smaller galaxy effectively forms the polar component. In the effort to classify PRGs, gas-gas misalignments were often ignored due to their difficulty to detect. Wakamatsu (1993) defined PRGs as S0 galaxies that possess perpendicularly rotating gaseous rings. Sparke and Cox (2000) described PRGs as objects with an early-type inner galaxy (i.e. lenticular or elliptical), that were likely the result of incomplete galaxy mergers rather than a potentially stable configuration.

Gas-star misalignments were the basis for many further studies, which led to new formation theories in the 2000s. Based on the assumption that PRGs are typically low-mass systems, as is the case with most gas-star and star-star misalignments, numerical simulations, cosmological simulations, and theoretical work supported the theory that cold gas accretion plays a major role in polar ring formation (Macciò et al., 2006; Brook et al., 2008). The argument against galactic interactions as a formation mechanism was that those theories did not self-consistently explain the large gas mass that is commonly found in polar structures, nor the ring's extended nature and the spatial coincidence of stars within the gas (Brook et al., 2008). There was also insufficient evidence of interaction-induced starbursts, which would be expected during a merger of two galaxies (Brook et al., 2008).

More recent studies turned their focus towards the dark matter halo present in PRGs, and found that the shape of the dark matter distribution in these objects varies strongly with radius (Khoperskov et al., 2014b,a). PRGs offer a unique opportunity to study the spatial distribution of gravitating matter in three dimensions, due to the two perpendicular planes of rotation (Khoperskov et al., 2014a; Combes, 2006), which could reinforce or refine dark matter predictions. While PRGs may be used to study dark matter, the opposite is also true. Moiseev et al. (2015) determined that the flattening of the dark matter halos varied with each PRG, which they suggested may be an indication that there is no singular method of formation across all PRGs. This theory is consistent with the Spavone et al. (2011) study, which found that one PRG formed through cold gas accretion but could not rule out tidal interactions for the second PRG. Khoperskov et al. (2013) contradicts flattened dark matter

halos in polar rings with a preference of oblate and triaxial dark matter halos, while other studies posit that the dark matter halos may be a combination of an oblate central portion with a prolate outer region (Khoperskov et al., 2014b; Combes, 2006). Due to the poor sample of PRGs with well-measured dark matter halo properties (Khoperskov et al., 2014b), this hypothesis cannot be confirmed. Identifying PRG candidates from WALLABY pilot fields could provide new gas-rich objects to study, and understanding the incidence of these systems in the local Universe will offer additional evidence as to how often these dark matter halos may be forming.

The Sloan Digital Sky Survey (SDSS) was used to find 31 new PRG candidates with the ring components found to have a larger scatter in their luminosity-size relation when compared to ordinary galaxies, which may be the result of a secondary origin (Reshetnikov and Mosenkov, 2019). This finding once again supports an acquisition event theory, rather than the slow accretion of gas from the surrounding intergalactic medium. These SDSS galaxies also exhibited a ring component within 20 degrees from a perfectly perpendicular orientation to the main disk in at least half of the candidates (Reshetnikov and Mosenkov, 2019). This supports the theory that perpendicular orientations are more stable, since they are observed most often and are therefore likely the longest lasting when compared to other misaligned geometries.

2.1.1 Gas-Rich PRGs

Gas-rich PRGs are objects where the ring or disk contains a reservoir of HI. In order to detect both components accurately through a radio telescope, the main galaxy body must be gas-rich as well. These tend to be spiral galaxies, rather than the quenched, gas-poor elliptical or lenticular galaxies that are commonly observed with rings in the optical (Stanonik et al., 2009). Many formation theories for gas-rich PRGs are based upon the assumption that the main galaxy body is an early-type galaxy - either elliptical or S0. Observing younger galaxies that have not yet exhausted their gas content and discovering that some possess a kinematically misaligned tilted ring of HI gas provides a new perspective on polar ring formation theories. Some astronomers argue that the lack of stellar counterpart to the gas-rich rings indicate the cold gas accretion method is in its early stages, where the gas has not yet cooled enough to form stars (Stanonik et al., 2009). Others have simulated the formation of these gas-rich objects through tidal interactions (Bournaud and Combes, 2003), which was then opposed with the argument that any galaxy interactions would transform the main galaxy body into an elliptical remnant without the rotation observed in disk and lenticular galaxies

(Bournaud et al., 2005; Stanonik et al., 2009). The formation theory debate continues despite numerous simulations, and gas-rich PRGs have instigated a new avenue of research for the topic.

2.2 Modelling PRGs

To zeroth order, the disks of spiral galaxies are flat. While their dynamics over time can be self-consistently simulated (Bournaud and Combes, 2003; Bournaud et al., 2005), including galactic interactions and star formation, it is also possible to approximate their kinematics as flat rotating disks. PRGs present unique modelling challenges due to their polar component, which rotates in a plane perpendicular to that of the main body. This component introduces a structural complexity which requires the galaxy to be separated into a series of tilted rings. Figure 2.2 demonstrates a tilted ring model, where each ring comprises a radial section of the galaxy. These rings are nested, meaning they do not overlap, and are concentric, meaning they share the same centre. Each individual ring can be modelled at its own orientation, which allows the morphology of a polar ring to be replicated.

The kinematics of a polar component must be separate from that of the main galaxy component. Both can be modelled in the sky plane using the velocity of tilted rings that follow:

$$V_{LOS}(r, \theta) = V_{sys} + V_{rot}(r) \sin[i(r)] \cos(\theta), \tag{2.1}$$

where V_{LOS} is the disk or ring model's line of sight velocity, V_{sys} is the object's systemic velocity, $V_{rot}(r)$ is the rotational velocity, $i(r)$ is the inclination as a function of radius, and θ is the cylindrical coordinate of a parcel of gas relative to the major axis in the plane of the disk. So, this nested ring model is a useful technique to replicate tilted rings in galaxies due to its ability to account for unique sets of geometric and kinematic parameters for each component.

There are a few algorithms that use the titled ring modelling method to generate three dimensional models, including TiRiFiC (Józsa et al., 2007), FAT (Kamphuis et al., 2015), and 3DBAROLO (Teodoro and Fraternali, 2015). These codes primarily focus on modelling existing data, rather than generating tilted-ring models. For that, the MockCubeGenerator Suite (MCG-Suite) set of programs was developed (Deg and Spekkens, 2022). MCGSuite, or MCG, functions through tilted ring modelling as well. Each ring is populated by a set of tracer particles that are projected onto the 'sky' and 'observed' according to the parameters input by the user. Figure 2.3 shows the process

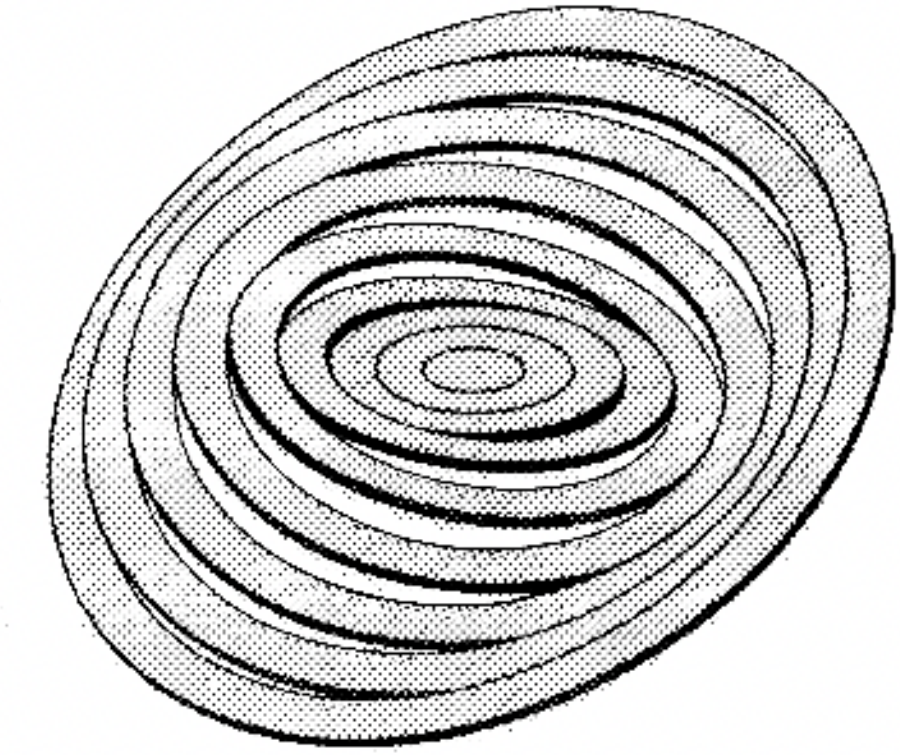

Figure 2.2: Tilted ring modelling consists of a series of nested rings that can be inclined at individual angles to create realistic galaxy disks. This figure demonstrates the nested ring concept (Rogstad et al., 1974).

of creating a data cube using a tilted ring model. MCG accepts a variety of inputs from the user, including the number of rings, the ring dimensions, the inclination and position angle of each ring, the desired noise value, the beam size, the systemic velocity, and the velocity of each ring. The radial position of tracer particles is selected such that the particle density is constant across each ring (Deg and Spekkens, 2022). This process can generate a realistic model that can be used to study the kinematic and morphological profile of these unique objects.

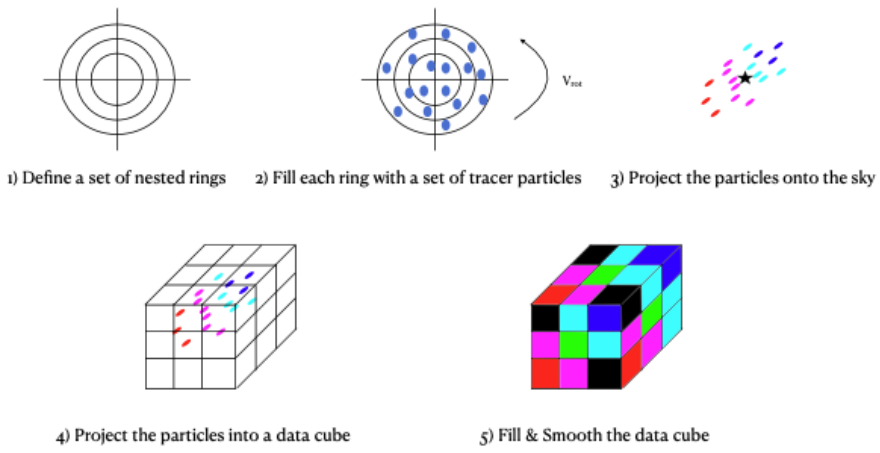

Figure 2.3: An illustration from Deg and Spekkens (2022) that demonstrates the process of generating a data cube using a tilted ring model. The coloured particles and cells in steps 3-5 represent the line of sight velocity of each component, with red receding and blue approaching.

2.3 Estimating the Incidence of PRGs

The first PRG incidence estimate was conducted by Whitmore et al. (1990), who determined that roughly 0.5% of all nearby S0 galaxies appeared to have polar rings. This paper also attempted to extrapolate based on detectability due to the galaxy's orientation, and amended that selection effects could increase the percentage to approximately 5% of nearby S0 galaxies. The larger estimate was generated when Whitmore et al. (1990) corrected their detected incidence to account for nonoptimal viewing orientation, after noting that less than half of the viewing orientations in Figure 2.1 were conducive to the effective identification of the system as a PRG. For every obvious polar ring, they estimated that there existed two other polar rings that could not be accurately observed. Whitmore et al. (1990) also corrected for the possible dimming, as well as the limited lifetime, of the ring by assuming that the ring is only visibly present for one third of the galaxy's lifetime. This accounted for any galaxies that had a polar ring in the past that no longer exists. The study's estimate applied only to S0 galaxies, which generally exhibit star-star and gas-star misalignments due to their relatively gas-poor nature. These misalignments are estimated to be far more common than the gas-gas misalignments being

examined in this thesis (Stanonik et al., 2009).

Moiseev (2014) determined that 18% of nearby luminous blue compact dwarf galaxies, in a sample of 28 objects, possessed inner and external polar structures. These galaxies were gas-rich late-type galaxies, meaning the polar rings being observed were gas-gas misalignments. Serra et al. (2012) estimated a PRG incidence of only 1.8% in their considerable sample of 166 exclusively early-type galaxies. Despite the early-type main galaxies being relatively gas-poor, the polar rings were detected in HI. Therefore, the Serra et al. (2012) study was primarily focused on gas-star misalignments. Both of these studies were examining specific types of galaxies, either luminous blue compact dwarf galaxies or early-type galaxies, which precludes an accurate incidence estimate for gas-rich PRGs across the local Universe. The canonical literature value to which the findings of this thesis will be compared is the $\sim$0.1% determined in 2011 (Reshetnikov et al., 2011). This value is the most recent estimate for the incidence of gas-rich PRGs, although not an exact comparison for the analysis being conducted in this thesis. Reshetnikov et al. (2011) use a luminosity function to estimate the incidence of gas-rich PRGs, and do not conduct a detectability analysis specific to HI observations to extrapolate the genuine incidence from the identifiable incidence.

A luminosity function is essentially the distribution of galaxies across luminosity intervals (Blanton et al., 2001), and is one of the basic descriptions of galaxy population (Smirnov and Reshetnikov, 2022). Smirnov and Reshetnikov (2022) recently published a luminosity function of PRGs and found that polar structures occur approximately twice as frequently around bright and red galaxies rather than blue ones. They also determined that the volume density of PRGs increases with redshift. While this study provides detail regarding the nature of PRGs and the conditions under which they are more commonly observed, it does not take the observational obstacles associated with identifying PRGs into account. This thesis is the first instance of a gas-rich PRG incidence estimate, using data from an untargeted radio astronomy survey, that accounts for the orientation and resolution of PRG detections.

2.4 WALLABY

WALLABY (Koribalski et al., 2020) is an untargeted survey that will observe the HI gas distribution within over 200,000 galaxies in the Southern Hemisphere out to redshift z $\sim$0.1. The first phase of the WALLABY pilot survey observed three fields, and the second phase focused on five fields. Each field is centred on an object or cluster and covers 30 square degrees of the Southern

sky. These 30 square degrees are constructed from two adjacent tiles which themselves consist of two interwoven ASKAP footprints that are 36 beams across (Koribalski et al., 2020). This methodology provides a relatively consistent noise level across each field, ∼1.67 mJy/beam, with a beam that is 30 arcsec across (Koribalski et al., 2020). The actual noise levels in each field vary slightly. Once the cubes are constructed, the SoFiA source finder (Serra et al., 2015; Westmeier et al., 2021) is used to catalogue individual HI detections in all fields.

A radio telescope defines resolution through the Rayleigh criterion:

$$\theta = 1.2\frac{\lambda}{D} \ , \tag{2.2}$$

where θ is the angular resolution, λ is the wavelength being observed, and D is the diameter of the aperture (Rayleigh, 1879). This criterion specifies the minimum separation between two celestial sources that can be resolved as individual objects, or the best obtainable resolution. This resolution is equivalent to the beam size, and is 30 arcsec for the WALLABY survey.

WALLABY Public Data Release 1 (PDR1) (Westmeier et al., 2022) was focused on three fields: the Hydra and Norma clusters as well as the NGC 4636 group. The PDR1 catalogue included 301 detections in Hydra, 144 detections in Norma, and 147 detections in NGC 4636. The majority of these are marginally resolved, with only 190 objects having a resolution greater than ∼4 beams across (BA). WALLABY Public Data Release 2 (PDR2) focused on five fields that were centred on the NGC 4808 group, the NGC 5044 group, and the Vela cluster. The data distribution to the WALLABY team from the NGC 5044 group was broken into three phases (DRs, or Data Releases) due to its size, and there were some detections that were released in two different phases. The internal PDR2 catalogue included 231 detections in NGC 4808, 353 detections in NGC 5044 DR1, 630 detections in NGC 5044 DR2, 1326 detections in NGC 5044 DR3, and 203 detections in Vela, with a public release of the PDR2 data planned for later this year.

Figure 2.4 shows a plot of WALLABY detections from PDR1 (Deg et al., 2022) created by a WALLABY collaborator. The circles represent the sources from the Hydra cluster, the stars represent the sources from the Norma cluster, and the triangles represent the sources detected in the NGC 4636 field. The colours on this plot depict which objects had kinematic modelling attempted on them, which included most of the detections with an ell_maj value above two beams. ell_maj represents the resolution of the detection and is approximately equal to the resolution in BA divided by two. Kinematic modelling was not attempted for objects with $\log(S/N_{obs}) < 1.25$. S/N_{obs} is the integrated

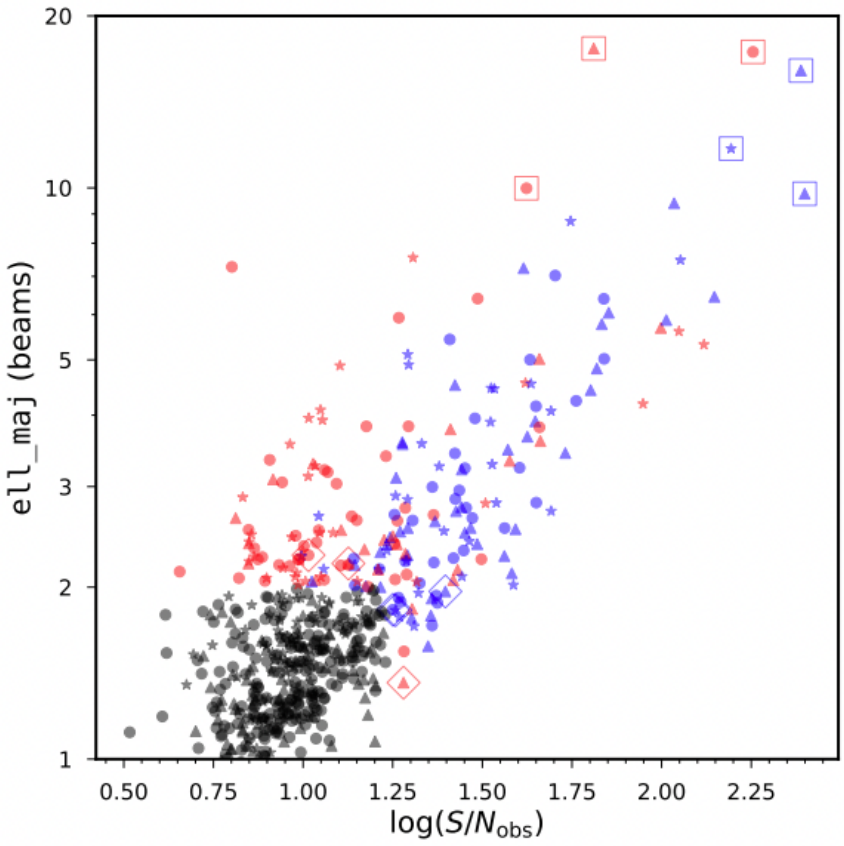

Figure 2.4: Size (as estimated by ell_maj) as a function of integrated S/N of WALLABY PDR1 detections (Deg et al., 2022). This plot includes the sources from the Hydra (circles), Norma (stars), and NGC 4636 (triangles) fields. Coloured points represent all detections with ell_maj > 2 beams or $\log(S/N_{obs}) > 1.25$, for which kinematic models were attempted. Models that were successful are shown in blue, and unsuccessful models are shown in red.

observed signal-to-noise ratio of the detection. Objects that were able to be successfully modelled were shown in blue, while objects that were unable to be modelled were shown in red. The larger open symbols in the figure represent objects for which kinematic plots were included in the source paper. The purpose of Figure 2.4 is to demonstrate that most WALLABY detections occur in the marginal-low resolution and low S/N regime, which makes determining unique features challenging.

Despite the majority of WALLABY detections being marginally resolved, two PRG candidates were detected in PDR1 (Deg et al., 2023). NGC 4632 and NGC 6156 were identified from their morphologies and kinematics during the standard analysis of PDR1 detections. Their identification prompted this study, since the nature of WALLABY offered a unique opportunity to investigate the detectability of PRGs among marginally resolved objects. The survey also collected data from a wide variety of objects such that it better represents the genuine incidence of extragalactic systems. This thesis is the first PRG incidence estimate from an untargeted HI survey, which could provide a more accurate insight into their prevalence in the local Universe.

2.5 Thesis Goals

The aim of this thesis is to investigate the incidence of gas-rich polar rings using the pilot phase of the WALLABY survey. Two PRG candidates were identified in PDR1, which were then used to generate two 3D PRG models (Deg et al., 2023). These model galaxies were used to simulate different observation conditions through modifications of the ring orientation angle (see Section 4.1) as well as the galaxy's inclination. Their dimensions were also altered in order to account for the effect of resolution on detectability, and these parameters were input into MCG to create mock observations. The mock observations were assessed for whether they could be reasonably identified through their kinematics and morphology. Using the weighted detectability of the model objects in conjunction with data from PDR1, the universal incidence of polar gaseous kinematic misalignments was able to be estimated with a greater degree of accuracy. PDR2 detections were examined and PRG candidates were identified. The incidence calculation was then applied to PDR2 data in order to reinforce the findings from PDR1.

Understanding the frequency of PRG occurrence across the local Universe will be useful in future studies of formation theories and galaxy interactions. Identifying potential gas-rich PRGs from their morphology and kinematic profiles in HI studies will allow radio astronomers to target these objects for further research. Gas-rich PRGs can be studied from the perspective of various fields, offering insight into subjects such as dark matter halos and potentially continual cold gas accretion from the galaxy's surroundings. This thesis finds that gas-rich PRGs are more common than historical literature values, and are as accessible to radio astronomers as PRGs have been to astronomers who study objects at visible wavelengths.

3 Polar Rings in WALLABY PDR1

This chapter describes the polar ring galaxy (PRG) candidates discovered in WALLABY PDR1, and how those galaxies were modelled. Section 3.1 discusses the format of WALLABY data, and introduces moment maps. Section 3.2 presents PRG candidates NGC 4632 and NGC 6156 as well as a brief overview of the creation of their best fitting kinematic models.

3.1 Survey Data

3.1.1 Data Cubes

WALLABY observations deliver 3D detections of HI in galaxies, which can be represented as three-dimensional data cubes that contain thousands of pixels representing the HI within the galaxy. The x- and y-axes are the dimensional coordinates of right ascension (RA) and declination, as would be expected in a cartesian plane. The z-axis is the Doppler frequency axis, which can be converted to a recessional velocity using the rest wavelength of the HI line.

Figure 3.1 demonstrates the data cube structure using three frames from a data cube, which can be viewed in slices. Data cubes can be difficult to visualize since the z-axis is Doppler frequency rather than another dimensional coordinate. The brightness indicates the density of HI atoms in each pixel, and the grainy foreground is Gaussian random noise. The galaxy in Figure 3.1 is one of the models created for NGC 4632, a PRG candidate discovered in PDR1 that will be discussed further in Section 3.2. This mock galaxy has an angular resolution of 10 BA, so the images are much clearer than those presented in Figure 3.2. At lower resolutions, the noisy foreground obscures the HI detections when the cube is being visually examined.

Figure 3.2 shows frames from a data cube at a considerably lower angular resolution. Not only is the viewing area often smaller when the file is opened,

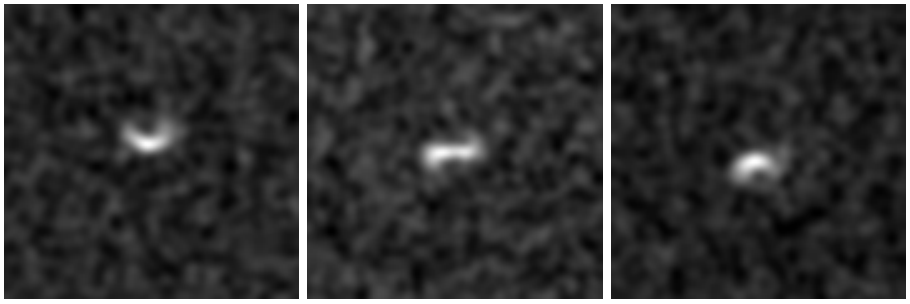

Figure 3.1: Velocity slices from the data cube for an NGC 4632 model galaxy at a resolution of 10 BA, an inclination of 30° and a ring orientation angle of 30°. Each frame is ∼35.6 km/s apart to best demonstrate the different presentations of a galaxy in a data cube.

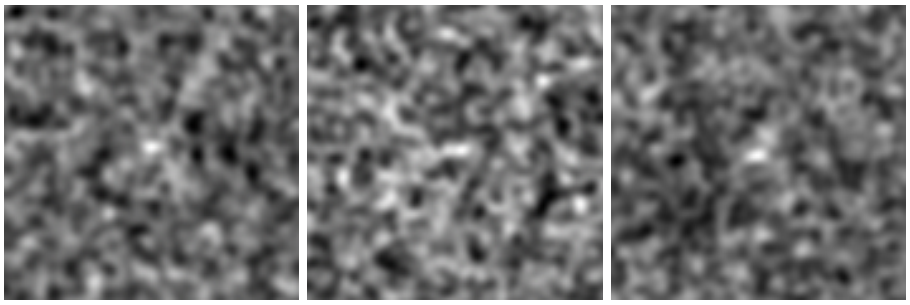

Figure 3.2: Slices from the data cube for an NGC 4632 model galaxy at a resolution of 3 BA, an inclination of 30° and a ring orientation angle of 30°. Each frame is ∼35.6 km/s apart and corresponds to the subfigure with the same letter in Figure 3.1.

but there is considerably more noise obscuring the galaxy's features. These sections are from the data cube for an NGC 4632 galaxy model resolved at 3 BA. The SoFiA masks applied to this type of data cube are less precise, since most of the galaxy observations are nearly as faint as the noise. Noise can be erroneously included in the galaxy's borders, creating a morphology that is not entirely accurate. The static visible in Figure 3.2 is a good depiction of what the masking program is trying to filter. Some of the slices show the galaxy as a bright spot, but most of the slices also contain unrelated bright spots that could easily be mistaken as part of the object. These regions of

noisy data, when included in low resolution moment plots, can be extremely misleading with respect to polar ring signatures in morphology and kinematics. Nevertheless, low resolution cubes can still offer a considerable amount of valuable information.

3.1.2 Moment Maps

In order to analyze the data cubes created by WALLABY, a code was written to generate two plots for each detection. Galaxy files with resolutions less than 3 BA were discarded. This was due to the detectability fraction at this resolution, as is seen in Figure 4.17 and will be discussed further in Section 4.4. A model PRG's detectability fraction at 3 BA was determined to be zero, therefore any detected PRGs with resolutions less than 3 BA would be essentially impossible to identify at this stage. Due to the improbability of a reliable identification, poorly resolved objects were filtered out of further analysis. The remaining galaxies were then analyzed by the Python program SoFiA (Serra et al., 2015), which generated masks for each detection that identified where the galaxy emission was located in the data cube.

The mask was then applied to the data cubes and the files were processed into two diagrams: moment zero and moment one. Moment zero maps depict the morphology of the detected galaxy. They plot the position and density of HI particles such that the shape of the galaxy can be studied. Moment one is the first derivative of moment zero, and it depicts the kinematics of the detected galaxy. It plots the velocity of each particle such that the motion of the gas can be studied. The maps for each detection were examined closely for polar ring signatures. Looking for polar component morphology in the moment zero panel was difficult at low angular resolutions. Galaxies exist in a variety of shapes with distortions, misalignments, warps, and other forms of anomalous gas that could be mistaken for a polar disk. At higher resolutions, these unique structures are typically able to be observed and recognized more reliably. At lower resolutions, the identification of PRG candidates relied heavily on the moment one map.

Figure 3.3 shows the morphology and kinematics of a reasonably symmetrical, regular galaxy. This is WALLABY J101232-451408, detected in the Vela cluster at approximately 7 BA. The morphology is perhaps unusually smooth and consistent, even for a regular galaxy. Many galaxies have bits of gas that are slightly detached, or elongated features. At lower resolutions, the moment zero maps can have a lot of anomalies due to noise. The moment one panel demonstrates a typical velocity gradient for a galaxy without kinematically misaligned components. The colours transition smoothly from red, to yellow,

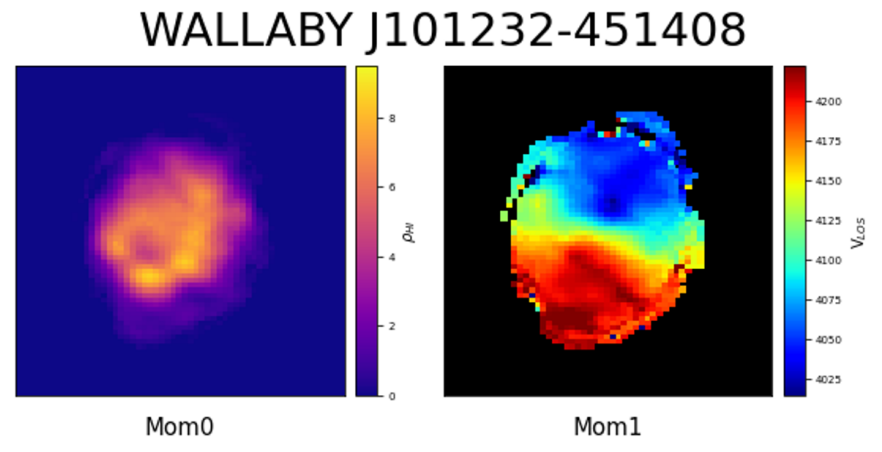

Figure 3.3: The moment zero (left) and moment one (right) maps for a galaxy without ostensible kinematic misalignments detected at a resolution of ∼7 BA. The morphology is exceptionally round, and the kinematic velocity gradient is consistent across the galaxy body.

to green, to cyan, and then finally to blue. This is what would be expected from regular moment one maps, with some leeway for morphological anomalies and noise.

When examining the kinematics of PRGs there are a variety of signature features that suggest the presence of a kinematically misaligned gaseous component, but these cannot confirm the presence of a polar ring independently. Further research may consist of similar studies for other types of kinematic anomalies in order to better discern the specifics of which indicators are unique only to polar components. Depending on the resolution and the qualities of the polar component, the moment maps can vary considerably. Section 4.2 will demonstrate the effect of angular resolution on the moment maps of model PRGs.

3.2 PRGs in PDR1

WALLABY PDR1 was released last year, and an analysis was run on its galaxies by a WALLABY collaborator. Among the 592 galaxies that were observed in WALLABY PDR1, two candidates were identified as potential PRGs from their moment maps. Their candidacy was supported by the 3D rendering of their data cubes, which clearly demonstrated polar components.

NGC 4632 was detected at a resolution of ∼10 BA, allowing the ring features to be seen clearly in its morphology. Figure 3.4 includes the moment zero and moment one maps for this PRG candidate from PDR1. It is clear that there is a misaligned gas-rich ring surrounding the main galaxy body in the moment zero panel. The moment one panel, however, does not possess any evident signatures associated with polar components. This is due to the orientation of the ring, as will be discussed further in this thesis.

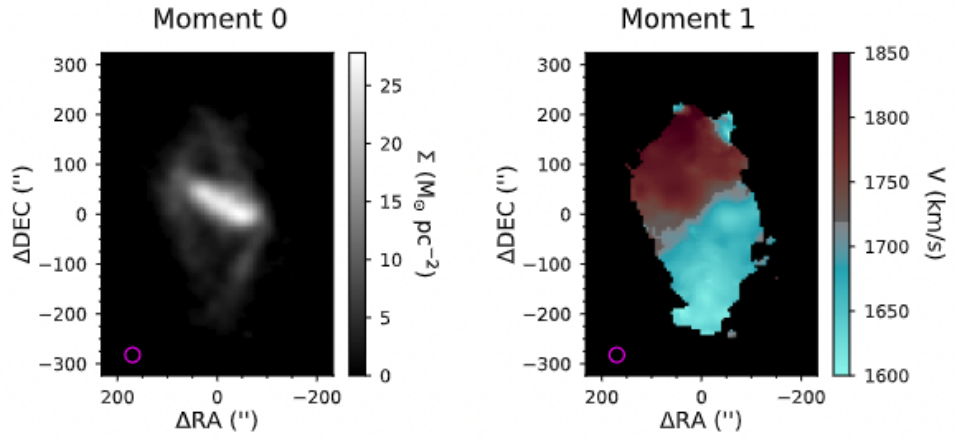

Figure 3.4: NGC 4632 moment zero (left) and moment one (right) maps. The morphology from the moment zero map clearly depicts a polar ring surrounding the main galaxy body, while the kinematics do not offer much insight (Deg et al., 2023).

NGC 6156 was not as well resolved as NGC 4632 with an observation resolution of ∼6 BA. Figure 3.5 includes the moment zero and moment one maps for this galaxy. In moment zero, the morphology of the galaxy does not provide any insight with respect to the presence of a polar component. The moment one map, in this case, was what suggested the potential presence of a kinematically misaligned gas ring. The velocity field is far from the smooth gradient consistent with a gas disk, and suggests that the observed object contains multiple components.

Table 3.1 provides a brief comparison between the two PDR1 detections. The number of rings in each model will be discussed further in Section 3.2.1.

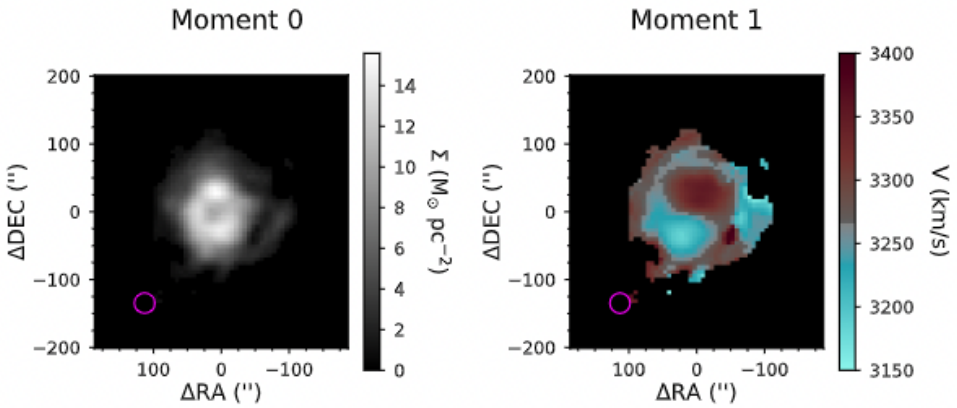

Figure 3.5: NGC 6156 moment zero (left) and moment one (right) maps. The morphology does not demonstrate the existence of a polar component, however the kinematics provided sufficient evidence to flag this galaxy for further investigation (Deg et al., 2023).

Parameter	NGC 4632	NGC 6156
Detection Resolution	10 BA	6 BA
Number of Rings in Model	9	5
Systemic Velocity (km/s)	1725	3270
HI Mass ($\log(M_{HI}/M_{\odot})$)	9.37	9.92

Table 3.1: PRG properties of NGC 4632 and NGC 6156 from WALLABY PDR1 data. The detection resolution and systemic velocity are rounded to the nearest whole number, and the mass of atomic hydrogen in each galaxy was calculated by Deg et al. (2023).

3.2.1 MCGSuite & Tilted Ring Models

The NGC 4632 and NGC 6156 models used throughout this thesis were generated using an approximation of the two observed PRGs in PDR1 and a program from MCGSuite (Deg and Spekkens, 2022). MCG accepts inputs for a galaxy's size, inclination, and position angle through a series of nested rings. It then populates a cube with particles and applies noise to mimic observation conditions experienced by radio astronomers (see Section 2.2). These mock cubes can then be processed to generate moment maps comparable to those found during the data analysis of WALLABY galaxies.

The two observed galaxies first had to be fitted with models that ap-

proximated their dimensions and features as best as possible. This was done through a modelling program called 3DBAROLO (Teodoro and Fraternali, 2015) by a WALLABY collaborator (Deg et al., 2023). Figure 3.6 shows a comparison between the best fitting model and the genuine observation for both the moment zero and moment one panels for NGC 4632, and Figure 3.8 depicts the same comparison for NGC 6156 and its best fitting model. These are flat-disk tilted ring models, with the outermost ring designed to be perfectly polar. It is clear that the models are quite close to the observed object but are rather idealized in their shapes. NGC 6156's ring became relatively noticeable in the model's moment zero map, but overall these models were determined to approximate the observed galaxies well enough to be used for future analyses. The rings were simplified to be perfectly circular as well as precisely polar, and each model was assigned a number of rings to accurately reflect the morphology.

Figure 3.7 shows the rotation curve, inclination, surface density, and position angle for NGC 4632's best fitting model. Figure 3.9 shows the same plots for NGC 6156's best fitting model. Each point in each plot respresents one of the model's rings; five in NGC 6156's model and nine in NGC 4632's model. The point that is separate and also shaped like a star represents the polar ring, detached from the main galaxy body rings and noticeably off-trend in inclination and position angle. The polar ring is rotating perpendicular to the main galaxy body, so this was to be expected.

With models for NGC 4632 and NGC 6156 already created, it was then possible to project those models onto the sky plane at different orientations in order to explore how the detected moment zero and moment one maps would change. These different projections would then allow for the estimation of the incidence of these objects from the WALLABY PDR1 detection statistics. A few additional calculations were necessary before a code could be developed that would generate these galaxy models at various observation conditions. These calculations will be discussed in Section 4.1.

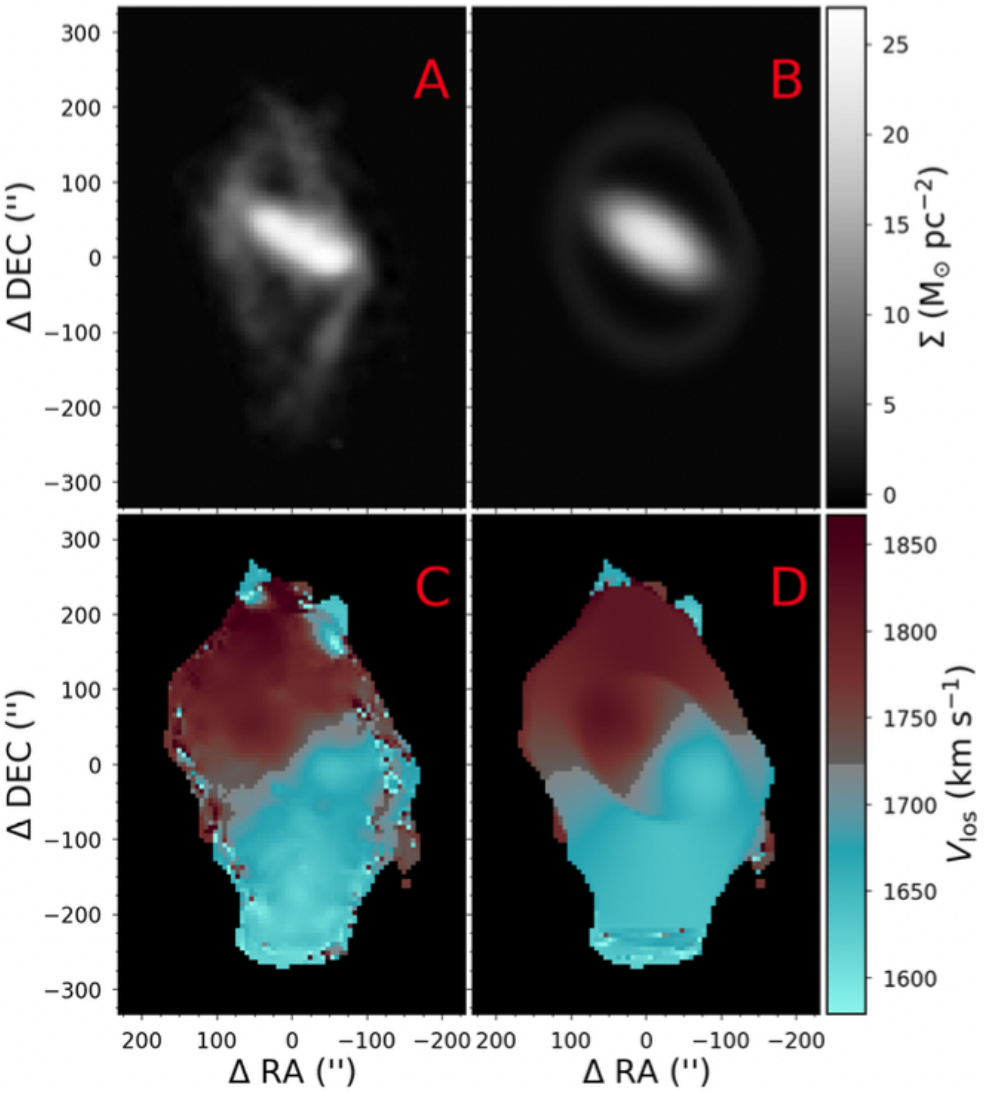

Figure 3.6: The best fitting HI PRG model of NGC 4632 (Deg et al., 2023). Panel A shows the observed moment zero map and panel C shows the observed moment one map, while panel B shows the model moment zero map and panel D shows the model moment one map. The moment zero maps use a linear stretch which explains the difference in size of the moment zero and moment one components.

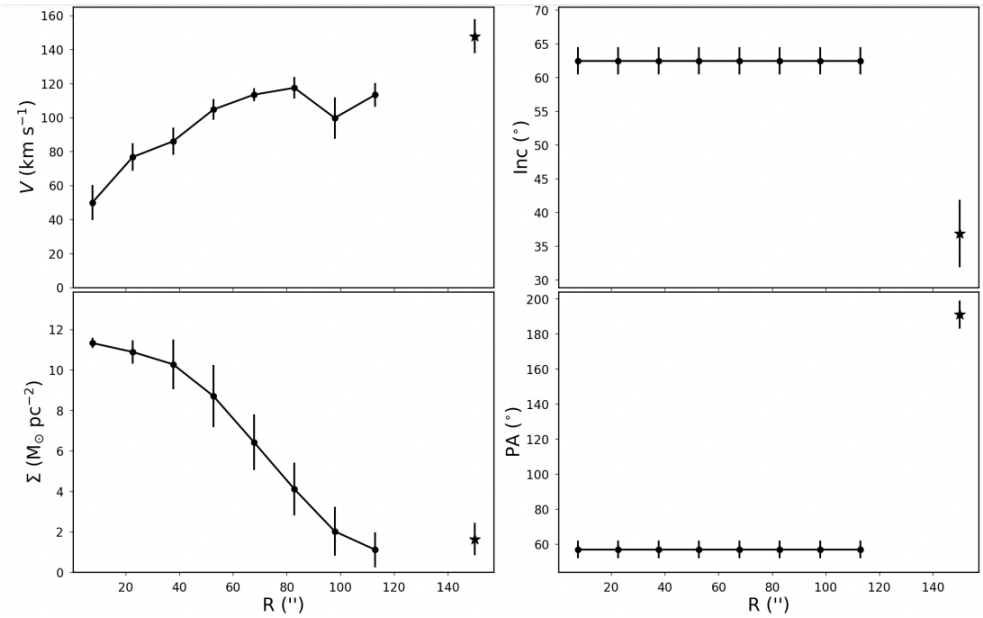

Figure 3.7: Best fitting model parameters for NGC 4632 (Deg et al., 2023). The left panels show the rotation curve (top) and surface density (bottom), while the panels on the right show the inclination (top) and position angle (bottom). The polar ring parameters are indicated by stars and are the last radial point in each panel.

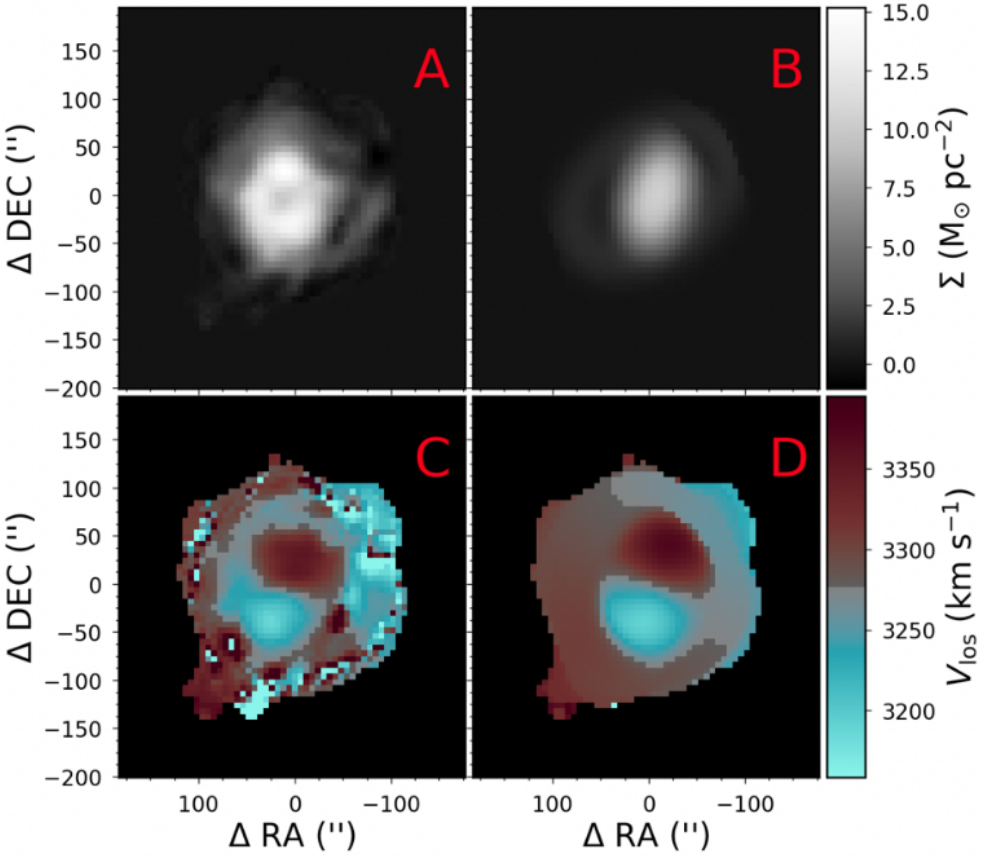

Figure 3.8: The best fitting HI PRG model of NGC 6156 (Deg et al., 2023). The panels have the same layout as in Figure 3.6.

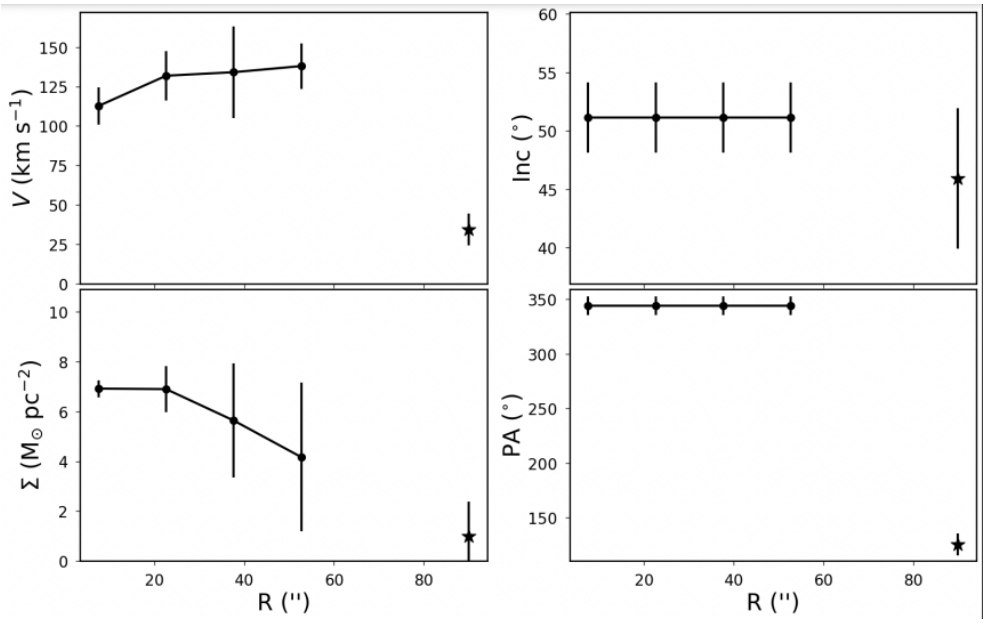

Figure 3.9: Best fitting model parameters for NGC 6156 (Deg et al., 2023). The panels have the same layout as in Figure 3.7.

3.3 Summary

Chapter 3 presented a brief overview of data cubes, as well as an introduction to the moment maps that will be analyzed in future chapters. Moment zero maps depict the galaxy's HI morphology, and moment one maps depict the HI kinematics within a galaxy. The two PRG candidates that were discovered in PDR1, NGC 4632 and NGC 6156, were discussed and their best fitting models were presented. This information provides sufficient background for Chapter 4, which will use the best fitting models to generate PRGs at a variety of sky projections and angular resolutions in order to explore their detectability and estimate their incidence.

4 Polar Ring Galaxy Incidence in PDR1

Chapter 3 introduced the two PRG candidates identified from WALLABY PDR1 data, NGC 4632 and NGC 6156, as well as their best fitting models. This chapter aims to determine the incidence of gas-rich PRGs using the data from PDR1 in conjunction with numerous mock galaxy detections. Section 4.1 presents a formalism that was derived in order to alter the observation conditions of the model PRGs, and introduces the moment panel plots that were generated in order to determine the detectability fraction of PRGs at different orientations and resolutions. Section 4.2 discusses the effects of angular resolution on detectability, and Section 4.3 identifies some of the PRG signatures evident in the moment panel plots. Section 4.4 presents the detectability fraction of PRGs at different angular resolutions, and Section 4.4.1 uses these fractions along with PDR1 data statistics in order to estimate the incidence of gas-rich PRGs in the local Universe.

4.1 Moment Panel Plots

In order to determine the detectability of PRGs at different observation conditions, mock galaxy detections were generated through MCG. These cubes resembled real detections from the WALLABY survey, such that they could be reliably used alongside PDR1 data statistics. MCG accepts a series of parameters and specifications regarding the mock observation (see Section 2.2), which were able to be altered in order to examine the NGC 4632 and NGC 6156 best fitting models at different orientations and angular resolutions.

It was difficult to calculate what ring inclination angle (with respect to the main galaxy body) would be generated using the MCG input files, which only accepted values for inclination (i) and position angle (PA) on the observational plane. In order to translate the ring's 90 degree offset from the main galaxy

body into MCG's coordinates, the matrix included in Equation 4.12 had to be developed and applied to relate the sky-plane coordinates to the galaxy-plane coordinates and determine the ring's projection on the galaxy plane.

These equations were first derived by a WALLABY collaborator through a rotation matrix applied to three planes: the sky plane, the galaxy plane, and the ring plane. The general relation between the sky plane and the galaxy plane is:

$$\mathbf{x}_s = R_z(\theta_g)R_x(i_g)\mathbf{x}_g \ , \tag{4.1}$$

where $\mathbf{x}_s$ are the sky plane coordinates ($\mathbf{x}_s = (x_s, y_s, z_s)$), $\mathbf{x}_g$ are the galaxy plane coordinates ($\mathbf{x}_g = (x_g, y_g, z_g)$), $R_z(\theta_g)$ is the rotation about the z_g axis by the main disk position angle θ_g ($\theta_g = PA_g + 90°$), and $R_x(i_g)$ is the rotation about the x_g axis by the main disk inclination i_g. A similar relation translates the coordinates in the ring plane into points on the sky plane:

$$\mathbf{x}_s = R_z(\theta_r)R_x(i_r)\mathbf{x}_r \ , \tag{4.2}$$

where the rotations are the same as in Equation 4.1 except the galaxy coordinates are replaced with the ring plane coordinates ($\mathbf{x}_r = (x_r, y_r, z_r)$). Expanding this into matrices gives:

$$\mathbf{x}_s = \begin{pmatrix} c_{\theta r} & -s_{\theta r} & 0 \\ s_{\theta r} & c_{\theta r} & 0 \\ 0 & 0 & 1 \end{pmatrix} \begin{pmatrix} 1 & 0 & 0 \\ 0 & c_{ir} & -s_{ir} \\ 0 & s_{ir} & c_{ir} \end{pmatrix} \mathbf{x}_r \ , \tag{4.3}$$

where c is the cosine function and s is the sine function, and the subscript indicates the variable. For example, $c_{ir} = cos(i_r)$. This matrix multiplication can be simplified into:

$$\mathbf{x}_s = \begin{pmatrix} c_{\theta r} & -s_{\theta r}c_{ir} & s_{\theta r}s_{ir} \\ s_{\theta r} & c_{\theta r}c_{ir} & -c_{\theta r}s_{ir} \\ 0 & s_{ir} & c_{ir} \end{pmatrix} \mathbf{x}_r \ . \tag{4.4}$$

This same rotation matrix can be used to translate the galaxy plane points into the sky plane if the galaxy's angles are used instead of the ring's (i.e. substitute the r's for g's).

In order to project the ring perpendicularly to the galaxy body, there must be a relation between the galaxy plane and the ring plane:

$$\mathbf{x}_g = R_z(\beta)R_y(\phi)R_x(\alpha)\mathbf{x}_r \ . \tag{4.5}$$

Where a few new variables are introduced. $R_x(\alpha)$ is the rotation about the x_r axis by α, which is the orientation of the ring relative to the galaxy plane. For the modelling of PRGs in this thesis, the ring was assumed to be perfectly polar such that $\alpha = 90°$. $R_y(\phi)$ is the rotation about the y_r axis by ϕ, which is the vertical angle between the ring's major axis and the galaxy plane. This is mostly useful for elliptical rings and is not typically applicable for the circular rings that are being modelled, but it is necessary for further rotation into the sky plane coordinates. $R_z(\beta)$ is the rotation about the z_r axis by β, which is the angle between the ring plane and the side of the galaxy approaching the observer ($+x_g$ axis). Figure 4.1 illustrates the angle β as viewed in the galaxy plane.

Next, expanding the matrices in Equation 4.5 gives:

$$\mathbf{x}_g = \begin{pmatrix} c_\beta & -s_\beta & 0 \\ s_\beta & c_\beta & 0 \\ 0 & 0 & 1 \end{pmatrix} \begin{pmatrix} c_\phi & 0 & s_\phi \\ 0 & 1 & 0 \\ -s_\phi & 0 & c_\phi \end{pmatrix} \begin{pmatrix} 1 & 0 & 0 \\ 0 & c_{90} & -s_{90} \\ 0 & s_{90} & c_{90} \end{pmatrix} \mathbf{x}_r \ , \tag{4.6}$$

$$\mathbf{x}_g = \begin{pmatrix} c_\beta & -s_\beta & 0 \\ s_\beta & c_\beta & 0 \\ 0 & 0 & 1 \end{pmatrix} \begin{pmatrix} c_\phi & 0 & s_\phi \\ 0 & 1 & 0 \\ -s_\phi & 0 & c_\phi \end{pmatrix} \begin{pmatrix} 1 & 0 & 0 \\ 0 & 0 & -1 \\ 0 & 1 & 0 \end{pmatrix} \mathbf{x}_r \ . \tag{4.7}$$

Which can now be simplified as:

$$\mathbf{x}_g = \begin{pmatrix} c_\beta & -s_\beta & 0 \\ s_\beta & c_\beta & 0 \\ 0 & 0 & 1 \end{pmatrix} \begin{pmatrix} c_\phi & s_\phi & 0 \\ 0 & 0 & -1 \\ -s_\phi & c_\phi & 0 \end{pmatrix} \mathbf{x}_r \ , \tag{4.8}$$

$$\mathbf{x}_g = \begin{pmatrix} c_\beta c_\phi & c_\beta s_\phi & s_\beta \\ s_\beta c_\phi & s_\beta s_\phi & -c_\beta \\ -s_\phi & c_\phi & 0 \end{pmatrix} \mathbf{x}_r \ . \tag{4.9}$$

The position angle of the galaxy does not affect the detectability of the polar component, so for simplicity θ_g can be set to zero. This means that Equation 4.1 simplifies to:

$$\mathbf{x}_s = \begin{pmatrix} 1 & 0 & 0 \\ 0 & c_{ig} & -s_{ig} \\ 0 & s_{ig} & c_{ig} \end{pmatrix} \mathbf{x}_g \ . \tag{4.10}$$

The ring can be rotated into galaxy plane coordinates before being projected into the sky plane coordinates by substituting Equation 4.9 into Equation 4.10:

$$\mathbf{x}_s = \begin{pmatrix} 1 & 0 & 0 \\ 0 & c_{ig} & -s_{ig} \\ 0 & s_{ig} & c_{ig} \end{pmatrix} \begin{pmatrix} c_\beta c_\phi & c_\beta s_\phi & s_\beta \\ s_\beta c_\phi & s_\beta s_\phi & -c_\beta \\ -s_\phi & c_\phi & 0 \end{pmatrix} \mathbf{x}_r \ , \tag{4.11}$$

which can be expanded into:

$$\mathbf{x}_s = \begin{pmatrix} c_\beta c_\phi & c_\beta s_\phi & s_\beta \\ c_{ig} s_\beta c_\phi + s_{ig} s_\phi & c_{ig} s_\beta s_\phi - s_{ig} c_\phi & -c_{ig} c_\beta \\ s_{ig} s_\beta c_\phi - c_{ig} s_\phi & s_{ig} s_\beta s_\phi + c_{ig} c_\phi & -s_{ig} c_\beta \end{pmatrix} \mathbf{x}_r \ . \tag{4.12}$$

Since the sky projection from the ring-galaxy plane must be the same as the projection from the ring's plane, the matrices in Equation 4.4 and Equation 4.12 can be directly compared. Using the 33 elements of the matrices in Equation 4.4 and Equation 4.12 (i.e. comparing the value in the third row, third column) implies the relation:

$$c_{ir} = -s_{ig} c_\beta \ . \tag{4.13}$$

Similarly, dividing the 13 elements by the 23 elements gives:

$$\frac{s_{\theta r} s_{ir}}{-c_{\theta r} s_{ir}} = \frac{s_\beta}{-c_{ig} c_\beta} \ , \tag{4.14}$$

which can be simplified to:

$$t_{\theta r} = \frac{s_\beta}{c_{ig} c_\beta} \ , \tag{4.15}$$

where the t is a tan function. Note that the sine and cosine terms were not simplified to tan on the right hand side. This was done in order to preserve the θ_r range between 0° and 360°.

Setting $\theta_r = PA_r + 90°$ allows the position angle of the polar ring to be calculated at $PA_g \neq 0$ through:

$$PA_r = \theta_r - 90 + PA_g \tag{4.16}$$

These relations indicate that a polar ring has a limited number of inclinations and position angles that are possible for a given galaxy orientation. For a face-on galaxy, the ring must be edge-on, but its position angle can vary widely (determined by β). For an edge-on galaxy, the ring could be either face-on or edge-on depending on β, but must be inclined ∼90° to the galaxy's surface.

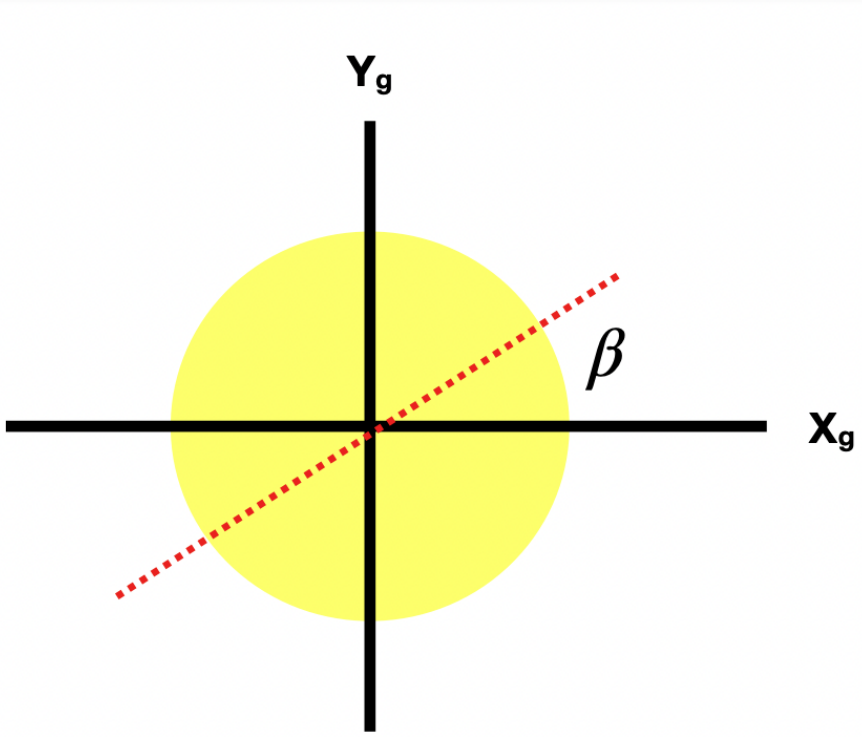

Figure 4.1: Polar ring diagram depicting the angle β (Deg et al., 2023). The yellow circle represents a top-down view of the galaxy, where the dotted red line represents the polar ring viewed edge-on. β is the angle between the approaching side of the galaxy ($+x_g$) and the polar ring.

In order to provide further insight into the detectability of PRGs in HI surveys, numerous plots were generated of model galaxies at different inclinations and observation angles. These moment panel plots were created using the NGC 4632 and NGC 6156 models that were discussed in Section 3.2.1 as a baseline for parameter manipulation. The resolution was altered as well as the inclination and position angle for each ring, using Equation 4.15 and Equation 4.16.

A code was created to generate numerous systematic input files, pass them to MCG, and return mock cubes for seven different inclinations and seven different ring orientation angles. These cubes were created for both model galaxies at resolutions of three, four, six, eight, and ten beams across (BA). These were then processed into moment zero and moment one plots. The main calculation that needed to be conducted to generate a moment zero plot was

converting the units from Jy/beam to $M_{\odot}/pc^2$, which was done by dividing each element in the moment zero matrix by a series of conversion factors.

In order to create the moment one matrix, the moment zero matrix had to be slightly altered. Since each value in moment one was going to be divided by the corresponding value in moment zero, the extremely small moment zero values had to be removed. They would create non-infinite extremely large data points that would impede the display of features at regular galaxy values. Any moment one value less than 0.1 was set to zero, since the infinity values created by a denominator of zero would not be included in the moment one plot.

The two moment maps are essential to determining whether a galaxy has any unique features, such as polar rings. The panel plots are included in Appendix A in their entirety, but a few examples for each PDR1 PRG candidate model are included in Figures 4.2 to 4.9 for reference. The ring orientation angle on the y-axis is the angle between the rotational plane of the polar component and the approaching side of the galaxy with respect to the observer. These figures were intended to be similar to Figure 2.1, however these panel plots do not use the same angles nor the same axes. Figure 2.1 is therefore not a suitable optical comparison for the plots created in this section and included in Appendix A. Each angular resolution produced 49 different mock galaxy observation data cubes that could then be processed for morphology and kinematics.

Figures 4.2 and 4.3 show the moment panel plots for the NGC 4632 model at its detection resolution of 10 BA. This was the highest angular resolution that the moment panel plots were created at, and in the moment zero panel the morphology is exceptionally clear. This is due in part to the high resolution of NGC 4632's original observation, which allowed a model to be generated with more distinct features and greater detail. The moment one panel demonstrates the wide range of potential kinematic plots that could be generated depending on the orientation of the PRG. The panels vary widely, supporting the production of these plots and their use as a detection tool. Cross-referencing these plots during galaxy analyses would allow PRG candidates to be selected more reliably, although at this resolution the morphology panel should clearly show signs of a polar component.

The moment panel plots for NGC 6156 (Figures 4.4 and 4.5) show the galaxy modelled at its detection resolution of 6 BA, which begins to demonstrate the effects of decreased resolution on the morphology panels. The indistinct features of NGC 6156's polar component are due in part to the resolution of the galaxy's original observation. The model was based off of the observations that were unable to resolve the ring in the greater detail of NGC 4632. There are a variety of galaxy asymmetries and distortions that could cause

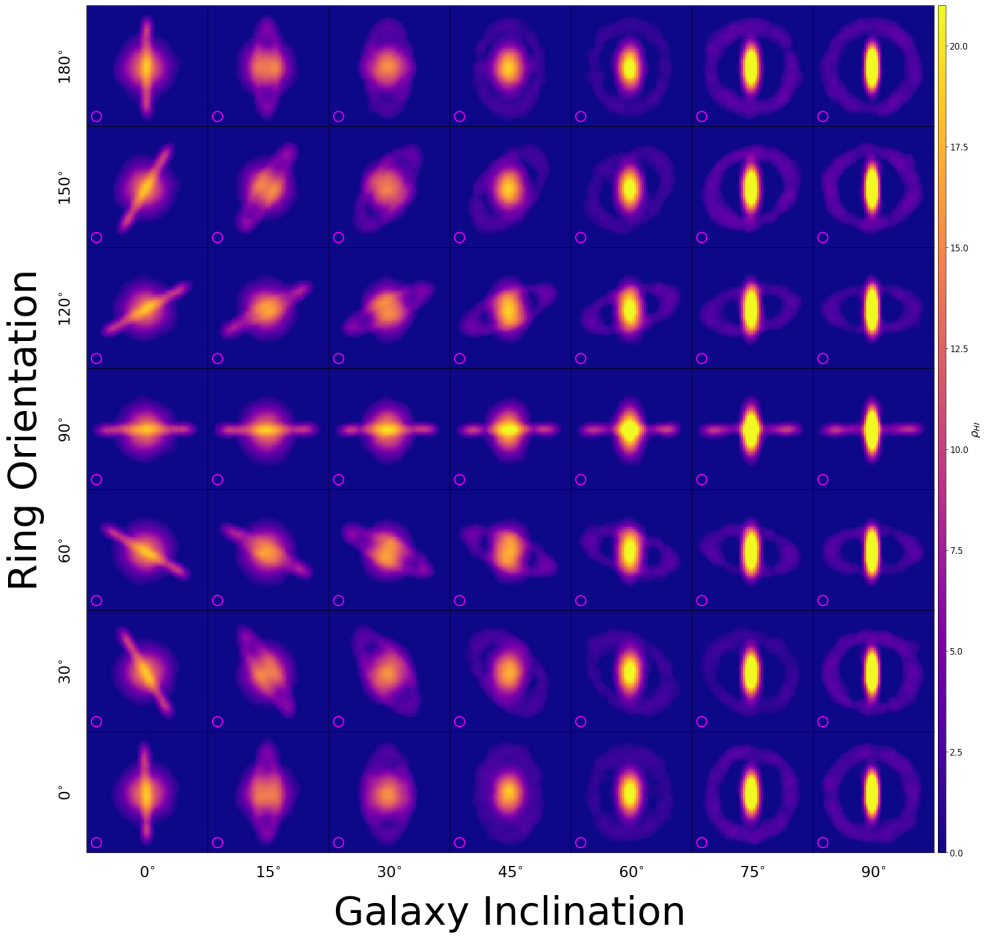

Figure 4.2: Moment zero panel plot for a galaxy model of the PDR1 PRG candidate NGC 4632 at its detected resolution of 10 BA. The colour bar on the y-axis depicts the HI density, ρ_{HI}, in units of $M_\odot/pc^2$. The ring morphology is clearly visible in all panels.

a slightly irregular galaxy morphology in the moment zero panels, so only around half of the panels in this plot could be reasonably identified as a PRG. The kinematics plot contains around the same amount of identifiable panels, but when combined with the morphology panels around 75% of orientations are identifiable at this resolution. This percentage is higher for galaxies with more distinct polar rings, such as NGC 4632.

In the bottom left corner of each panel in the moment panel plots, there is a small magenta circle. This represents the beam size for each of the panels.

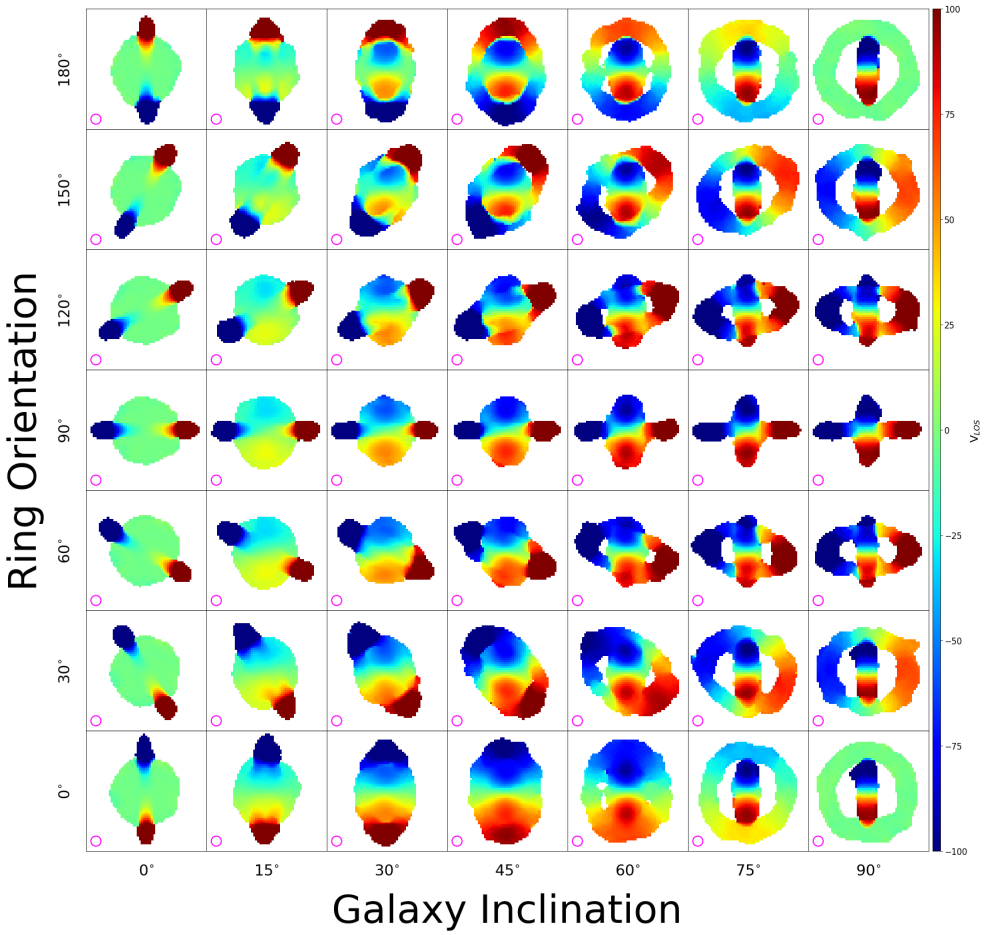

Figure 4.3: Moment one panel plot for a galaxy model of the PDR1 PRG candidate NGC 4632 at its detected resolution of 10 BA. The colour bar on the y-axis depicts the line of sight velocity, V_{LOS}, in units of km/s. The kinematics panels all contain evidence of a polar component, with the exception of the panel located at i=45°, β=0°.

For the panel plots, the circles are the same across every panel in the same figure. In other plots, such as the resolution comparison figures (Figure 4.14 and Figure 4.16), these circles may change depending on the panel. A larger circle indicates a larger beam, and therefore a lower resolution because the galaxy width is fewer beams across.

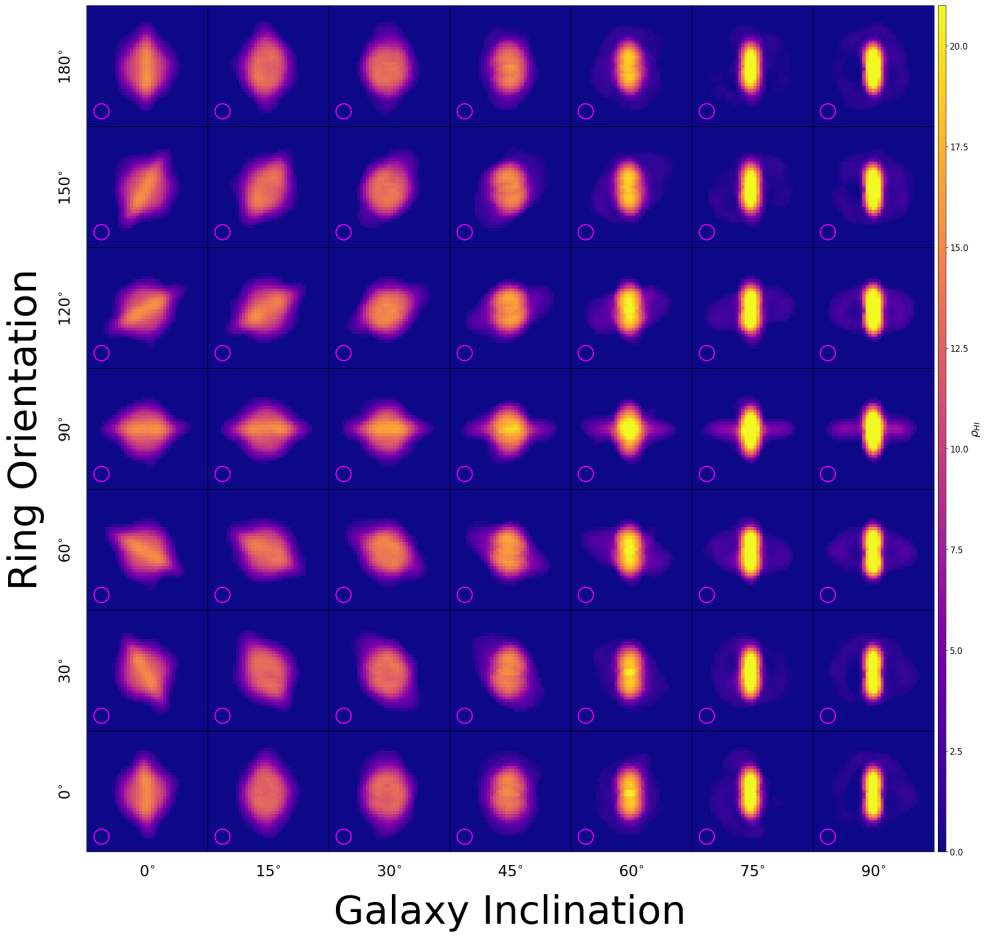

Figure 4.4: Moment zero panel plot for a galaxy model of the PDR1 PRG candidate NGC 6156 at its detected resolution of 6 BA. The colour bar on the y-axis depicts the HI density, ρ_{HI}, in units of $M_\odot/pc^2$. The morphology does not provide many polar ring identifiers, and only approximately half of these panels are identifiable as a PRG.

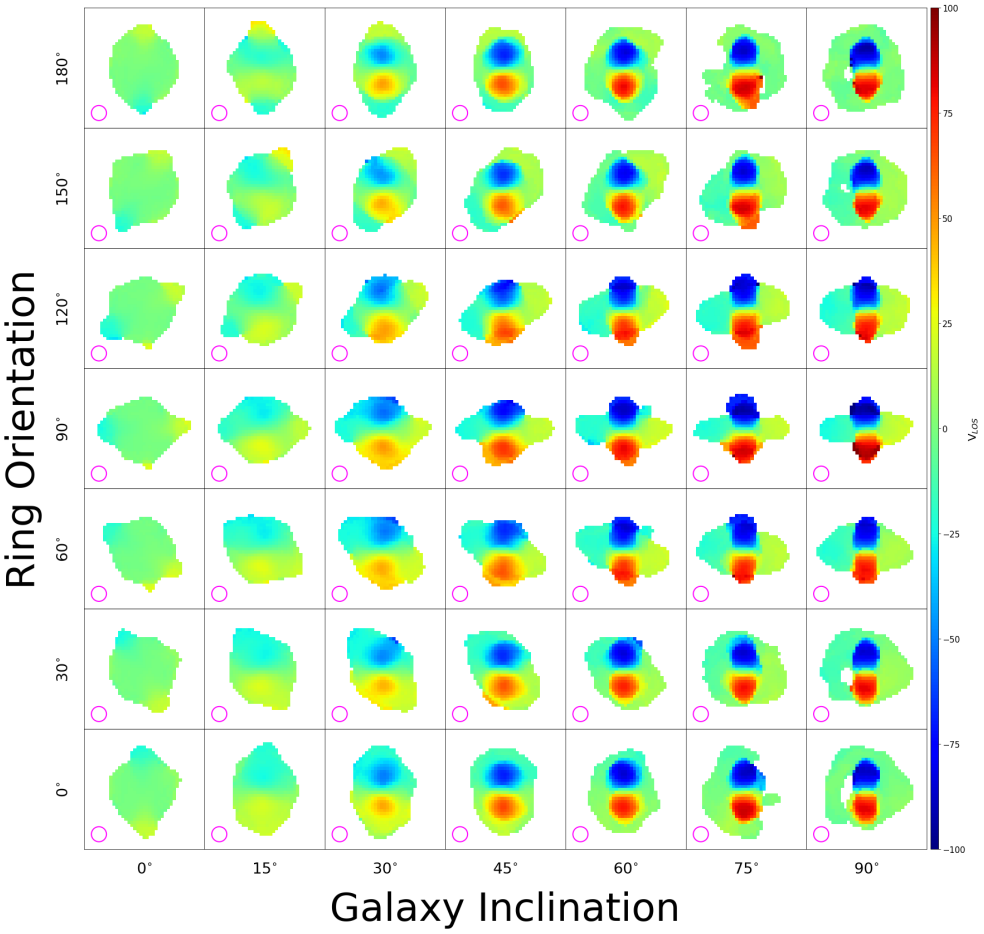

Figure 4.5: Moment one panel plot for a galaxy model of the PDR1 PRG candidate NGC 6156 at its detected resolution of 6 BA. The colour bar on the y-axis depicts the line of sight velocity, V_{LOS}, in units of km/s. Only approximately half of the kinematics panels contain strong evidence of a polar component.

4.2 Effects of Angular Resolution

The angular resolution for each mock galaxy was changed by simulating an observation made across greater distance. Using the dimensions for each ring in the MCG input file, a ratio between the original resolution and future resolution was developed. The size of each ring was reduced or increased by the same factor in order to decrease or increase the mock galaxy's resolution. The noise levels remained at ∼1.67 mJy/beam for each mock observation, and each MCG pixel was set to a value of 6 arcsec^2. The following equation was used to determine the size of the galaxy required to achieve a resolution in beams across:

$$res(w_b) = R_{out} \ , \tag{4.17}$$

where R_{out} is the radius between the outer ring and the centre of the galaxy, res is the resolution in BA, and w_b is the beam width (which was always 30 arcsec for mock WALLABY observations). Then:

$$R_{out_i} = r_{mid} + \frac{1}{2} r_{wid} \ , \tag{4.18}$$

where r_{mid} is the distance from the ring to the galaxy's centre, and r_{wid} is the lateral width of the ring. R_{out_i} is the initial value of the exterior ring's radius. A fraction was then calculated in order to quickly alter the value for each separate ring within the tilted ring model input parameters:

$$f = \frac{R_{out}}{R_{out_i}} \ . \tag{4.19}$$

This fraction was multiplied with the r_{mid} and r_{wid} values for each ring, changing the dimensions by the same ratio in order to scale the entire galaxy equally. R_{out} changed for each iteration, because it was based on the the goal resolution in terms of BA. R_{out_i} remained the same through all the resolutions for each galaxy individually, as it was the initial value of the galaxy model's outermost radius. The initial galaxy values were the ones multiplied by the fraction for each new resolution:

$$r_{mid} = r_{mid_i}(f) \ . \tag{4.20}$$

The new dimensions were submitted as the ring parameter input file into the MCG program, and the orientation code proceeded to alter the observation angles.

Figure 4.6 and 4.7 are the moment zero and moment one panel plots, respectively, for the NGC 4632 model galaxy at a resolution of 6 BA. This is included as a quick reference when compared to the plots at 10 BA (Figures 4.2 and 4.3) and 3 BA (Figures 4.8 and 4.9). The effects of resolution on identifiable features is undeniable, even for a galaxy with a ring as defined as NGC 4632. Just under 60% of the panels in Figure 4.6 were deemed identifiable when examined by three different astronomers who were familiar with PRGs. The ring orientation angle of 90° is identifiable at every inclination, and the inclination angle of 0° is identifiable at every ring orientation angle. Beyond that, each panel is unique in its ability to depict the existence of the polar component. As for Figure 4.7, approximately 80% of its panels contain identifiable features of a polar component. This is why kinematics panels are integral to the detection of gas-gas polar misalignments. The general regions of low identification are the panels at middle inclination angles and low ring orientation angles, where the velocity gradient of the ring is aligned with the main galaxy body.

Figure 4.8 shows the NGC 4632 model galaxy moment zero panel plot at a resolution of 3 BA. It is clear at this resolution that none of the moment zero panels depict an identifiable polar component. Some panels demonstrate unusual morphologies, but even NGC 4632's clearly defined ring cannot be discerned at this resolution. Figure 4.9 shows the NGC 4632 model galaxy moment one panel plot at a resolution of 3 BA, which also contained no identifiable PRG panels. Most of the velocity profiles were relatively consistent with typical red, yellow, green, cyan, blue transitions. The panels at a galaxy inclination of 0° only displayed the systemic velocity (green), and the panels at an inclination of 15° barely differed with a hint of yellow in the bottom portion. Both the moment zero and moment one panel plots for the NGC 4632 model at a resolution of 3 BA had no positively identifiable panels, and the ring for this galaxy was very clearly defined. This is not always the case in PRG detections, which indicates that the moment maps for other galaxies would be equally deceptive at this angular resolution. The moment panel plots for the NGC 6156 model demonstrate this effect, and are included in their totality in Appendix A along with the panel plots for the NGC 4632 model.

It is evident from the moment panel plots that while the models from NGC 4632 and NGC 6156 both demonstrate a polar phenomenon, they look notably different from one another in their moment maps. This represents the diverse presentation of polar components in HI detections. Despite this, there were some features in the moment one maps that seemed to be consistent among the PRG models and were used to identify PRG candidates in PDR2.

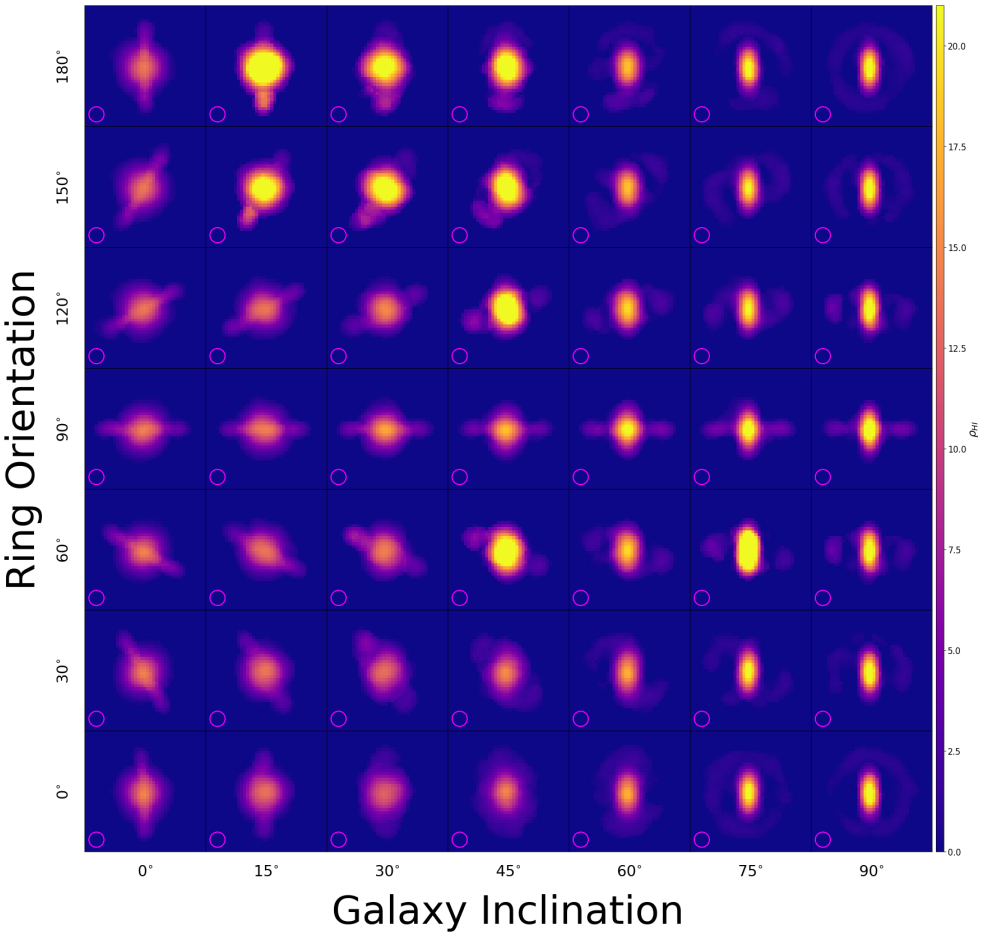

Figure 4.6: Moment zero panel plot for a galaxy model of PDR1 PRG candidate NGC 4632 at a resolution of 6 BA. The colour bar on the y-axis depicts the HI density, ρ_{HI}, in units of $M_\odot/pc^2$. The morphology is much clearer than the corresponding moment zero panel plot for the NGC 6156 model, due to the initial observation resolutions and the nature of the polar components.

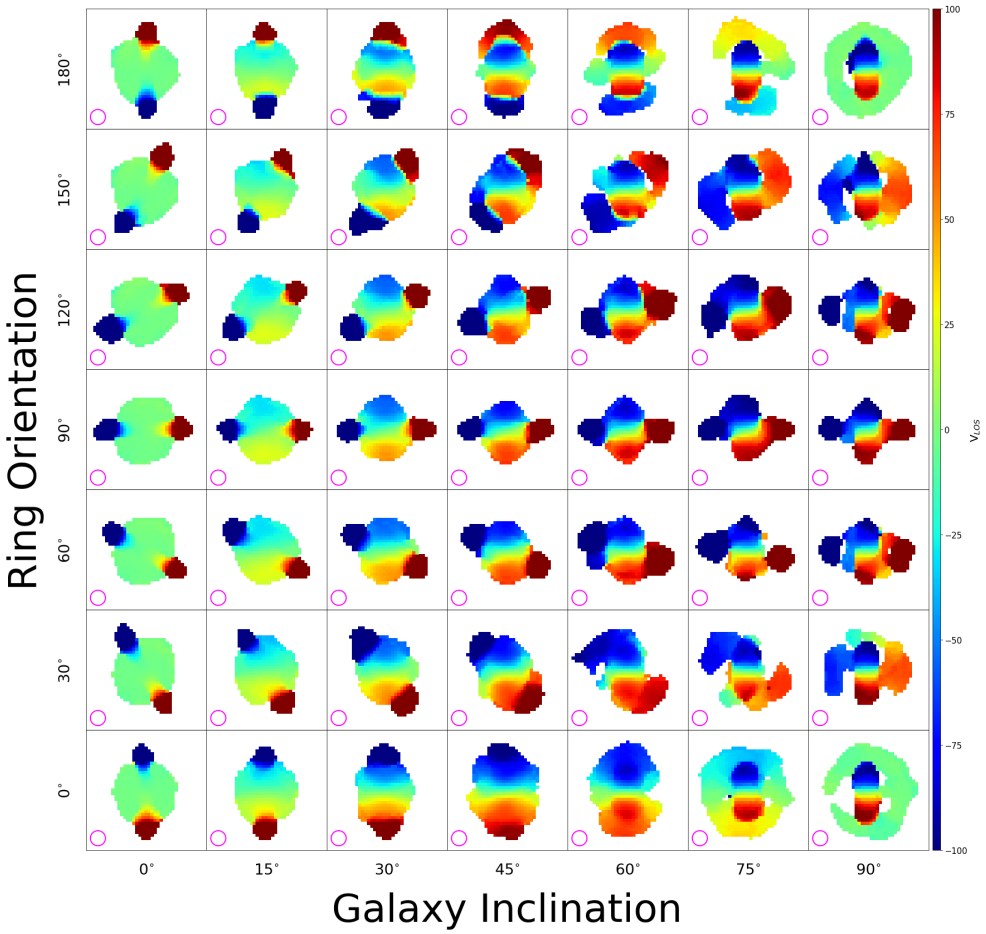

Figure 4.7: Moment one panel plot for a galaxy model of PDR1 PRG candidate NGC 4632 at a resolution of 6 BA. The colour bar on the y-axis depicts the line of sight velocity, V_{LOS}, in units of km/s. The majority of these kinematics panels are identifiable as polar ring candidates.

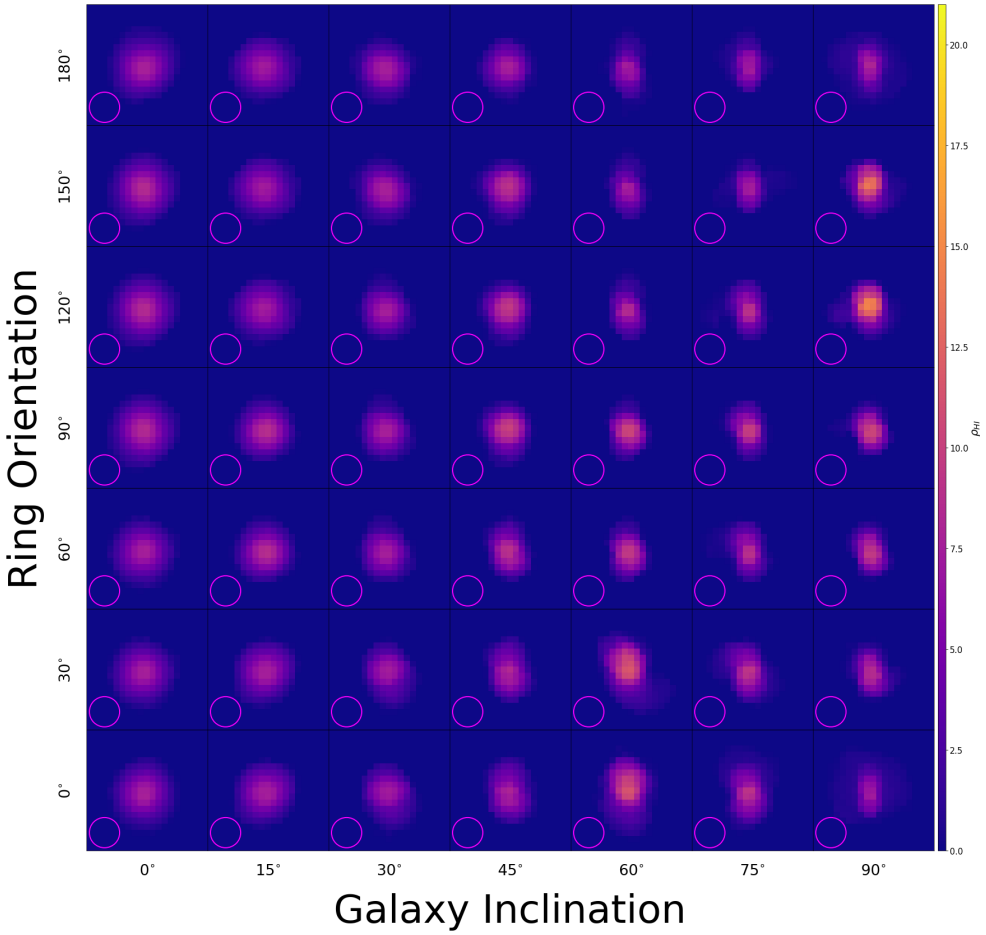

Figure 4.8: Moment zero panel plot for a galaxy model of PDR1 PRG candidate NGC 4632 at a resolution of 3 BA. The colour bar on the y-axis depicts the HI density, ρ_{HI}, in units of $M_\odot/pc^2$. It is clear that none of the morphology panels provide reliable evidence of a polar component at this resolution.

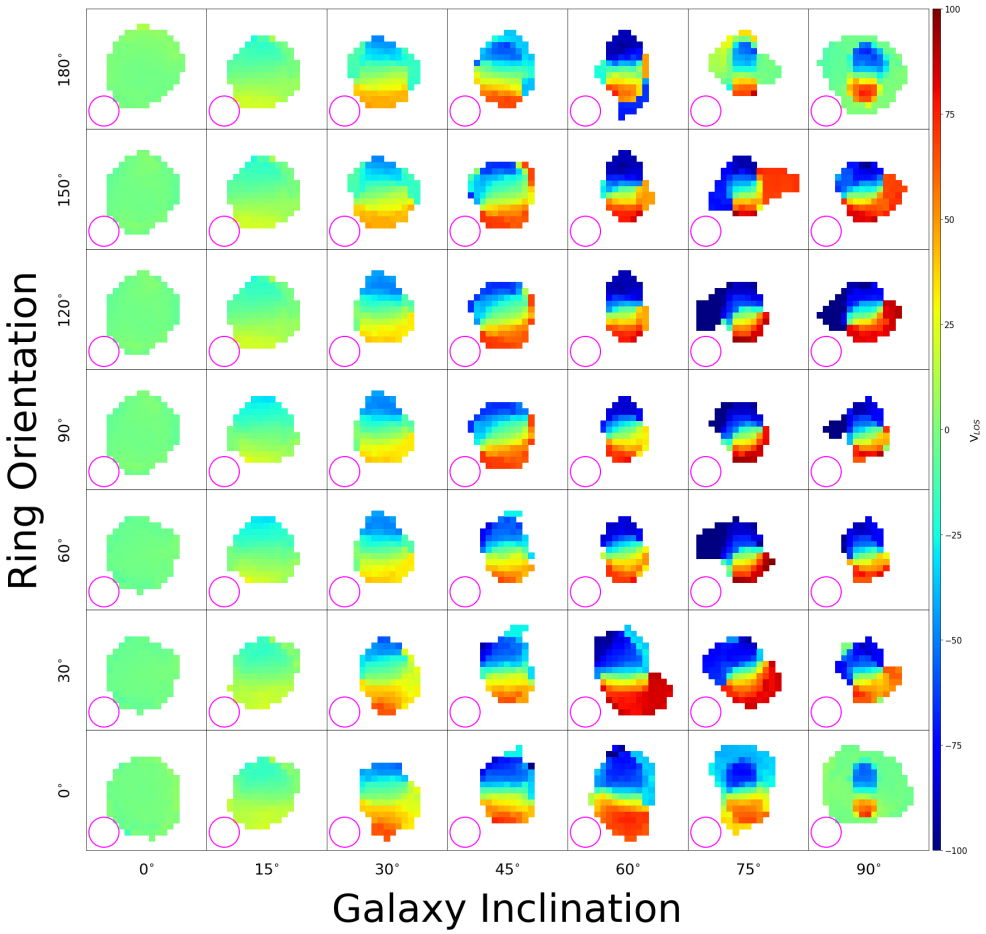

Figure 4.9: Moment one panel plot for a galaxy model of PDR1 PRG candidate NGC 4632 at a resolution of 3 BA. The colour bar on the y-axis depicts the line of sight velocity, V_{LOS}, in units of km/s. These kinematics panels do not provide reliable evidence regarding the presence of a polar component.

4.3 PRG Signatures

One of these signatures was a green main galaxy body with two dots on the edges, coloured red and blue. This pattern is exhibited by a galaxy being viewed from directly above, such that its velocity does not vary across the main component and only the systemic velocity is able to be observed. If there is a polar component, the ring in this orientation would be levelled edge-on and appear on the kinematic diagram with a redshifted and blueshifted section. Examples of this signature are included in Figure 4.10.

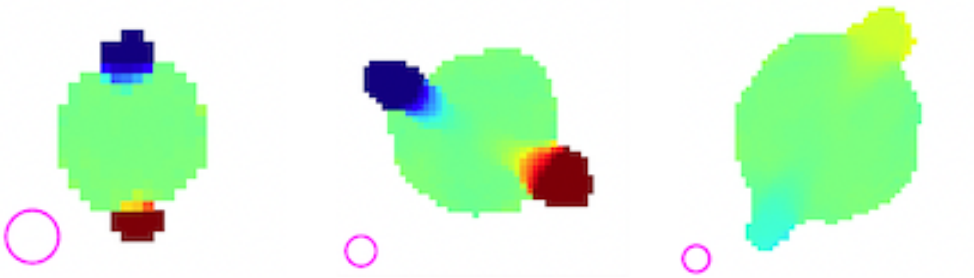

(a) NGC 4632 at 4 BA, i = 0° β = 0°.

(b) NGC 4632 at 8 BA, i = 0° β = 60°.

(c) NGC 6156 at 10 BA, i = 0° β = 150°.

Figure 4.10: Moment one panels that show a low galaxy inclination PRG signature. The neutral green represents the main galaxy body travelling at systemic velocity while the red and blue circles represent the approaching and receding arms of the polar ring. The yellow and cyan dots in (c) are the same concept, except observed more faintly.

Another signature that was used to identify PRG candidates was the juxtaposition of two velocities in a symmetrical manner. At galaxy inclinations between 30° and 60°, and ring orientation angles between 120° and 180°, these contradictions occur. The velocity gradient that had been smooth in the main galaxy body suddenly reverses without any intermediate sections. The gas that was observed moving towards the observer undergoes a nearly instantaneous shift and moves away from the observer. This indicates that there is a ring on the edges of the main galaxy body that is moving in a fashion kinematically opposed to that of the main galaxy body. This feature strongly indicates the presence of a kinematically misaligned polar component of HI gas, and some examples of this signature are included in Figure 4.11.

An evident feature of a polar ring is the space between the main galaxy body and the gaseous ring. This is typically only a viable method of identifying

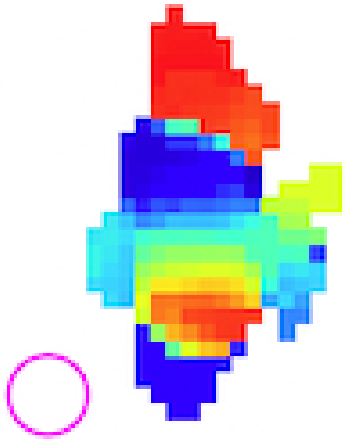

(a) NGC 4632 at 4 BA, i = 60° β = 180°.

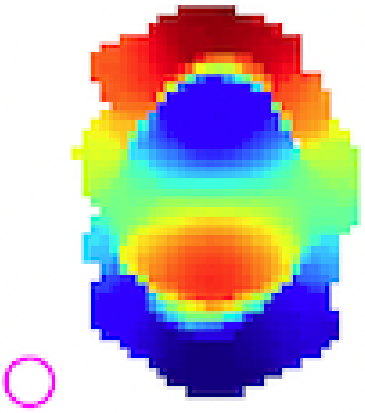

(b) NGC 4632 at 8 BA, i = 45° β = 180°.

Figure 4.11: Moment one panels that show velocity juxtaposition as a PRG signature. Velocity juxtaposition is where the gradient is broken by an opposite colour, i.e. blue transitioning immediately into red or vice versa.

PRG candidates at higher resolutions that possess polar rings rather than polar disks, since the low resolution observations are unable to detect the space between the gaseous disk and the main galaxy body. When this space can be resolved, it provides a convincing feature in the moment maps that supports the presence of a polar component. These features can sometimes be erroneously recreated by masking errors, so their reliability depends heavily on the resolution of the detection and the symmetry of the identifying feature. Some examples of the ring shape in moment one maps are included in Figure 4.12. This feature would reflect the morphology displayed in the moment zero plot.

Another PRG indicator is when the kinematics plot resembles an addition sign at a ring orientation angle of 90°, as shown in Figure 4.13. At higher resolutions, the horizontal component can have a velocity gradient as well as the vertical component. At reduced clarity conditions the horizontal component tends to display in green. NGC 6156 has a green horizontal component because the model was created to be accurate at a lower resolution where the galaxy was observed. Even at higher resolutions, the quality of the original observation weakens the features being mapped. This addition sign feature is difficult to rely upon at low resolutions because of noise and masking. Since the galaxy observation is so small, minimal noise could be included in the

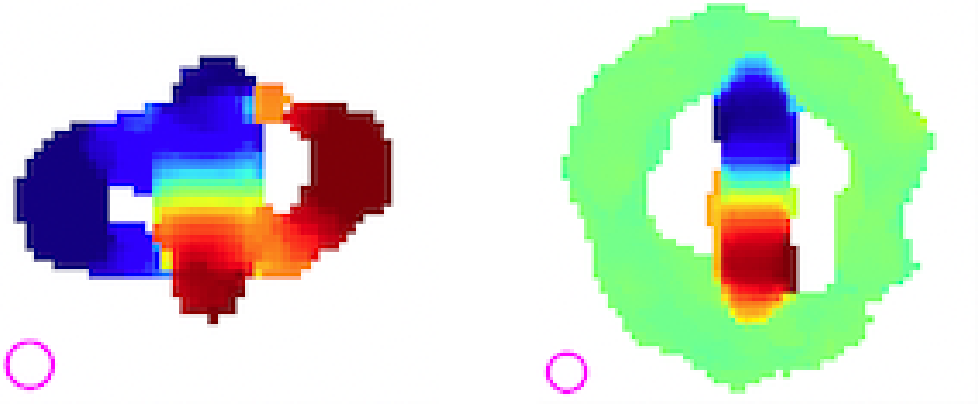

(a) NGC 4632 at 8 BA, i = 75° β = 120°.

(b) NGC 6156 at 10 BA, i = 90° β = 0°.

Figure 4.12: Moment one panels that a show ring structure PRG signature. These diagrams clearly depict the main galaxy body with a separate ring component, which is not expected to be a common observation in real data given how easily noise could obscure the vacant areas near the centre.

mask and form the horizontal component in a convincing manner. Future analyses could model regular galaxies at low resolutions across the different orientations in order to demonstrate which features are truly unique to PRGs within that observation range.

Even at high resolutions, there are panels in the moment panel plots that are not identifiable as PRGs. NGC 4632 was a well resolved galaxy, so the model was better defined than the NGC 6156 model. Despite this, there remains an unidentifiable kinematics panel in the highest resolution panel plot. At a galaxy inclination of 45° and a ring orientation angle of 0°, the velocity dispersion resembles a normal gradient. Without the use of the corresponding morphology panel, that system orientation obscures the evidence of a kinematic misalignment. At lower resolutions, the morphology becomes less reliable and that panel may not be identifiable at all.

Figure 4.14 shows a resolution comparison for both NGC 4632 and NGC 6156 at this orientation that offers very little kinematic evidence of a polar component. In the NGC 4632 moment maps (top), the galaxy could not be identified from its morphology or kinematics panels below 8 BA. Even the moment zero at 8 BA would be difficult to confirm as a PRG when examined beside the moment one panel that indicates a normal velocity dispersion. This

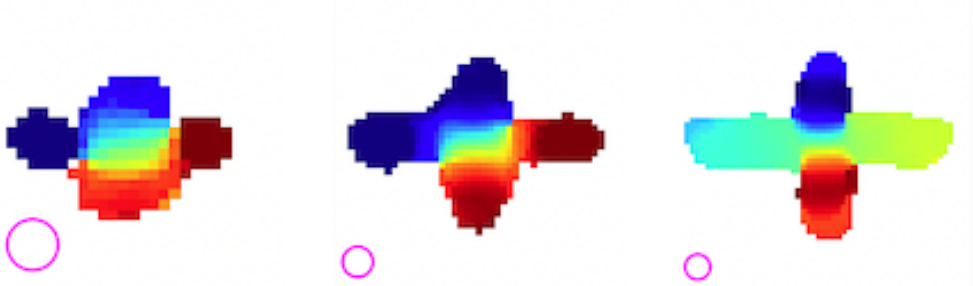

(a) NGC 4632 at 4 BA, i = 60° β = 90°.

(b) NGC 4632 at 8 BA, i = 75° β = 90°.

(c) NGC 6156 at 10 BA, i = 90° β = 90°.

Figure 4.13: Moment one panels that show the addition sign PRG signature. At high galaxy inclination angles and 90° ring orientation angles, both the ring and the main galaxy body contain velocity gradients that intersect through their centres. NGC 6156's ring component in (c) is a cyan-green-yellow gradient because of the original ring's fainter observation.

orientation in NGC 6156 (bottom) is perhaps easier to identify because of the kinematics panels. None of the moment zero maps are conclusive, although the high resolution panels support a PRG theory when viewed in conjunction with the moment one maps. The redshifted and blueshifted elements in the centre of a systemic velocity component is an indicator of a kinematic misalignment. NGC 6156's less distinct gas ring is easier to identify at this orientation than the more detailed ring detected on NGC 4632.

4.3.1 Colour Map Selection

The moment maps taken from Deg et al. (2023) are a different set of colours than those in the rest of this thesis. This is due to the different applications of the plots. In the Deg et al. (2023) paper, the black and grey moment zero map appears more binary and shows exactly where the gas is present or absent. The colour scheme for the moment one map was also specifically designed for reader perception. The red tones were made cooler and the blue tones were made warmer such that the red toned parcels give the impression of moving into the paper and the blue toned parcels give the impression of moving towards the reader. Since this is the motion of the gas relative to the observer, these colour maps were used when the galaxies were being presented.

These were not the colour maps used in this analysis because those figures prioritize demonstration rather than identification through the accentuation of individual features. In Figure 4.15, it is clear that the 'plasma' colour map

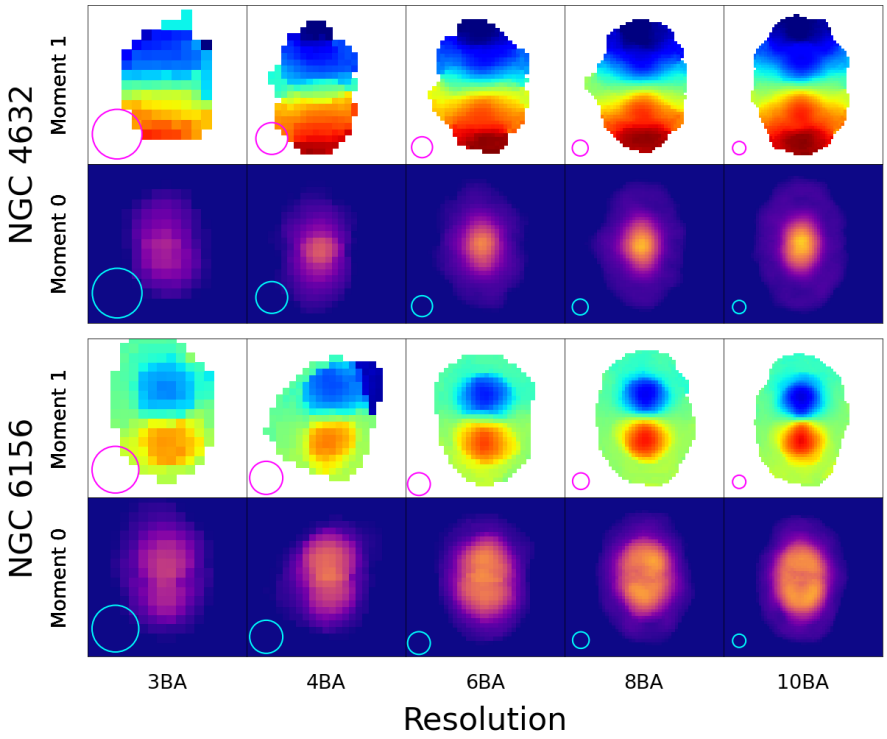

Figure 4.14: Resolution comparison of NGC 4632 and NGC 6156 models at the orientation of i = 45° and $\beta = 0°$. The NGC 4632 model was not identifiable in moment one at this orientation across any of the resolutions, and was only identifiable in moment zero at a resolution of 8 BA.

shows more details of the diffuse gas in the ring component. These details are integral to the identification of polar signatures, so the 'gray' colour map was discarded. The custom kinematics maps were very useful for the reader to visualize the motion of the gas particles in Deg et al. (2023), however it did not have the same detailed range of colours as the 'jet' colour map. The multiple colours and clear gradient across shades allowed for specific features in the moment one map to be identified. Since the target was to identify kinematic anomalies, the colour map with the more obvious velocity changes was selected.

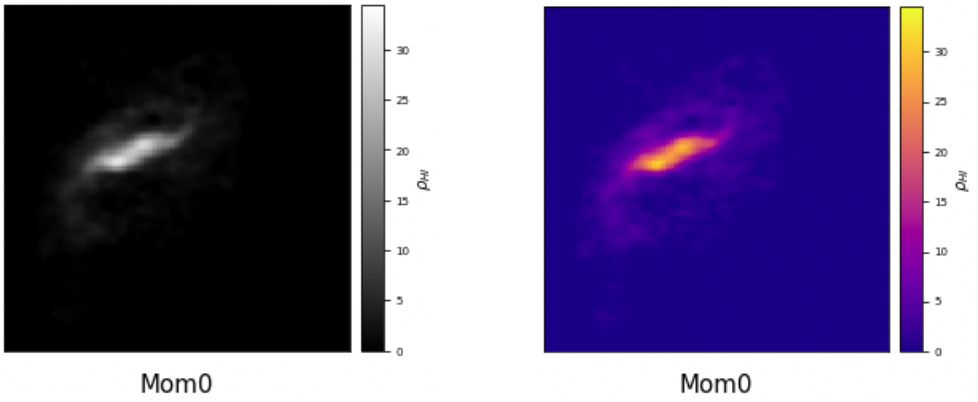

(a) Moment zero diagram of PRG candidate using 'gray' colour map.

(b) Moment zero diagram of PRG candidate using 'plasma' colour map.

Figure 4.15: Comparison of colour maps for the moment zero diagrams. 'Gray' (a) did not show as much of the HI gas as 'Plasma' (b) was able to, which is why it was selected for PRG analyses.

4.4 Detectability Fraction

Figure 4.16 shows each galaxy at the same orientation observed at different angular resolutions in order to demonstrate that the lower resolution plots are not reliable indicators of polar morphology or kinematics. The red X's mark the panels that could not be positively identified as PRGs, and the green check marks were given to panels that were able to be identified as potential PRGs.

The moment panel plots at each resolution were assessed for PRG detectability by three WALLABY collaborators including the author, and the moment maps for each inclination and orientation were given a pass or fail grading on whether they could be identified as a PRG. The detectability estimates were done conservatively, with the intentions of imitating the detection fraction that would be found by unfamiliar astronomers as closely as possible. This meant that panels with slightly questionable identifiers were given a fail grade. Figure 4.17 demonstrates the detectability fraction that was calculated using these plots on the bottom panel. The dotted lines represent the detectability fraction generated from the moment zero panels, and the dashed lines represent the detectability fraction generated from the moment one panels, when each were viewed independently. The solid lines represent the detectability fraction generated at each orientation when the moment zero and moment one maps were viewed together, which best replicates the gen-

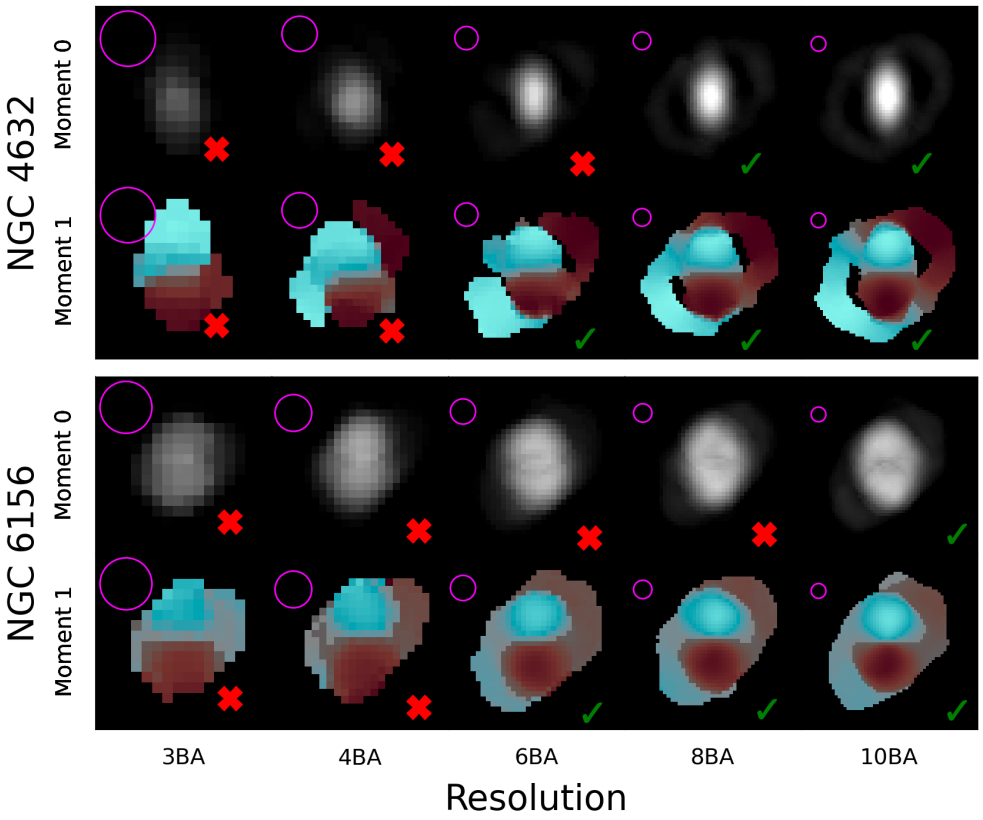

Figure 4.16: Resolution comparison plot for the galaxy models of both PDR1 PRG candidates at a constant orientation (Deg et al., 2023). The galaxies are depicted at the i=45° β=30° orientation with moment zero in the top row and moment one on the bottom row for each candidate. The red X's indicate panels that could not be identified as PRGs, and the green check marks indicate panels that provided sufficient evidence to be identified as potential PRGs.

uine process of PRG identification. Despite the detectability fraction for each galaxy model varying considerably during individual moment panel assessments, the solid lines demonstrate that the identification of polar rings is relatively consistent when the moment zero and moment one maps are examined together. The black line in Figure 4.17 represents the average of the solid lines for both PRG models, and was used to interpolate the intermediate detectability fraction values at the untested resolutions of five, seven, and nine beams across.

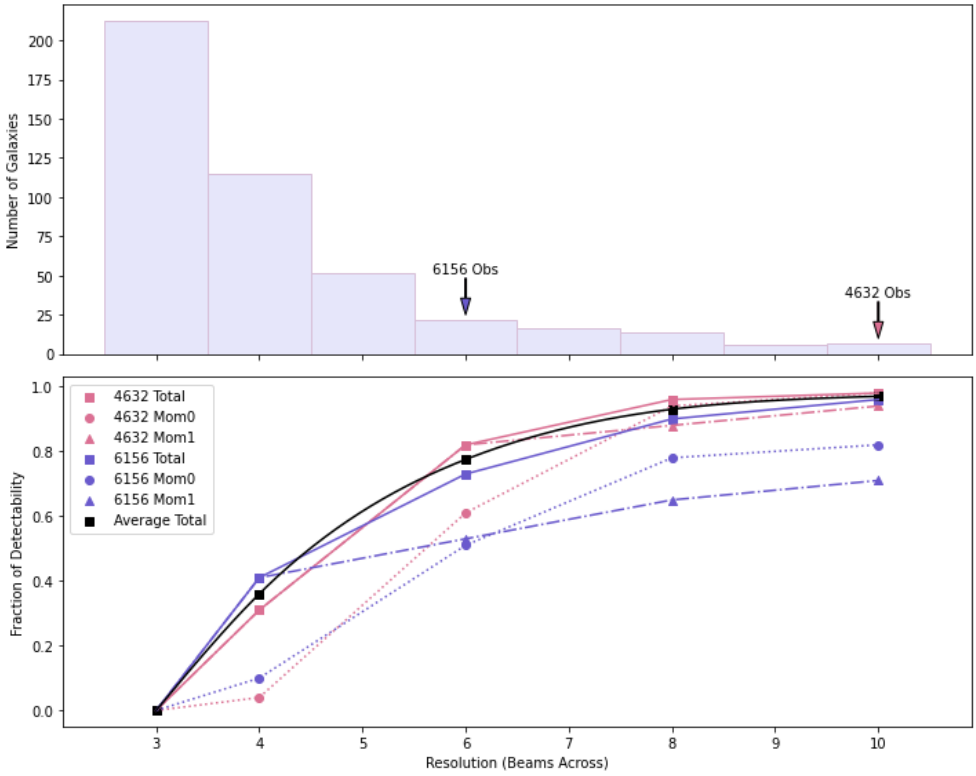

Figure 4.17: Detectability fraction of PRG models at different angular resolutions (bottom), with separate dashed lines for each galaxy model's morphology and kinematics. The solid lines represent the combined examination of panels from both moment zero and moment one, and the black solid line represents the average total between both galaxy models. The galaxy resolution distribution (top) demonstrates how many objects were detected in PDR1 at each resolution in order to determine the weighted incidence.

The top panel in Figure 4.17 shows the number of galaxies detected in PDR1 at each resolution, as listed in the WALLABY Data Release catalogues. The detection bins are aligned with the detectability fraction of that resolution on the bottom panel. It was clear from this figure that the majority of PDR1 objects were detected in the 3 BA range, which had a detectability fraction of zero. None of the moment maps at any orientation demonstrated clear signs of a polar component that could be positively identified when detected at 3 BA. This figure depicts how many existing PRGs cannot be identified due to the resolution of their detections.

4.4.1 PDR1 Incidence Calculations

The incidence of PRGs in each phase of the WALLABY survey was calculated using the following equation:

$$f_i = \frac{N_{detected}}{\sum_b N_b D_f} \ , \tag{4.21}$$

where f_i is the incidence of PRGs, $N_{detected}$ is the number of PRGs identified in the data set, N_b is the number of elements in each bin, D_f is the detectability fraction at each bin's resolution, and $\sum_b$ sums the product of the last two variables across all the bins.

Resolution (BA)	Detectability Fraction	Number of Detections	Product
3	0/49	212	0
4	18/49	115	41
5	30/49	52	32
6	38/49	22	17
7	43/49	16	14
8	46/49	14	13
9	47/49	6	6
10	48/49	7	7
		Sum	130

Table 4.1: Incidence fraction calculations for PDR1. The detectability fraction (as displayed in Figure 4.17) was multiplied by the number of detections in order to determine the product, which was then summed to generate the denominator for Equation 4.21. The product column is rounded to the nearest integer. Some of the detectability fractions may have had a non-whole numerator due to the averaging of NGC 4632 and NGC 6156 data, and the interpolation of intermediate data points. In this table, the numerators of the detectability fraction are also rounded to the nearest integer.

Using the values in Table 4.1, the incidence of PRGs in PDR1 could be calculated as:

$$f_i = \frac{2}{129.98} = 0.0154 \ , \tag{4.22}$$

which translates to a gas-rich PRG incidence of $\sim$1.5%. If the methodology is accurate, a similar incidence percentage should be calculated with the data from PDR2.

4.5 Summary

This chapter presented the sequence and methodology of the PRG incidence calculations used with WALLABY PDR1 data. The moment panel plots were described and included in Section 4.1, and the effects of angular resolution were demonstrated in Section 4.2. Some of the PRG signatures that were used to identify PRG candidates from their moment maps were highlighted in Section 4.3, before the detectability fraction was calculated in Section 4.4. The incidence of gas-rich PRGs in PDR1 of the WALLABY pilot survey was estimated to be $\sim$1.5%. The methodology outlined in this chapter is applied to WALLABY PDR2 data in Chapter 5.

5 Application to PDR2

Chapter 4 introduced the moment panel plots and detectability fraction that are integral to the weighted incidence estimate of gas-rich PRGs in WALLABY pilot fields, and estimated this incidence to be ∼1.5% in PDR1. This chapter applies the same methodology to PDR2 data after examining the detections to identify PRG candidates. Section 5.1 introduces three PRG candidates from the PDR2 data, and compares their morphology and kinematics to panels from the moment panel plots introduced in Section 4.1. Section 5.2 calculates the incidence of gas-rich PRGs in WALLABY PDR2, which is compared to the incidence found using PDR1 data in Section 5.3. Section 5.3 also discusses the results and limitations of this thesis while highlighting areas for future study.

5.1 PDR2 PRG Candidates

There were many galaxies in PDR2 that had unique morphology and kinematic markers that suggested the presence of misaligned features. In order to assess the moment plots of the PDR2 detections, potential PRG candidates were compared to the moment panel plots of the models for PDR1 PRGs NGC 4632 and NGC 6156 that corresponded to their observation resolution (see Section 4.1). A PRG candidate was identified if there were similarities between the observed galaxy and the modelled galaxy at a certain orientation or orientation range. The orientation had to match for both the moment zero and moment one plots before it could be deemed a reasonable comparison. Three PDR2 galaxies exhibited significant features of polar rings, to varying degrees of certainty. These galaxies were selected as polar ring candidates until further research can be done that examines them more closely. Note that the moment maps of the PDR2 detections are slightly compressed in Figures 5.2, 5.5, 5.8, and 5.11 in order to facilitate comparison to the PRG model moment maps. The PDR2 PRG candidate galaxies also had their position angles altered by 90° in Figures 5.8 and 5.11 to accentuate the similarities between their moment

maps and those of the PRG models.

The first candidate, WALLABY J125548+041805 (W1255), is the most convincing and its moment maps are presented below in Figure 5.1. Due to the galaxy's orientation and the position of the ring, the moment one map shows a regular velocity gradient. The moment zero map, however, shows a main galactic body with a displaced ring of gas surrounding it. At a resolution of 17 beams across (BA), as listed in the PDR2 detection catalog, this ring of gas is relatively distinct. At a lower resolution, this galaxy may not have been able to be identified as a PRG candidate due to the absence of signatures in the moment one map.

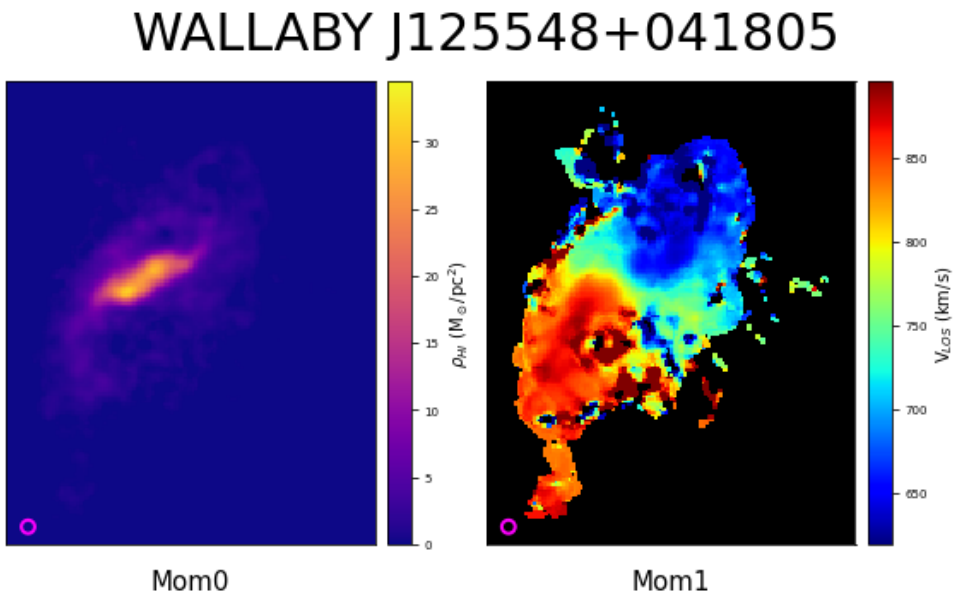

Figure 5.1: WALLABY galaxy J125548+041805, a PRG candidate from PDR2, detected at a resolution of ∼17 BA. The moment zero plot (left) demonstrates a clear gaseous misalignment while the moment one plot (right) shows little evidence of anomalous gas.

Figure 5.2 shows the moment zero plot for W1255 compared to a panel from the NGC 4632 model at a resolution of 10 BA. This galaxy was determined to approximate the model galaxy's plots at an inclination of $i = 30°$ and a ring orientation angle of $\beta = 0°$. Figure 5.2 also shows the moment one plot from the same candidate beside the moment one panel from the NGC 4632 model at the same observation conditions. The observed galaxy may be tilted compared to the modelled plots because the position angle of the sys-

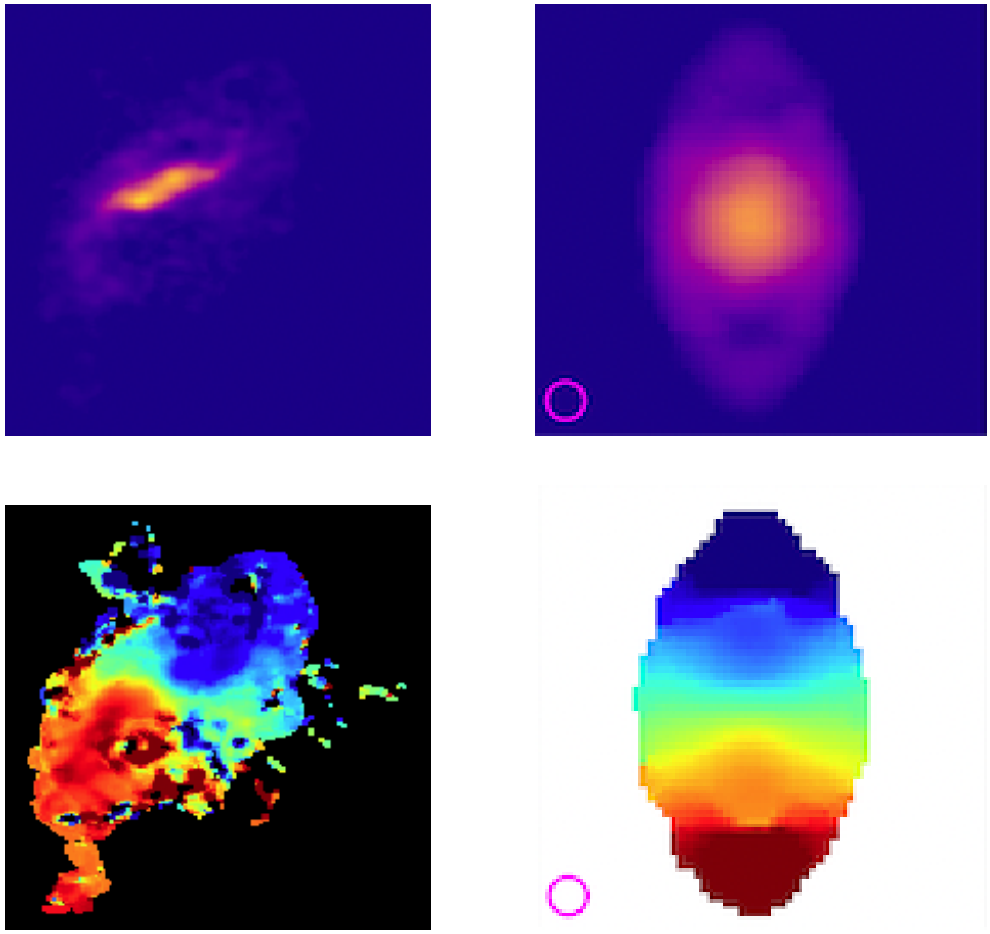

Figure 5.2: Comparison of moment zero (top) and moment one (bottom) maps for W1255 (left) and a panel from the NGC 4632 model's moment zero panel plot (Appendix A) at a resolution of 10 BA (right) with i = 30° and β = 0°. Both moment zero maps depict a bright central component with a fainter ring that extends in an oblong shape beyond the main galaxy body, leaving a gap above and below. Both moment one maps depict a relatively consistent velocity gradient without compelling evidence of a polar component.

tem does not affect its morphology or kinematics. This comparison strongly supports the presence of a kinematically misaligned gaseous polar component in W1255.

W1255 cross-matches to the well-known galaxy NGC 4808, and the Legacy

Survey DR10 (Dey et al., 2019) image of the object is included in Figure 5.3. It is clear that NGC 4808 is a spiral galaxy, rich with blue star forming regions in its arms and a yellow central component indicating an older star population. Recall that the polar rings being investigated in this study are gas-gas misalignments, which are invisible in the optical wavelength range unless the gaseous ring begins forming stars. The lack of polar components in the Legacy images suggest that if a stellar counterpart to the HI ring is present, it is very faint.

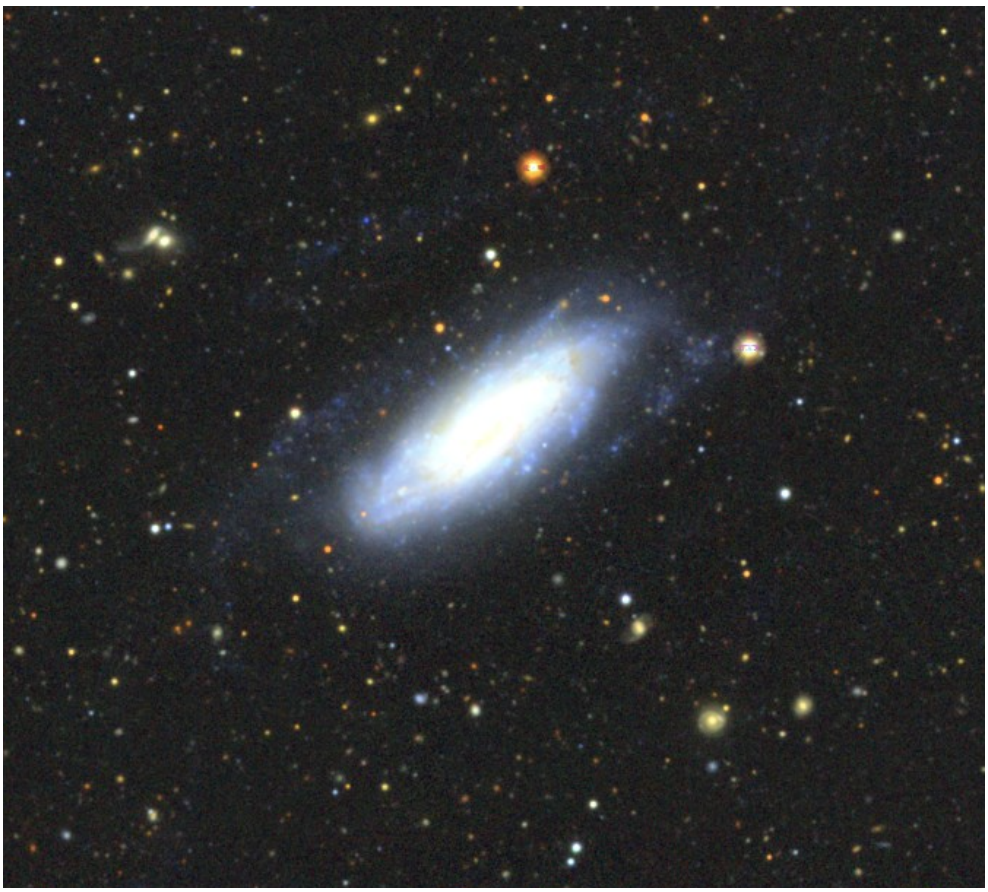

Figure 5.3: NGC 4808 (W1255) as viewed in the optical by DECaLS (Dey et al., 2019).

The second PRG candidate is slightly less convincing, but nonetheless exhibits reasonably clear signatures of a kinematic misalignment. Moment zero and moment one maps for WALLABY J130056-135640 (W1300) are presented

in Figure 5.4. In the moment zero panel, a ring-like structure can be seen around a main galaxy component. The resolution being 10 BA supports that the observations are accurate, and that this galaxy does possess a misaligned component. The kinematic diagram supports the presence of a kinematically misaligned gas ring as well. The green component in Figure 5.4 (gas near the systemic velocity) has a ring-like shape, and appears to be rotating in a plane separate to the main galaxy that shows its own velocity gradient in the East-West direction. However, there are gaseous shreds above and below the ring that could indicate that the features being observed are simply noise.

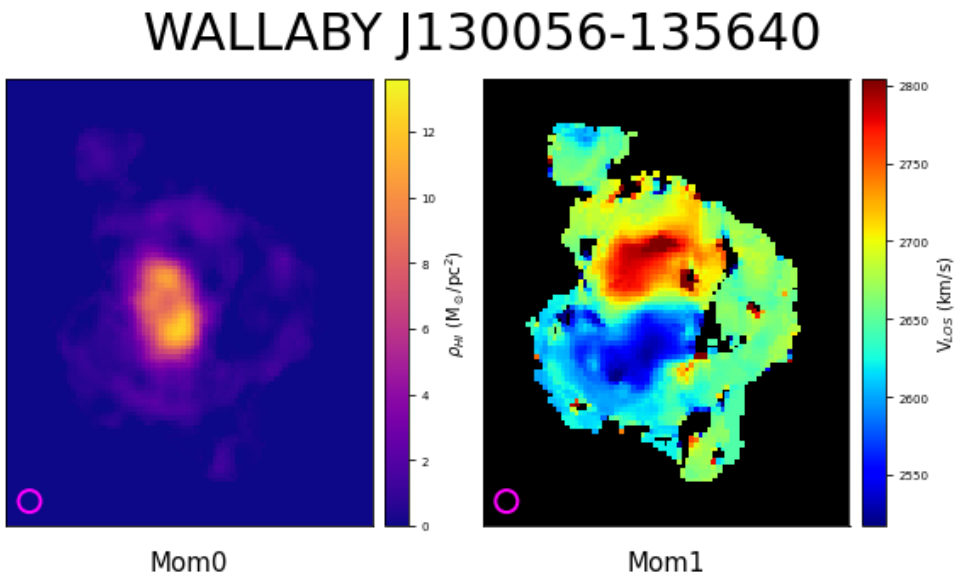

Figure 5.4: WALLABY galaxy J130056-135640 from PDR2, detected at a resolution of ∼10 BA. The moment zero plot (left) shows a nearly complete ring structure surrounding the main galaxy body, and the moment one plot (right) demonstrates that the ring structure is rotating in a different plane than the main galaxy body.

The ring of W1300 was less well defined, as was the case for NGC 6156, so the moment map comparison was better suited to the NGC 6156 model galaxy at 10 BA. Figure 5.5 compares the moment maps for W1300 to moment maps from the NGC 6156 model's panel plot at an inclination of 90° and a ring orientation angle of 60°.

It was expected that the model panels would not match the observations exactly, for a variety of reasons. The models have smooth, circular rings

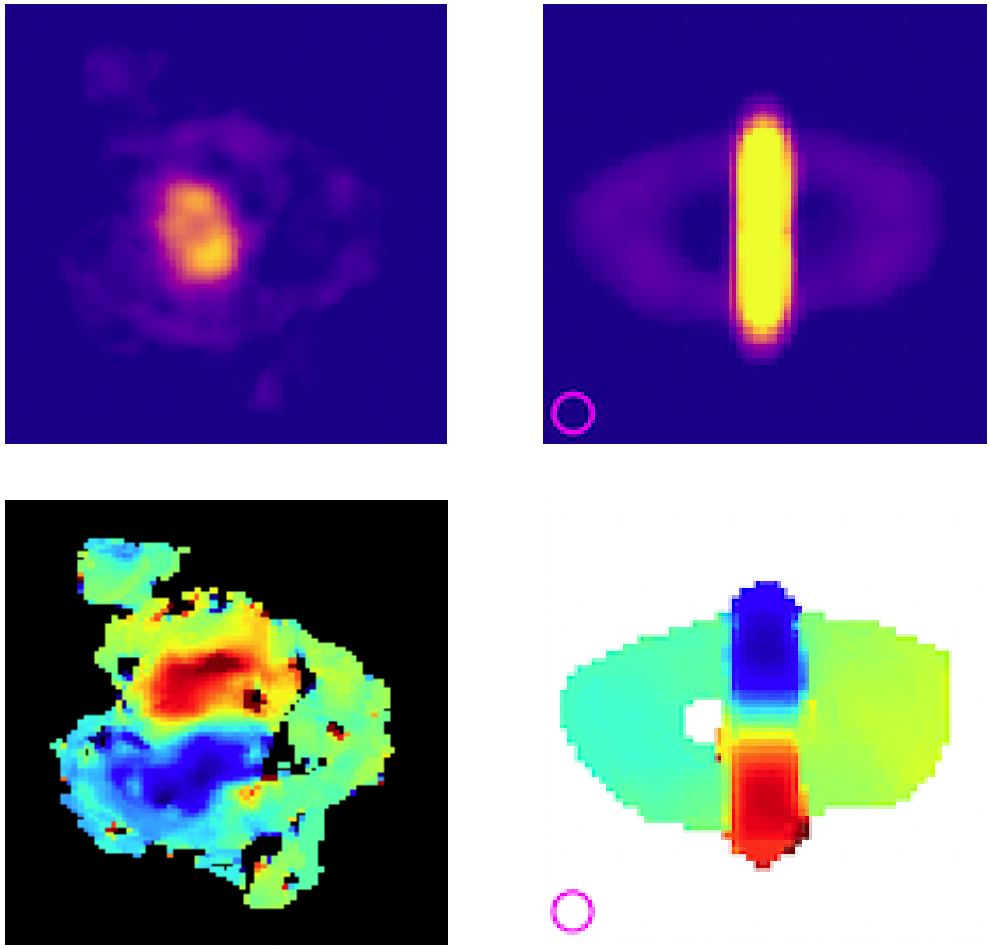

Figure 5.5: Comparison of moment maps for W1300 (left) and panels from the NGC 6156 model's moment panel plots (Appendix A) at a resolution of 10 BA (right) with i = 90° and $\beta = 60°$. Both moment zero (top) maps depict a bright central component surrounded by a wide oval ring, leaving gaps on both sides of the main galaxy body. Both moment one (bottom) maps depict a central component consisting primarily of blue and red sections, with a neutral green shaded ring component that trends slightly towards yellow on one side.

inclined at precisely 90° with a uniform dispersion of gas. There is a constant level of noise, and no other objects that could hinder observation. In the WALLABY detections, a certain amount of deformation does not indicate the

lack of a polar component. Many polar rings are elliptical rather than perfect circles, and they are not always inclined at exactly 90° from the main galaxy body. Real data cubes are not always as cleanly masked as the galaxy models were, since there could be varying gaseous interference or abnormalities during observation.

W1300 cross-matches to NGC 4899, and an optical image from the Legacy Survey is shown in Figure 5.6. The optical image clearly depicts a spiral galaxy with a yellow centre and blue arms, indicating active regions of star formation similar to NGC 4808.

The third candidate is the least convincing, but contains sufficient potential to be considered a PRG candidate. The moment zero and moment one maps of WALLABY J130943-163617 (W1309) are presented in Figure 5.7. The kinematics of this galaxy are definitely unusual and possibly consistent with a polar disk. There is evidence of green systemic velocity gas with redshifted and blueshifted components superimposed, which indicates two separate planes of rotation. The tail-like portions of the red and blue components were deemed a unique feature that is neither evidence for nor against the presence of a polar disk. The misaligned portion also fades from green to yellow on the side with the red component, and from green to cyan on the side with the blue component. This small detail indicates that there may be something more than simple noise or interference occurring in this observation. In the morphology panel, there is a dense central component surrounded by a sparse disk of gas. This could be noise, however a resolution of 11 BA is typically reliable in terms of PRG detections (see Figure 4.17). Future studies and a more in-depth observation of W1309 could confirm the presence of a polar component.

Despite being observed at 11 BA, W1309's misaligned gaseous component was much less complete during its observation which made finding an exact comparison difficult. It also has some unique features that extend outward from the main galaxy that alters its appearance. Nevertheless, Figure 5.8 shows the third PRG candidate compared to the NGC 4632 model at a resolution of 10 BA, an inclination of 75°, and a ring orientation angle of 0°. W1309 likely possesses a polar disk, so the ring features in the model PRG panels were used as a reference for extrapolation. Recall that the primary difference between a polar ring and a polar disk is the space between the misaligned component and the main galaxy body. By extending the patterns observed in the modelled ring towards the galaxy body, the presentation of a polar disk at this orientation can be estimated. The moment zero map for this galaxy depicts a sparse gaseous component, perhaps due to the mask that was applied, which makes the moment one maps a far more compelling

Figure 5.6: Optical image of NGC 4899 (W1300) from DECaLS (Dey et al., 2019).

comparison.

Since W1309 is relatively consistent with modelled PRG signatures and orientations, it was able to be included as a PRG candidate. Figure 5.9 shows the Legacy Survey DR10 image of W1309, which cross-matches to IRAS 13070-

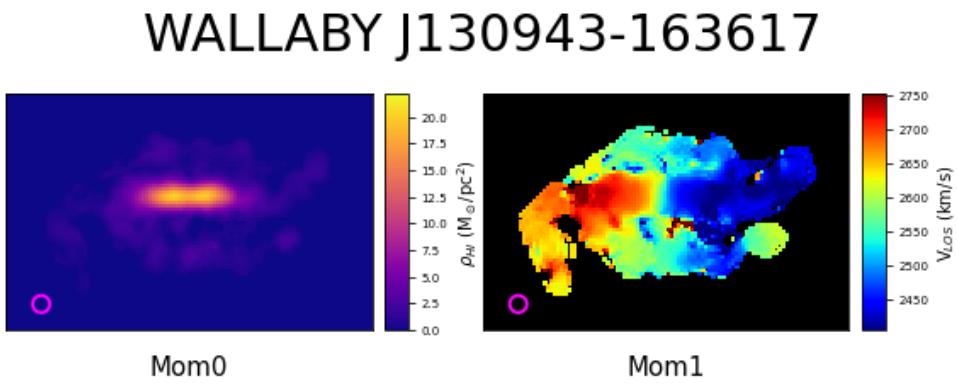

Figure 5.7: WALLABY galaxy J130943-163617, a PRG candidate from PDR2, detected at a resolution of ∼11 BA. The moment zero plot (left) shows faint evidence of a potential disk structure surrounding the main component, while the moment one map (right) indicates that the dispersed gas may be rotating in a different plane from the galaxy body.

1620. While it is difficult to discern any details from this saturated image, the general shape of the galaxy body is consistent with the disk galaxy that was expected from the HI data.

Poorly resolved galaxies were also identified that show some evidence of having a polar component, but the reliability of the detections was insufficient for them to be considered PRG candidates for the purposes of estimating incidence. The moment zero and moment one plots for all of these tentative PRG candidates are included in Appendix B, with one discussed below for illustrative purposes.

WALLABY J131649-133623 was observed in DR3 of the NGC 5044 group at a resolution of approximately 3.7 BA. Individual pixels can be seen in the moment zero and moment one maps, Figure 5.10, which demonstrates the low resolution before even knowing the beams across value. There is an oblong central component that trends towards yellow on the side canted slightly towards the redshifting component, depicted by a red circle on the Eastern side of the galaxy. The blueshifting component on the Western side of the galaxy neighbours the portion of the central component that shifts towards cyan. The middle element averages the green of the object's systemic velocity, which could indicate a kinematically misaligned component. Despite the hints of PRG signatures in the moment one map, this galaxy was not considered a candidate because at this low resolution the abnormalities could stem from instrumental effects or noise. This will be demonstrated further

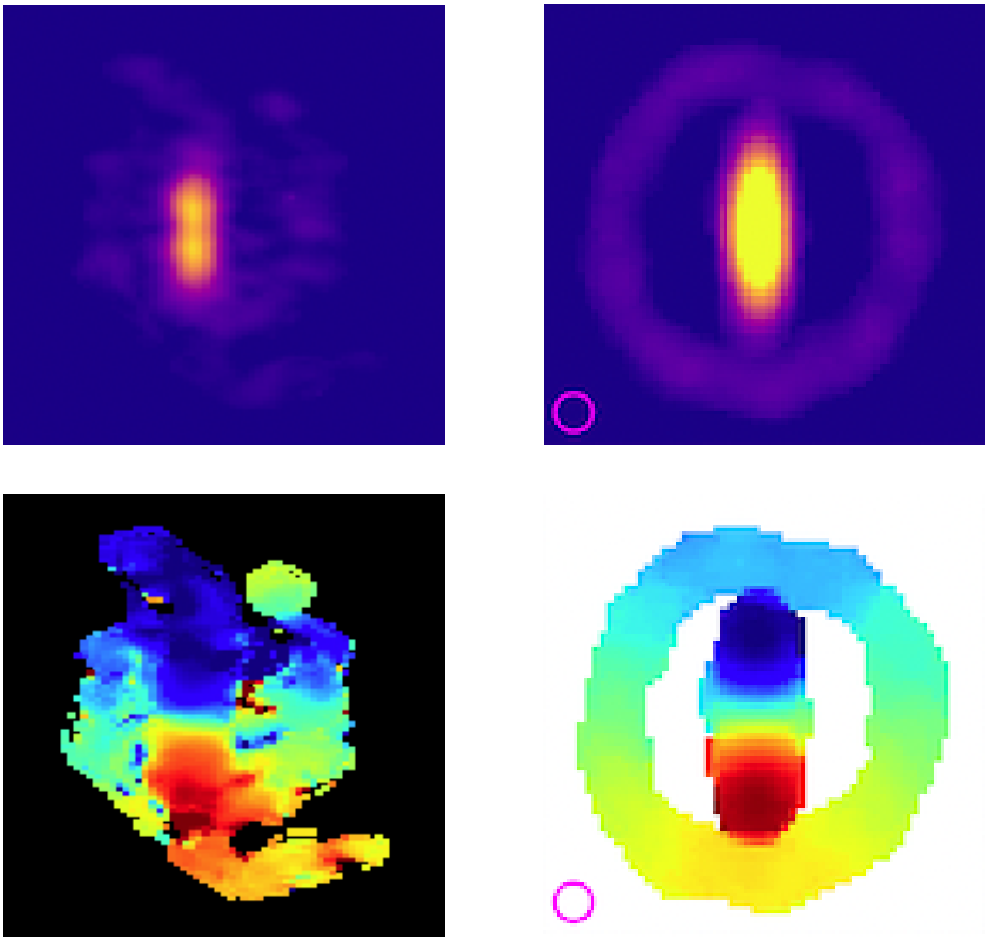

Figure 5.8: Comparison of moment maps for W1309 (left) with the PA rotated 90°, and a panel from the NGC 4632 model's (right) moment panel plots (Appendix A) at resolutions of 10 BA with i = 75° and $\beta = 0°$. Both moment zero maps (top) depict a bright central component with a fainter widespread ring/disk of diffuse gas. Both moment one maps (bottom) demonstrate a nearly neutral polar component that trends towards yellow on one side and cyan on the other, as well as strong blue and red sections found relatively close together in the centre of the maps.

with 3D cube projections in Section 5.1.1. The moment zero map has no discernible abnormalities, only a brighter central component that is typical

Figure 5.9: IRAS 13070-1620 (W1309) in the optical from DECaLS (Dey et al., 2019).

for most detections at this resolution. It was compared to the NGC 6156 model at 3 BA in Figure 5.11.

These plots look ostensibly similar, down to the ring of yellow around the inner edge of the red circles in both moment one maps, but with the low resolution of the data and the lack of a normal galaxy panel for comparison it is not feasible to include candidates like this into the incidence calculations. The incidence calculations have an uncertainty of plus or minus one galaxy, to account for the potential PRGs included in Appendix B that were detected at low angular resolutions and could not be supported by 3D rendering.

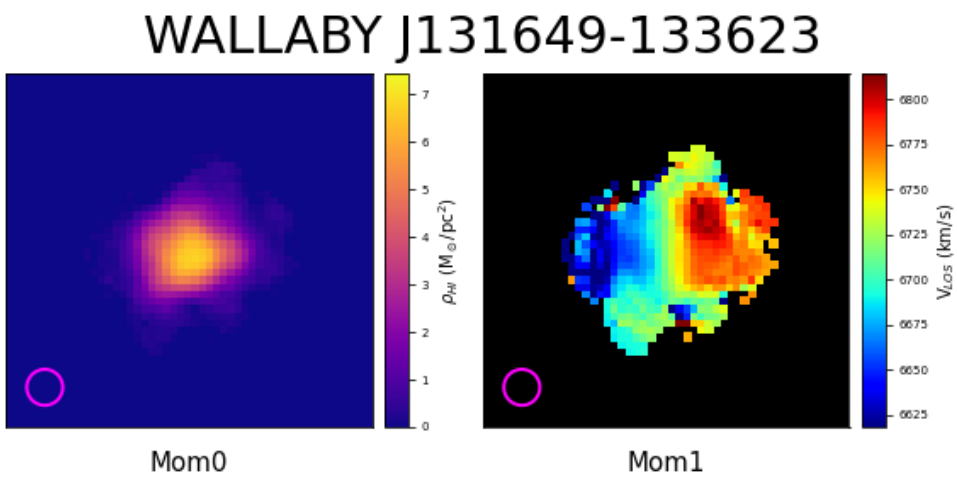

Figure 5.10: WALLABY galaxy J131649-133623, detected at a resolution of ∼3.5 BA, which exhibits some PRG signatures. The moment zero map (left) shows no evidence of a polar component, but the moment one map (right) depicts an elongated central portion, travelling predominantly at the object's systemic velocity, that could indicate a kinematically misaligned gaseous component.

PRG Candidate	Angular Resolution
NGC 4808	17 BA
NGC 4899	10 BA
W1309	11 BA

Table 5.1: PRG candidates from PDR2 of the WALLABY pilot survey and the angular resolutions of their detections.

5.1.1 3D Visualization

In order to further narrow the PRG candidates from PDR2, a three-dimensional FITS file viewer called Slicer (Fedorov et al., 2012) was used. Slicer's 3D rendering and rotation capability allows the form of both the main galaxy and polar components to be seen much more clearly amid the noise. In Figures 5.12 to 5.16, individual frames were selected at orientations that best exemplified the polar component for each of the PRG candidates identified above. A Slicer image of the tentative PRG WALLABY J131649-133623, among the objects given in Appendix B but not considered in the incidence calculation of Section 5.2, was also included in order to demonstrate why the features seen

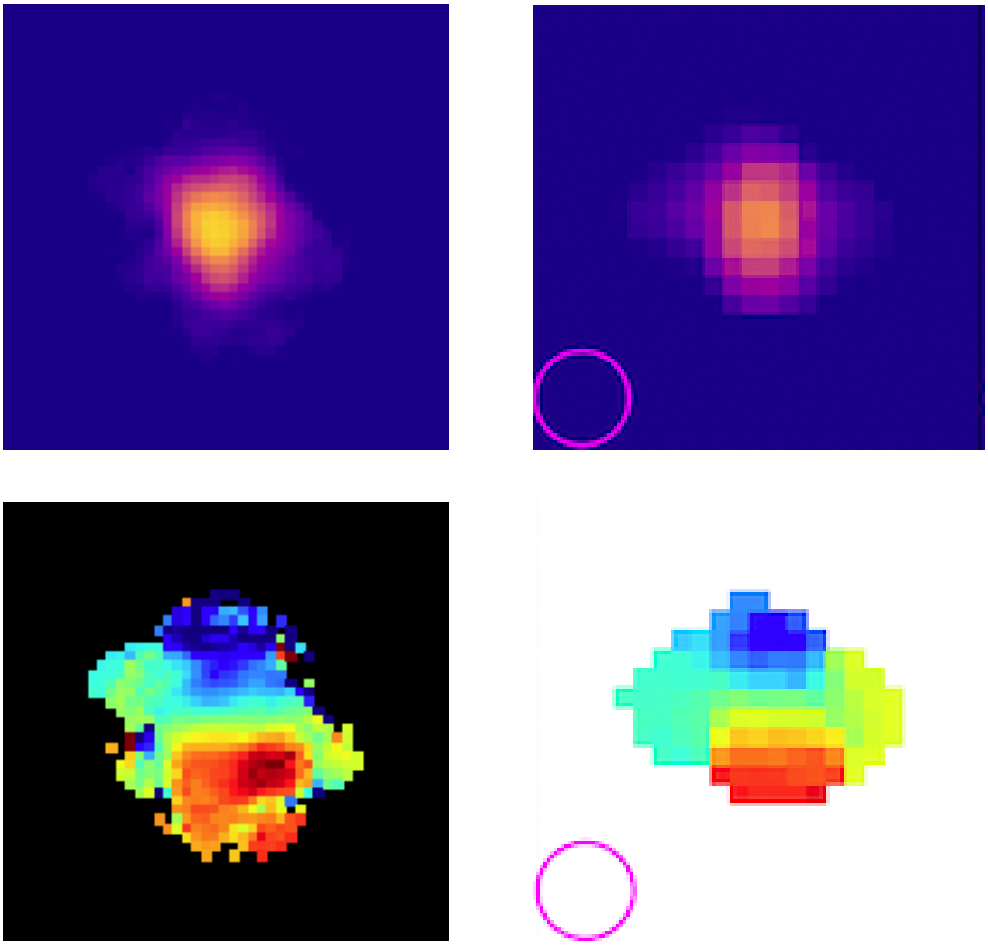

Figure 5.11: Comparison of moment maps for WALLABY J131649-133623 (left), with the PA rotated 90°, and panels from the NGC 6156 model's panel plot (Appendix A) at a resolution of 3 BA (right) with i = 60° and β = 90°. Neither moment zero map (top) exemplifies sufficient evidence to be identified as a PRG, although they are similar in that the central component is a circle with slightly elongated bits of gas. Both moment one maps (bottom) depict a red and blue dot on either side of an elongated central component with a neutral green velocity colour. The elongated component on both galaxies trends towards yellow on one side and cyan on the other.

in the moment plots cannot be entirely relied upon at lower resolutions.

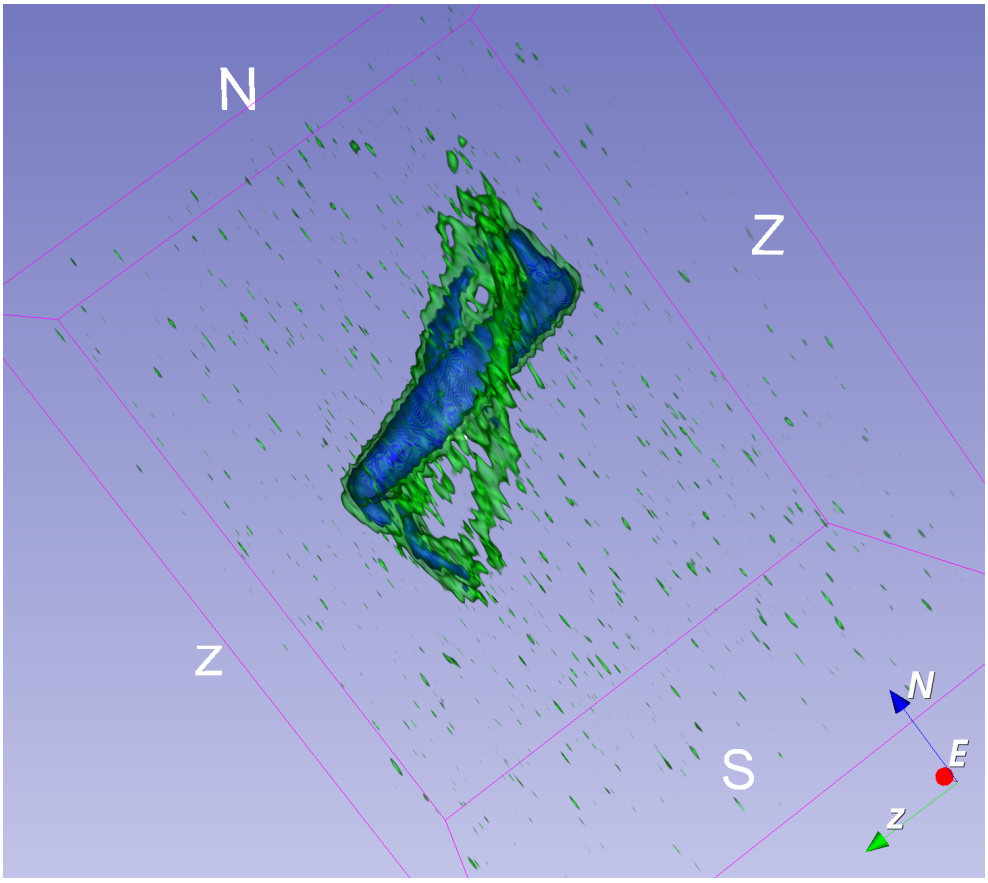

Figure 5.12: NGC 4808, for which moment maps are shown in Figure 5.1, viewed in Slicer at a noise threshold of approximately 1.85 mJy/beam. The elongated blue component is the central galaxy, and the green circle surrounding it is the ring component. The denser portions of the ring are seen in blue.

Figure 5.12 shows a 3D view of W1255. The rendering threshold value for this image was set to ∼1.85 mJy/beam. This is a relatively high threshold compared to the other cubes that were examined, but acceptable because of the clarity of the ring component. The green gas forms the ring structure, and is sufficiently well-defined as to even contain some blue, brighter emission. It is clear from this image that the galaxy contains some form of tilted ring structure. The y-axis in this 3D view reveals a blue hook-like structure that connects the main galaxy body with the polar component. This suggests that perhaps the tilted ring is an extreme warp rather than a wholly separate polar

ring.

Figure 5.13 shows W1300 in 3D. While it is not as clear as NGC 4808's ring in Figure 5.12, there is still clear evidence of a polar component. There are a few especially dense clumps in the ring that reveal themselves in blue, but the misaligned component is primarily represented through defined green clumps forming a nearly complete circle. Even through the noise, it is clear that there exists a secondary component that is offset from the main galaxy body, reinforcing this galaxy as a PRG candidate.

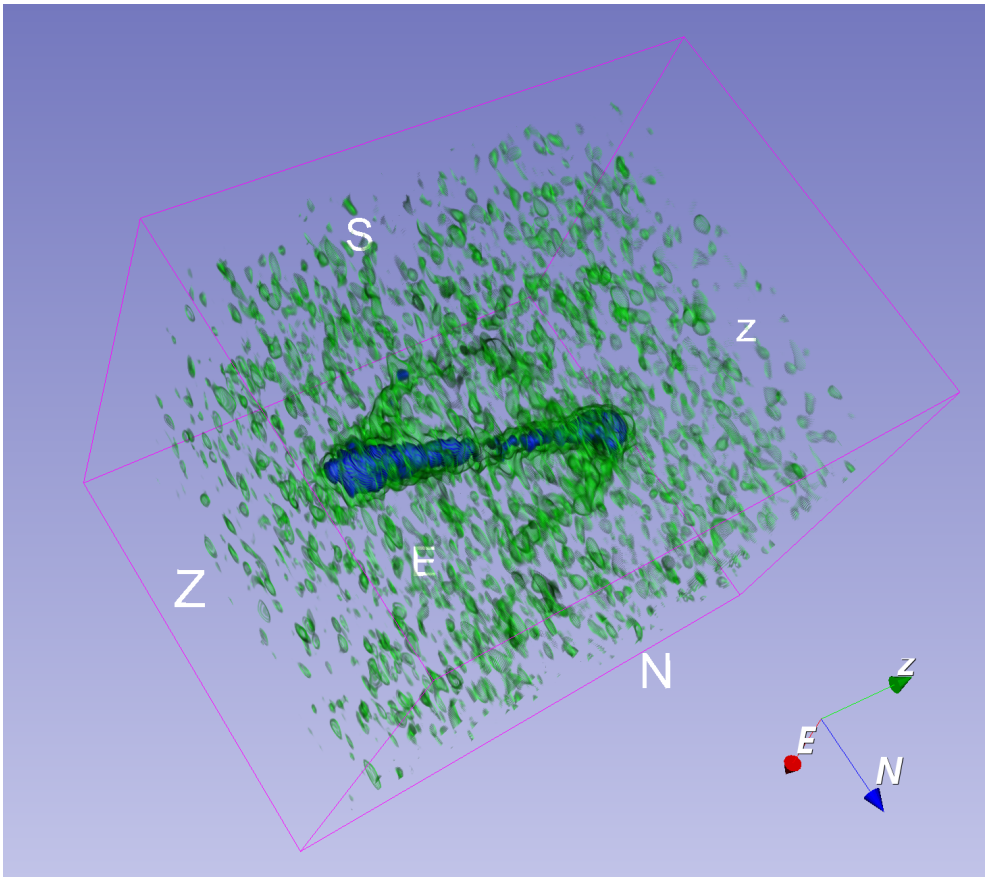

Figure 5.13: NGC 4899, for which moment maps are shown in Figure 5.4, viewed in Slicer at a threshold of approximately 1.31 mJy/beam. The elongated blue component is the central galaxy, and the tilted ring can be discerned among the noise as a partially complete dense green circle. The more translucent green specks within the image represent noise.

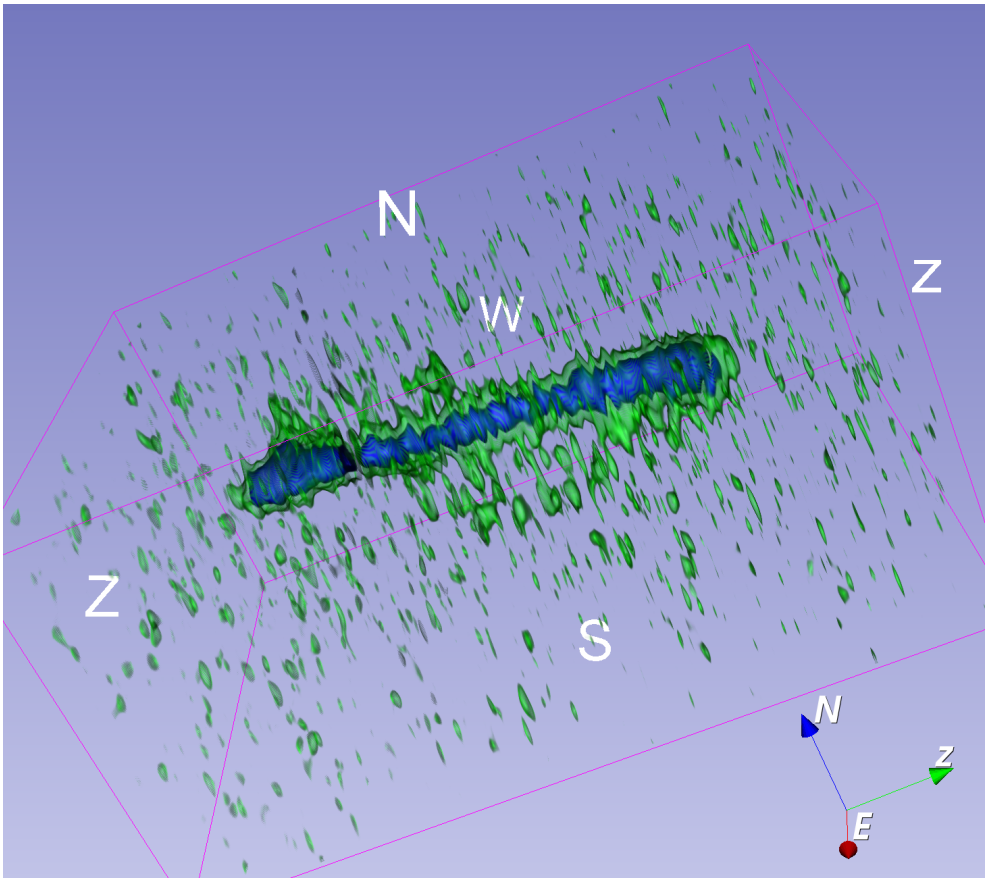

Figure 5.14: W1309, for which moment maps are shown in Figure 5.7, viewed in Slicer at a threshold of approximately 1.54 mJy/beam. The elongated blue component is the central galaxy, and the ring can be partially seen through a pattern of thicker and brighter green flecks. A second 3D orientation for this detection is shown in Figure 5.15.

Figures 5.14 and 5.15 show different 3D projections of W1309, the least convincing PRG candidate in PDR2. The two figures show this galaxy at different orientations, because the ring structure is more difficult to see without the benefit of live cube rotation. Figure 5.14 shows a side view where portions of the ring component can be seen. They appear as green clumps that are slightly brighter than the noise surrounding them. Note that there is a slice of empty space visible through the model on the $-z$ axis, which cuts through the blue main body in Figure 5.14 and is caused by flagged pixels in the

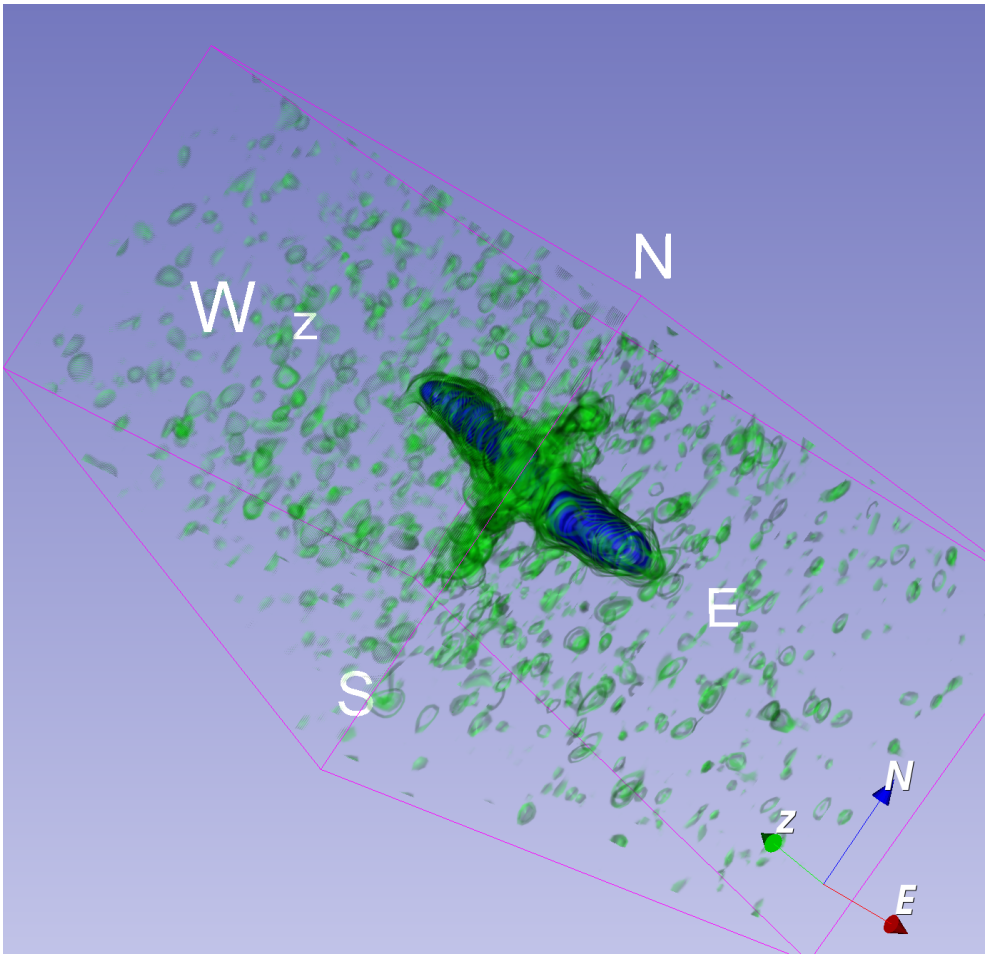

Figure 5.15: W1309 viewed in Slicer at a second orientation with the same threshold value as in Figure 5.14. The main galaxy remains visible as the elongated blue component, but the ring is evidenced more clearly when viewed edge-on. The clumps of green that intersect the blue component in a dense line represents the ring, and the more translucent green flecks represent the noise.

PDR2 data cube. While Figure 5.14 may not be convincing on its own, it is supported greatly by the second projection of the same dataset in Figure 5.15.

At this projection, the ring in W1309 is viewed edge-on. There is clearly an amalgamation of green gaseous elements that are located in a plane offset from the main galaxy component. At the relatively high resolution of this

observation, this is unlikely to be coincidental and constituted the deciding factor in including this detection in the list of PRG candidates in PDR2.

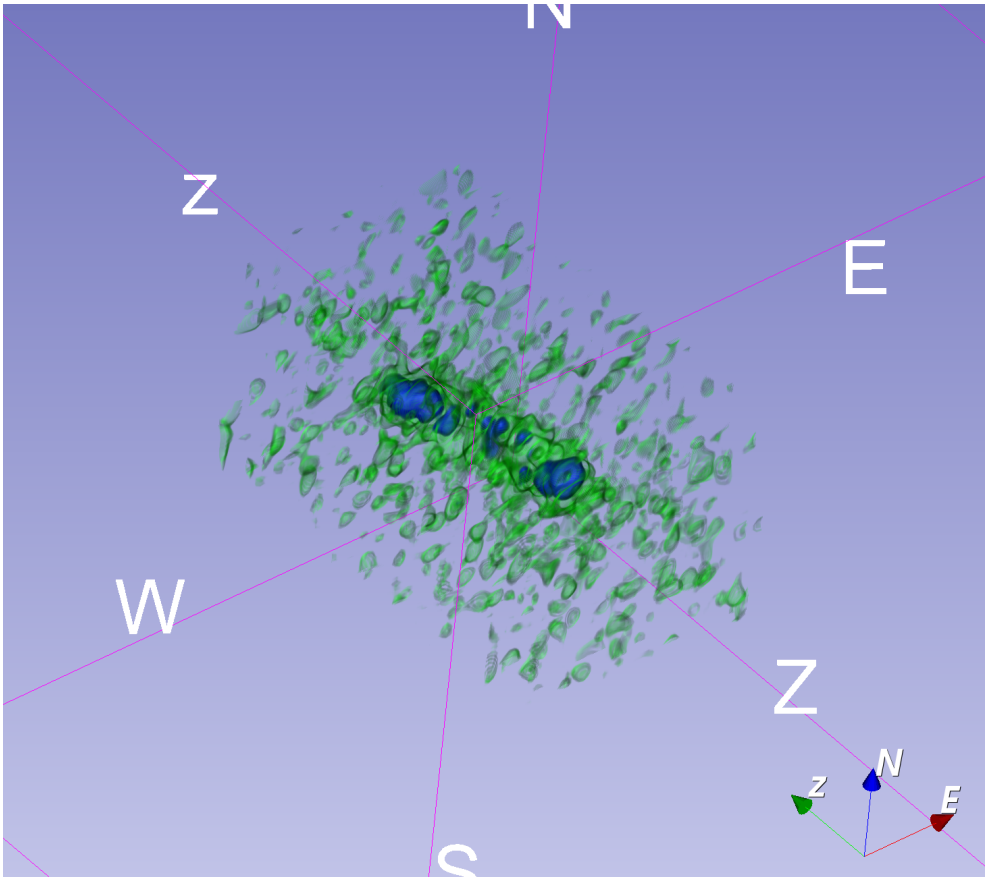

Figure 5.16: WALLABY J131649-133623, for which moment maps are shown in Figure Appendix B, viewed in Slicer at a threshold of approximately 0.96 mJy/beam. The patchy blue component represents the main galaxy body, and if a polar component is present it cannot be discerned amongst the green clumps of noise at this resolution.

For completeness, Figure 5.16 shows a 3D view of WALLABY J131649-133623. The Slicer views of the other objects in Appendix B were a large contributor to their omission from the list of PRG candidates. In this image, even with the very low noise threshold value allowing all faint emission to be rendered, there is no discernible ring structure. Thus while the hints of a polar structure in its moment maps (Figure 5.10) may indicate a tilted ring of

gas in this galaxy, at this resolution there is marginal evidence for one in 3D. The signatures seen in the moment maps may therefore be caused by masking artifacts due to the local noise fluctuations.

5.2 PDR2 Incidence Calculations

The detectability fraction that was determined while studying PDR1 (Section 4.4) was used again in the PDR2 study since it was based on observation conditions unspecific to any particular PRG. These fractions were determined by examining each panel in the moment panel plots (Section 4.1) at five different resolutions. The fraction of identifiable PRG orientations was recorded for both galaxy models, as was discussed in Section 4.4.

Two PRG candidates were identified in the first phase of the WALLABY study, and three were identified in the second phase. PDR1 only contained 592 objects, compared to PDR2's 2743 objects. Figure 5.17 demonstrates how PDR1 detected far fewer objects at lower resolutions than PDR2, but how the objects detected have relatively higher angular resolutions. At resolutions where PRGs are consistently identifiable, PDR1 and PDR2 yielded similar sample sizes. This is important when considering the incidence of PRGs weighted by the detectability fraction at the observation's resolution (see Figure 4.17). At 3 BA, the detectability fraction is zero. That means that for the purposes of the incidence calculations, none of the galaxies in that bin were counted for PDR1 or PDR2. The low weight of low resolution detections puts PDR2 nearly equal to PDR1 in terms of constraining the incidence of PRGs from WALLABY's pilot survey phase.

The equation used to calculate the incidence of PRGs in PDR1 (Equation 4.21) was used again to calculate their incidence in PDR2 using the data in Table 5.2:

$$f_i = \frac{3}{198.224} = 0.0151 \ , \tag{5.1}$$

which translates to an incidence of $\sim$1.5%, essentially identical to the incidence of PRGs calculated using the PDR1 data (see Section 4.4.1).

Note that the detectability fractions in Table 5.2 are the same as those in Table 4.1, as a detectability analysis using PRG models of the PDR2 candidates was not within the scope of this thesis. Since the two PRG models from PDR1 varied greatly in their individual detectability fractions but yielded very similar results when the moment zero and moment one maps were viewed together, it is unlikely that additional modelling would cause the average detectability fractions to differ significantly. Future studies could

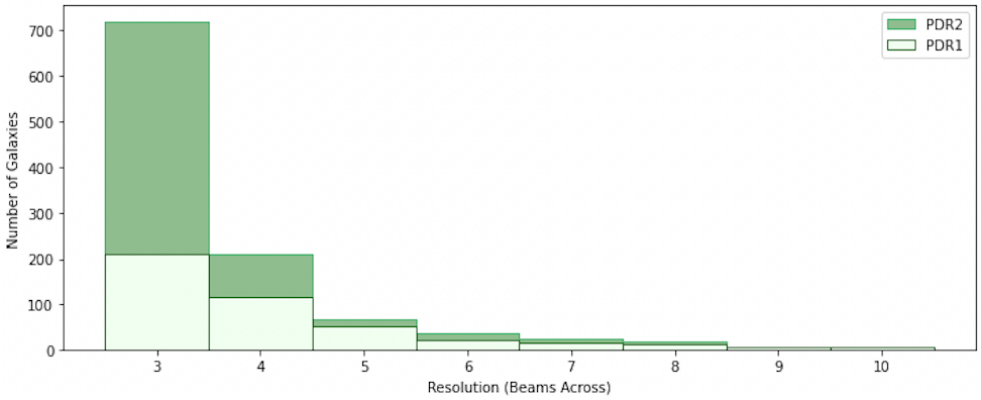

Figure 5.17: Comparison of detections and resolutions between PDR1 (light green) and PDR2 (dark green). PDR2 had more detections overall, but they were heavily weighted towards lower resolutions where PRG signatures are unreliable.

refine the results generated in this analysis by creating moment panel plots and detectability fractions for the PDR2 candidates. This would reinforce the average detectability fraction values and create a more reliable incidence estimate for gas-rich PRGs.

In order to account for uncertainties in the identification of PRGs, $N_{detected}$ (the number of PRGs identified in the data set) was varied by one galaxy in both directions. This created an incidence range of $\sim$1% to 2% for both PDR1 and PDR2 when rounded to the nearest percent. These ranges are consistently larger than literature values for gas-gas polar kinematic misalignments, and are relatively consistent with each other. The PDR2 results support the conclusions drawn from the PDR1 data, now with a larger sample.

Resolution (BA)	Detectability Fraction	Number of Detections	Product
3	0/49	719	0
4	18/49	210	76
5	30/49	68	42
6	38/49	36	28
7	43/49	26	23
8	46/49	20	19
9	47/49	6	6
10	48/49	6	6
		Sum	200

Table 5.2: Incidence fraction calculations for PDR2. The detectability fraction (see Figure 4.17 and Table 4.1) was multiplied by the number of detections in order to get the product, which was then summed in order to get the denominator for Equation 4.21. The product column is rounded to the nearest integer. Some of the detectability fractions may have had a non-whole numerator due to the averaging of NGC 4632 and NGC 6156 data, and the interpolation of intermediate data points. In this table, the numerators of the detectability fraction are also rounded to the nearest integer.

5.3 Summary

This chapter applied the analysis conducted on the PDR1 data to the detections from WALLABY PDR2. Section 5.1 introduced the PRG candidates that were identified from PDR2 data and compared them to panels from the moment map panel plots generated using the NGC 4632 and NGC 6156 models (see Section 4.1). Section 5.2 calculated the incidence of gas-rich PRGs in WALLABY PDR2 to be $\sim$1.5%, essentially identical to that estimated from PDR1 data but using a significantly larger sample.

6 Discussion & Conclusion

By using the detectability fraction to calculate the genuine incidence of gas-rich PRGs, the suspected number of these objects increased dramatically. Only five PRG candidates were discovered in a combined survey of 3335 objects. That would imply an incidence of ∼0.15% for gas-gas polar misalignments if resolution effects were ignored, which is a lot closer to the accepted literature value of ∼0.1% (Reshetnikov et al., 2011). It is clear that the orientation and resolution of radio astronomy detections is more than capable of obscuring the necessary evidence to identify PRGs, which is why the incidence of PRGs may have been consistently underestimated. Future studies may extend this analysis to other unique objects found throughout the Universe in order to determine how the observation conditions affect their predicted incidence. There may be a variety of phenomena that occur more often than previously estimated, due to the difficulties associated with identification, the effects of resolution, and the orientation of the object.

The incidence analysis conducted for PDR1 of the WALLABY survey followed the exact same procedure as the PDR2 analysis, the only difference between the two being the data sets. There were more galaxies in PDR2, but most of those galaxies were observed at lower resolutions. There was only one additional PRG candidate in PDR2 than was found in PDR1, but with the weighted summation of galaxies based on their resolution, this extra galaxy was sufficient to maintain balance. Having an incidence estimate that was essentially identical in both data sets is encouraging. Even if the least convincing candidate is not included in the calculations, an incidence of ∼1% is still much greater than earlier estimates.

Discovering the true incidence of gas-gas polar kinematic misalignments is important to extragalactic astronomy (Whitmore, 1984) and the study of dark matter (Khoperskov et al., 2014b; Whitmore et al., 1990; Moiseev et al., 2015). There have been many incidence estimates of gas-star PRGs that were much greater than the ∼0.1% (Reshetnikov et al., 2011) allotted to gaseous components and younger galaxies. While this is reasonable, given the base

statistics of older galaxies having had more opportunities to interact with other galaxies or accrete gas from their surroundings, it has caused gas-gas PRGs to be overlooked. Many formation theories were based off of elliptical galaxies with an exhausted main body and a polar component that was rich with gas and star forming regions (Moiseev, 2014; Sparke and Cox, 2000; Wakamatsu, 1993). This is not the case for all polar misalignments, and the results of this thesis support the presence of a competitive number of gas-rich PRGs in the local Universe. PRGs with ample amounts of HI gas in both the main galaxy body and the polar component imply a polar ring formation at a relatively young age, and are perhaps not as rare as astronomers believe.

This analysis contained some limitations that must be acknowledged when referencing the true incidence of gas-rich PRGs in the local Universe. First, the models used to create the moment panel plots were very idealized with respect to their shape and inclination. The ring was assumed to be both perfectly circular and perfectly polar, inclined at 90° exactly for consistency and simplicity. PRGs can exist with a wide range of inclinations, which may look quite different in the morphology and kinematic diagrams. Transitioning rings were also not accounted for during the analysis, as their moment maps may closely resemble that of the PRGs at various orientations. Further studies could investigate low inclination kinematic misalignments at various observation conditions in order to test the results gathered in this study or to research how other phenomena present in moment maps. The rings, polar or otherwise, are also not likely to be a perfect circle, and could extend laterally in thicker disk-like components that would alter the way they are observed. Future analyses could model polar disk galaxies with thicker polar components and create similar moment panel plots for them. This could also be undertaken for misshapen rings and polar components inclined slightly offset from perfectly polar; somewhere between 70° and 110° from the major axis of the galaxy body.

The detectability fraction at each resolution was determined through visual examination from only three scientists that were well-versed in the area. In order to reinforce the specific detectability fraction of PRGs, it may be useful to circulate the panels to subject matter experts on a wider scale. This would provide a more reliable average detectability fraction among extragalactic radio astronomers, however it may also skew the fraction when astronomers who are unfamiliar with PRGs are considered. Applying fresh perspectives to the various observation conditions would provide a more realistic detectability fraction outside of the PRG community. The panel plots themselves contain a detectability paradox: since the observer knows that the object being modelled is a PRG, they will be more likely to discern identifiable features. Perhaps

when they are circulated among astrophysicists, the panels could be presented as individual galaxies. This way, observers would not know that every panel is in fact a PRG and it would simulate more closely the process of detecting polar components among real galaxy observations.

Future studies could alternatively focus on automated methods of identifying PRGs. Computing programs running kinematic analyses on detected objects may fail consistently when a PRG is encountered, or the polar component may be identified as an asymmetrical feature of the gas dispersion. Anomalous results from galaxy identification programs may be a faster method of narrowing detections down to only the most likely PRG candidates. Furthermore, the detectability analysis in this thesis generated the first set of predictive plots for the presentation of PRGs in HI data at different orientations. These plots could be used as the basis for future machine learning projects surrounding gas-rich PRG identification.

The noise in data cubes from widefield surveys such as WALLABY can be included in the SoFiA mask inadvertently, which can cause there to be spurious PRG markers. It could also erase PRG signatures if they are too faint or if there happens to be too much noise in that region. The interference experienced by radio telescopes adds another layer of uncertainty into this anaylsis that is difficult to account for. Future analyses could use three-dimensional modelling programs, like Slicer, to view the data cubes and understand where the observations are coming from. This was done for the WALLABY PDR2 PRG candidates, and was integral to narrowing down which candidates were viable and which candidates were too poorly resolved to be included in the incidence estimate.

It should also be acknowledged that this incidence calculation relied on PRG *candidates* from both PDR1 and PDR2 of the WALLABY survey. These galaxies have not yet been confirmed as PRGs through kinematic modelling (Deg et al., 2022), only targeted as strong contenders that should be researched further. Some of these candidates have moment maps that are very convincing on their own, while others have moment maps with indicators that are not quite as unquestionable. This is why an uncertainty of one galaxy was included in the incidence calculations, in order to account for the potential PRGs still being in their candidacy phase of discovery. Even if the incidence is at the lower end of the estimated scale, $\sim$1% is still significantly greater than the literature value of 0.1% estimated by Reshetnikov et al. (2011) and worth noting for future studies.

The PRG incidence being approximately ten times greater than previous estimates indicates that galaxies are experiencing acquisition events more frequently than was previously believed. This is an important detail in the

study of galactic interactions as well as the formation mechanisms of PRGs themselves. It will also be useful in future radio astronomy surveys that may contain galaxies with polar features in their morphology and kinematics diagrams. The moment panel plots can be used as a reference in future scientific endeavours when a PRG candidate has been discovered, and the updated incidence of these objects can be used to support future candidates as well. Cosmological simulations (Macciò et al., 2006; Brook et al., 2008) can also be refined with the knowledge that polar gas acquisition events occur approximately ten times more often in gas-rich galaxies than previously believed.

To summarize this thesis, three PRG candidates were identified in WALLABY PDR2. NGC 4808 is the most promising candidate, presenting with a clear HI ring surrounding its main galaxy body when examined in its moment zero map. Its moment one map does not offer many details regarding a polar structure, but is consistent with the moment maps of model PRGs at low ring orientation angles. NGC 4899 is the next most convincing candidate from the morphology and kinematics analyses that were conducted in this thesis. It possesses an HI ring-like structure that is visible in the moment zero map, with only a few gaps on the left side of the ring. The moment one map depicts a ring shape as well, where the gas particles are moving at the systemic velocity. This indicates that the plane of rotation for the misaligned section of the galaxy is different than that of the main galaxy body. The left side of the ring either does not exist, was erroneously removed by the mask, or was unable to be resolved even at 10 beams across. W1309 is the third and final PRG candidate from PDR2. It is the least convincing due to the patchy observations of the gaseous disk as well as the anomalous shape seen in the moment one map. There are two arms reaching out of the main galaxy body which do not necessarily negate the existence of a polar component, but they do suggest the possibility of some other phenomenon.

Through the examination and evaluation of $\sim$980 individual moment panels, a resolution dependent detectability fraction for PRGs was able to estimated. The panels consisted of moment zero and moment one maps for an NGC 4632 model galaxy and an NGC 6156 model galaxy at 49 different orientations. The model galaxies' inclinations were observed at seven different angles, and their ring orientation angles were altered to seven different positions. The dimensions of each ring within the tilted ring model were adjusted in order to simulate observation at five different angular resolutions. The detectability of each galaxy was expressed as a fraction for each of the resolution settings, and plotted in order to observe the trend. The trend that was found across the tested resolutions of three, four, six, eight, and ten beams across was extrapolated such that detectability fractions could be used for the in-

termediate resolutions of five, seven, and nine beams across. These values were used in conjunction with over 3000 detections from the pilot phase of the WALLABY survey in order to determine the amount of PRGs that could have been identified in each resolution range if they existed. The number of PRG candidates in PDR1 and PDR2 were used with this weighted detectability value such that the total gas-rich PRG incidence in each phase could be estimated.

The difference between the PDR1 and PDR2 results was effectively negligible, as both data sets estimated a gas-rich PRG incidence of $\sim$1.5% and an incidence range including uncertainties of $\sim$1%-2%. The lower limit alone indicates that PRGs are approximately ten times more abundant than the canonical literature value of $\sim$0.1% (Reshetnikov et al., 2011). These results could be further supported by future studies using WALLABY data, or detections from another untargeted radio survey. This analysis manipulated the tilted ring models of two previously identified PRG candidates from PDR1, evaluated $\sim$980 mock observation moment panels, and identified three PRG candidates in WALLABY PDR2. This thesis estimates the weighted incidence of gas-rich polar displacements in WALLABY pilot fields to be $\sim$1.5%, providing new insight into the nature of these unique systems and the challenges associated with their study.

Bibliography

Hiroaki Aihara, Robert Armstrong, Steven Bickerton, James Bosch, Jean Coupon, Hisanori Furusawa, Yusuke Hayashi, Hiroyuki Ikeda, Yukiko Kamata, Hiroshi Karoji, Satoshi Kawanomoto, Michitaro Koike, Yutaka Komiyama, Dustin Lang, Robert H. Lupton, Sogo Mineo, Hironao Miyatake, Satoshi Miyazaki, Tomoki Morokuma, Yoshiyuki Obuchi, Yukie Oishi, Yuki Okura, Paul A. Price, Tadafumi Takata, Manobu M. Tanaka, Masayuki Tanaka, Yoko Tanaka, Tomohisa Uchida, Fumihiro Uraguchi, Yousuke Utsumi, Shiang-Yu Wang, Yoshihiko Yamada, Hitomi Yamanoi, Naoki Yasuda, Nobuo Arimoto, Masashi Chiba, Francois Finet, Hiroki Fujimori, Seiji Fujimoto, Junko Furusawa, Tomotsugu Goto, Andy Goulding, James E. Gunn, Yuichi Harikane, Takashi Hattori, Masao Hayashi, Krzysztof G. Hełminiak, Ryo Higuchi, Chiaki Hikage, Paul T. P. Ho, Bau-Ching Hsieh, Kuiyun Huang, Song Huang, Masatoshi Imanishi, Ikuru Iwata, Anton T. Jaelani, Hung-Yu Jian, Nobunari Kashikawa, Nobuhiko Katayama, Takashi Kojima, Akira Konno, Shintaro Koshida, Haruka Kusakabe, Alexie Leauthaud, Chien-Hsiu Lee, Lihwai Lin, Yen-Ting Lin, Rachel Mandelbaum, Yoshiki Matsuoka, Elinor Medezinski, Shoken Miyama, Rieko Momose, Anupreeta More, Surhud More, Shiro Mukae, Ryoma Murata, Hitoshi Murayama, Tohru Nagao, Fumiaki Nakata, Mana Niida, Hiroko Niikura, Atsushi J. Nishizawa, Masamune Oguri, Nobuhiro Okabe, Yoshiaki Ono, Masato Onodera, Masafusa Onoue, Masami Ouchi, Tae-Soo Pyo, Takatoshi Shibuya, Kazuhiro Shimasaku, Melanie Simet, Joshua Speagle, David N. Spergel, Michael A. Strauss, Yuma Sugahara, Naoshi Sugiyama, Yasushi Suto, Nao Suzuki, Philip J. Tait, Masahiro Takada, Tsuyoshi Terai, Yoshiki Toba, Edwin L. Turner, Hisakazu Uchiyama, Keiichi Umetsu, Yuji Urata, Tomonori Usuda, Sherry Yeh, and Suraphong Yuma. First data release of the Hyper Suprime-Cam Subaru Strategic Program. , 70:S8, January 2018. doi: 10.1093/pasj/psx081.

Jean Ballet. X-ray Synchrotron Emission from Supernova Remnants. *Advances in Space Research*, 37(10), January 2006. ISSN 02731177. doi: 10.1016/j.asr.2005.03.047. URL http://arxiv.org/abs/astro-ph/0503309.

Kenji Bekki. Formation of Polar Ring S0 Galaxies in Dissipative Galaxy Mergers. *The Astrophysical Journal*, 490(1):L37–L40, November 1997. ISSN 0004637X. doi: 10.1086/311008. URL https://iopscience.iop.org/article/10.1086/311008.

Kenji Bekki. Unequal-Mass Galaxy Mergers and the Creation of Cluster S0 Galaxies. *The Astrophysical Journal*, 502(2):L133–L137, August 1998. ISSN 0004637X. doi: 10.1086/311508. URL https://iopscience.iop.org/article/10.1086/311508.

Michael R. Blanton, Julianne Dalcanton, Daniel Eisenstein, Jon Loveday, Michael A. Strauss, Mark SubbaRao, David H. Weinberg, John E. Anderson, Jr., James Annis, Neta A. Bahcall, Mariangela Bernardi, J. Brinkmann, Robert J. Brunner, Scott Burles, Larry Carey, Francisco J. Castander, Andrew J. Connolly, István Csabai, Mamoru Doi, Douglas Finkbeiner, Scott Friedman, Joshua A. Frieman, Masataka Fukugita, James E. Gunn, G. S. Hennessy, Robert B. Hindsley, David W. Hogg, Takashi Ichikawa, Željko Ivezić, Stephen Kent, G. R. Knapp, D. Q. Lamb, R. French Leger, Daniel C. Long, Robert H. Lupton, Timothy A. McKay, Avery Meiksin, Aronne Merelli, Jeffrey A. Munn, Vijay Narayanan, Matt Newcomb, R. C. Nichol, Sadanori Okamura, Russell Owen, Jeffrey R. Pier, Adrian Pope, Marc Postman, Thomas Quinn, Constance M. Rockosi, David J. Schlegel, Donald P. Schneider, Kazuhiro Shimasaku, Walter A. Siegmund, Stephen Smee, Yehuda Snir, Chris Stoughton, Christopher Stubbs, Alexander S. Szalay, Gyula P. Szokoly, Aniruddha R. Thakar, Christy Tremonti, Douglas L. Tucker, Alan Uomoto, Dan Vanden Berk, Michael S. Vogeley, Patrick Waddell, Brian Yanny, Naoki Yasuda, and Donald G. York. The Luminosity Function of Galaxies in SDSS Commissioning Data. *The Astronomical Journal*, 121(5):2358–2380, May 2001. ISSN 00046256. doi: 10.1086/320405. URL https://iopscience.iop.org/article/10.1086/320405.

F. Bournaud and F. Combes. Formation of Polar Ring Galaxies. *Astronomy & Astrophysics*, 401(3):817–833, April 2003. ISSN 0004-6361, 1432-0746. doi: 10.1051/0004-6361:20030150. URL http://www.aanda.org/10.1051/0004-6361:20030150.

F. Bournaud, C. J. Jog, and F. Combes. Galaxy Mergers With Various Mass Ratios: Properties of remnants. *Astronomy & Astrophysics*, 437(1):69–85,

July 2005. ISSN 0004-6361, 1432-0746. doi: 10.1051/0004-6361:20042036. URL http://www.aanda.org/10.1051/0004-6361:20042036.

Chris B. Brook, Fabio Governato, Thomas Quinn, James Wadsley, Alyson M. Brooks, Beth Willman, Adrienne Stilp, and Patrik Jonsson. The Formation of Polar Disk Galaxies. *The Astrophysical Journal*, 689(2):678–686, December 2008. ISSN 0004-637X, 1538-4357. doi: 10.1086/591489. URL https://iopscience.iop.org/article/10.1086/591489.

Xiao Cao, Yan-Mei Chen, Yong Shi, Min Bao, Alexei Moiseev, Dmitry Bizyaev, Song-Lin Li, José G. Fernández-Trincado, Rogemar A. Riffel, Rogério Riffel, and Richard R. Lane. Multiple gas acquisition events in galaxies with dual misaligned gas disks. *Nature Astronomy*, 6(12), September 2022. ISSN 2397-3366. doi: 10.1038/s41550-022-01788-8. URL http://arxiv.org/abs/2209.15417.

F. Combes. Polar Ring Galaxies and Warps. *EAS Publications Series*, 20: 97–104, 2006. ISSN 1633-4760, 1638-1963. doi: 10.1051/eas:2006054. URL http://www.eas-journal.org/10.1051/eas:2006054.

N Deg and K Spekkens. MCG Guide. *Monthly Notices of the Royal Astronomical Society (Preprint)*, October 2022.

N. Deg, K. Spekkens, T. Westmeier, T. N. Reynolds, P. Venkataraman, S. Goliath, A. X. Shen, R. Halloran, A. Bosma, B. Catinella, W. J. G. de Blok, H. Dénes, E. M. Di Teodoro, A. Elagali, B.-Q. For, C. Howlett, G. I. G. Józsa, P. Kamphuis, D. Kleiner, B. Koribalski, K. Lee-Waddell, F. Lelli, X. Lin, C. Murugeshan, S. Oh, J. Rhee, T. C. Scott, L. Staveley-Smith, J. M. van der Hulst, L. Verdes-Montenegro, J. Wang, and O. I. Wong. WALLABY Pilot Survey: Public release of HI kinematic models for more than 100 galaxies from phase 1 of ASKAP pilot observations. *Publications of the Astronomical Society of Australia*, 39, 2022. ISSN 1323-3580, 1448-6083. doi: 10.1017/pasa.2022.43. URL http://arxiv.org/abs/2211.07333.

N Deg, R Palleske, K Spekkens, J Wang, T Jarrett, J English, X Lin, J Yeung, J.R. Mould, B Catinella, H Dénes, A Elagali, B.Q. For, P Kamphuis, B.S. Koribalski, K. Lee-Waddell, C. Murugeshan, S. Oh, J. Rhee, P. Serra, T. Westmeier, O.I. Wong, K. Bekki, A. Bosma, C. Carignan, B.W. Holwerda, and N. Yu. WALLABY Pilot Survey: the potential Polar Ring Galaxies NGC 4632 and NGC 6156. *Monthly Notices of the Royal Astronomical Society, in press*, 2023.

Arjun Dey, David J. Schlegel, Dustin Lang, Robert Blum, Kaylan Burleigh, Xiaohui Fan, Joseph R. Findlay, Doug Finkbeiner, David Herrera, Stéphanie Juneau, Martin Landriau, Michael Levi, Ian McGreer, Aaron Meisner, Adam D. Myers, John Moustakas, Peter Nugent, Anna Patej, Edward F. Schlafly, Alistair R. Walker, Francisco Valdes, Benjamin A. Weaver, Christophe Yèche, Hu Zou, Xu Zhou, Behzad Abareshi, T. M. C. Abbott, Bela Abolfathi, C. Aguilera, Shadab Alam, Lori Allen, A. Alvarez, James Annis, Behzad Ansarinejad, Marie Aubert, Jacqueline Beechert, Eric F. Bell, Segev Y. BenZvi, Florian Beutler, Richard M. Bielby, Adam S. Bolton, César Briceño, Elizabeth J. Buckley-Geer, Karen Butler, Annalisa Calamida, Raymond G. Carlberg, Paul Carter, Ricard Casas, Francisco J. Castander, Yumi Choi, Johan Comparat, Elena Cukanovaite, Timothée Delubac, Kaitlin DeVries, Sharmila Dey, Govinda Dhungana, Mark Dickinson, Zhejie Ding, John B. Donaldson, Yutong Duan, Christopher J. Duckworth, Sarah Eftekharzadeh, Daniel J. Eisenstein, Thomas Etourneau, Parker A. Fagrelius, Jay Farihi, Mike Fitzpatrick, Andreu Font-Ribera, Leah Fulmer, Boris T. Gänsicke, Enrique Gaztanaga, Koshy George, David W. Gerdes, Satya Gontcho A Gontcho, Claudio Gorgoni, Gregory Green, Julien Guy, Diane Harmer, M. Hernandez, Klaus Honscheid, Lijuan (Wendy) Huang, David J. James, Buell T. Jannuzi, Linhua Jiang, Richard Joyce, Armin Karcher, Sonia Karkar, Robert Kehoe, Jean-Paul Kneib, Andrea Kueter-Young, Ting-Wen Lan, Tod R. Lauer, Laurent Le Guillou, Auguste Le Van Suu, Jae Hyeon Lee, Michael Lesser, Laurence Perreault Levasseur, Ting S. Li, Justin L. Mann, Robert Marshall, C. E. Martínez-Vázquez, Paul Martini, Hélion Du Mas Des Bourboux, Sean McManus, Tobias Gabriel Meier, Brice Ménard, Nigel Metcalfe, Andrea Muñoz-Gutiérrez, Joan Najita, Kevin Napier, Gautham Narayan, Jeffrey A. Newman, Jundan Nie, Brian Nord, Dara J. Norman, Knut A. G. Olsen, Anthony Paat, Nathalie Palanque-Delabrouille, Xiyan Peng, Claire L. Poppett, Megan R. Poremba, Abhishek Prakash, David Rabinowitz, Anand Raichoor, Mehdi Rezaie, A. N. Robertson, Natalie A. Roe, Ashley J. Ross, Nicholas P. Ross, Gregory Rudnick, Sasha Safonova, Abhijit Saha, F. Javier Sánchez, Elodie Savary, Heidi Schweiker, Adam Scott, Hee-Jong Seo, Huanyuan Shan, David R. Silva, Zachary Slepian, Christian Soto, David Sprayberry, Ryan Staten, Coley M. Stillman, Robert J. Stupak, David L. Summers, Suk Sien Tie, H. Tirado, Mariana Vargas-Magaña, A. Katherina Vivas, Risa H. Wechsler, Doug Williams, Jinyi Yang, Qian Yang, Tolga Yapici, Dennis Zaritsky, A. Zenteno, Kai Zhang, Tianmeng Zhang, Rongpu Zhou, and Zhimin Zhou. Overview of the DESI Legacy Imaging Surveys. *The Astronomical Journal*, 157(5):168,

April 2019. ISSN 1538-3881. doi: 10.3847/1538-3881/ab089d. URL https://iopscience.iop.org/article/10.3847/1538-3881/ab089d.

A. Fedorov, R. Beichel, J. Kalpathy-Cramer, J. Finet, J-C. Fillion-Robin, S. Pujol, C. Bauer, D. Jennings, F.M. Fennessy, M. Sonka, J. Buatti, S.R. Aylward, J.V. Miller, S. Pieper, and R. Kikinis. 3D Slicer as an Image Computing Platform for the Quantitative Imaging Network, November 2012.

Aidan Hotan. The ASKAP radio telescope, 2022. URL https://www.atnf.csiro.au/projects/askap/index.html.

G. I. G. Józsa, F. Kenn, U. Klein, and T. A. Oosterloo. Kinematic modelling of disk galaxies: I. A new method to fit tilted rings to data cubes. *Astronomy & Astrophysics*, 468(2):731–774, June 2007. ISSN 0004-6361, 1432-0746. doi: 10.1051/0004-6361:20066164. URL http://www.aanda.org/10.1051/0004-6361:20066164.

P. Kamphuis, G. I. G. Józsa, S-.H. Oh, K. Spekkens, N. Urbancic, P. Serra, B. S. Koribalski, and R.-J. Dettmar. Automated kinematic modelling of warped galaxy discs in large H i surveys: 3D tilted-ring fitting of H i emission cubes. *Monthly Notices of the Royal Astronomical Society*, 452(3):3139–3158, September 2015. ISSN 0035-8711, 1365-2966. doi: 10.1093/mnras/stv1480. URL https://academic.oup.com/mnras/article-lookup/doi/10.1093/mnras/stv1480.

S. Khoperskov, A. Moiseev, A Khoperskov, and A.S. Saburova. The Shape of Dark Matter Halo in the Polar Ring Galaxy NGC 4262. ASP Conference Series, page 221, INAF-Osservatorio Astronomico di Capodimonte, Napoli, Italy, May 2014a. URL https://articles.adsabs.harvard.edu/pdf/2014ASPC..486..221K.

S. A. Khoperskov, A. V. Moiseev, and A. V. Khoperskov. Polar rings dynamics in the triaxial dark matter halo. *Memorie della Società Astronomica Italiana Supplementi*, 25:51, 2013. doi: 10.48550/ARXIV.1211.1307. URL https://arxiv.org/abs/1211.1307.

S. A. Khoperskov, A. V. Moiseev, A. V. Khoperskov, and A. S. Saburova. To be or not to be oblate: the shape of the dark matter halo in polar ring galaxies. *Monthly Notices of the Royal Astronomical Society*, 441(3):2650–2662, May 2014b. ISSN 0035-8711, 1365-2966. doi: 10.1093/mnras/stu692. URL https://academic.oup.com/mnras/article-lookup/doi/10.1093/mnras/stu692.

Bärbel S. Koribalski, L. Staveley-Smith, T. Westmeier, P. Serra, K. Spekkens, O. I. Wong, K. Lee-Waddell, C. D. P. Lagos, D. Obreschkow, E. V. Ryan-Weber, M. Zwaan, V. Kilborn, G. Bekiaris, K. Bekki, F. Bigiel, A. Boselli, A. Bosma, B. Catinella, G. Chauhan, M. E. Cluver, M. Colless, H. M. Courtois, R. A. Crain, W. J. G. de Blok, H. Dénes, A. R. Duffy, A. Elagali, C. J. Fluke, B. Q. For, G. Heald, P. A. Henning, K. M. Hess, B. W. Holwerda, C. Howlett, T. Jarrett, D. H. Jones, M. G. Jones, G. I. G. Józsa, R. Jurek, E. Jütte, P. Kamphuis, I. Karachentsev, J. Kerp, D. Kleiner, R. C. Kraan-Korteweg, Á. R. López-Sánchez, J. Madrid, M. Meyer, J. Mould, C. Murugeshan, R. P. Norris, S. H. Oh, T. A. Oosterloo, A. Popping, M. Putman, T. N. Reynolds, J. Rhee, A. S. G. Robotham, S. Ryder, A. C. Schröder, Li Shao, A. R. H. Stevens, E. N. Taylor, J. M. vanÂ der Hulst, L. Verdes-Montenegro, B. P. Wakker, J. Wang, M. Whiting, B. Winkel, and C. Wolf. WALLABY - an SKA Pathfinder HI survey. , 365(7):118, July 2020. doi: 10.1007/s10509-020-03831-4.

S. Laustsen and R. M. West. NGC 4650 A: A nearly edge-on ring galaxy? *Journal of Astrophysics and Astronomy*, 1(2):177–187, December 1980. ISSN 0250-6335, 0973-7758. doi: 10.1007/BF02714236. URL `http://link.springer.com/10.1007/BF02714236`.

Andrea V. Macciò, Ben Moore, and Joachim Stadel. The Origin of Polar Ring Galaxies: Evidence for Galaxy Formation by Cold Accretion. *The Astrophysical Journal*, 636(1):L25–L28, January 2006. ISSN 0004-637X, 1538-4357. doi: 10.1086/499778. URL `https://iopscience.iop.org/article/10.1086/499778`.

Jonathan M. Marr, Ronald Lee Snell, and Stanley Kurtz. *Fundamentals of Radio Astronomy: Observational Methods*. CRC Press, Taylor & Francis Group, Boca Raton, 2016. ISBN 9781498770194. OCLC: 958800564.

A. Moiseev, S. Khoperskov, A. Khoperskov, K. Smirnova, A. Smirnova, A. Saburova, and V. Reshetnikov. Structure and Kinematics of Polar Ring Galaxies: New Observations and Estimation of the Dark Halo Shape. *Open Astronomy*, 24(1), January 2015. ISSN 2543-6376. doi: 10.1515/astro-2017-0205. URL `https://www.degruyter.com/document/doi/10.1515/astro-2017-0205/html`.

Alexei Moiseev. Polar structures in late-type galaxies. *Astronomical Society of the Pacific*, 483:61, 2014. doi: 10.48550/ARXIV.1401.7912. URL `https://arxiv.org/abs/1401.7912`.

Rayleigh. XXXI. Investigations in optics, with special reference to the spectroscope. *The London, Edinburgh, and Dublin Philosophical Magazine and Journal of Science*, 8(49):261–274, October 1879. ISSN 1941-5982, 1941-5990. doi: 10.1080/14786447908639684. URL https://www.tandfonline.com/doi/full/10.1080/14786447908639684.

T. Rector. Polar Ring Galaxy NGC 660, November 2014. URL https://apod.nasa.gov/apod/ap141108.html.

V. Reshetnikov and N. Sotnikova. Global structure and formation of polar-ring galaxies. *Astronomy and Astrophysics*, 1997. doi: 10.48550/ARXIV.ASTRO-PH/9704047. URL https://arxiv.org/abs/astro-ph/9704047.

V. P. Reshetnikov, V. A. Hagen-Thorn, and V. A. Yakovleva. Photometric study of polar-ring galaxies. III. Forming rings. *Astronomy & Astrophysics*, 1996. doi: 10.48550/ARXIV.ASTRO-PH/9608100. URL https://arxiv.org/abs/astro-ph/9608100.

Vladimir P Reshetnikov and Aleksandr V Mosenkov. New candidates to polar-ring galaxies from the Sloan Digital Sky Survey. *Monthly Notices of the Royal Astronomical Society*, 483(2):1470–1480, February 2019. ISSN 0035-8711, 1365-2966. doi: 10.1093/mnras/sty3209. URL https://academic.oup.com/mnras/article/483/2/1470/5211088.

V.P. Reshetnikov, M. Faúndez-Abans, and M. de Oliveira-Abans. Polar-Ring Galaxies: New Candidates and Statistics. *Astronomy Letters*, 37(3):171–180, 2011. ISSN 1063-7737. doi: 10.1134/S1063773711030042.

D. H. Rogstad, I. A. Lockart, and M. C. H. Wright. Aperture-synthesis observations of H I in the galaxy M 83. *The Astrophysical Journal*, 193:309, October 1974. ISSN 0004-637X, 1538-4357. doi: 10.1086/153164. URL http://adsabs.harvard.edu/doi/10.1086/153164.

F. Schweizer, B. C. Whitmore, and V. C. Rubin. Colliding and Merging Galaxies. II - S0 Galaxies with Polar Rings. *The Astronomical Journal*, 88:909, July 1983. ISSN 00046256. doi: 10.1086/113377. URL http://adsabs.harvard.edu/cgi-bin/bib_query?1983AJ.....88..909S.

Paolo Serra, Tom Oosterloo, Raffaella Morganti, Katherine Alatalo, Leo Blitz, Maxime Bois, Frédéric Bournaud, Martin Bureau, Michele Cappellari, Alison F. Crocker, Roger L. Davies, Timothy A. Davis, P. T. De Zeeuw, Pierre-Alain Duc, Eric Emsellem, Sadegh Khochfar, Davor Krajnović, Harald Kuntschner, Pierre-Yves Lablanche, Richard M. McDermid, Thorsten

Naab, Marc Sarzi, Nicholas Scott, Scott C. Trager, Anne-Marie Weijmans, and Lisa M. Young. The ATLAS3D Project - XIII. Mass and Morphology of Hi in Early-Type Galaxies as a Function of Environment: The ATLAS3D Project - XIII. Neutral Hydrogen. *Monthly Notices of the Royal Astronomical Society*, 422(3):1835–1862, May 2012. ISSN 00358711. doi: 10.1111/j.1365-2966.2012.20219.x. URL https://academic.oup.com/mnras/article-lookup/doi/10.1111/j.1365-2966.2012.20219.x.

Paolo Serra, Tobias Westmeier, Nadine Giese, Russell Jurek, Lars Flöer, Attila Popping, Benjamin Winkel, Thijs van der Hulst, Martin Meyer, Bärbel S. Koribalski, Lister Staveley-Smith, and Hélène Courtois. SOFIA: a flexible source finder for 3D spectral line data. , 448(2):1922–1929, April 2015. doi: 10.1093/mnras/stv079.

Daniil V Smirnov and Vladimir P Reshetnikov. The luminosity function of ringed galaxies. *Monthly Notices of the Royal Astronomical Society*, 516 (3):3692–3700, September 2022. ISSN 0035-8711, 1365-2966. doi: 10.1093/mnras/stac2549. URL https://academic.oup.com/mnras/article/516/3/3692/6695095.

O. N. Snaith, B. K. Gibson, C. B. Brook, A. Knebe, R. J. Thacker, T. R. Quinn, F. Governato, and P. B. Tissera. The halo shape and evolution of polar disc galaxies: A simulated polar disc galaxy. *Monthly Notices of the Royal Astronomical Society*, 425(3):1967–1979, September 2012. ISSN 00358711. doi: 10.1111/j.1365-2966.2012.21518.x. URL https://academic.oup.com/mnras/article-lookup/doi/10.1111/j.1365-2966.2012.21518.x.

L.S. Sparke and A.L. Cox. New Observations of Polar Ring Galaxies. *Dynamics of Galaxies: from the Early Universe to the Present*, 197, 2000.

M. Spavone, E. Iodice, M. Arnaboldi, G. Longo, and O. Gerhard. Chemical abundances of the PRGs UGC 7576 and UGC 9796: I. Testing the formation scenario. *Astronomy & Astrophysics*, 531:A21, July 2011. ISSN 0004-6361, 1432-0746. doi: 10.1051/0004-6361/201116588. URL http://www.aanda.org/10.1051/0004-6361/201116588.

K. Stanonik, E. Platen, M. A. Aragón-Calvo, J. H. Van Gorkom, R. Van De Weygaert, J. M. Van Der Hulst, and P. J. E. Peebles. Polar Disk Galaxy Found In Wall Between Voids. *The Astrophysical Journal*, 696(1):L6–L9, May 2009. ISSN 0004-637X, 1538-4357. doi: 10.1088/0004-637X/696/1/

L6. URL https://iopscience.iop.org/article/10.1088/0004-637X/696/1/L6.

Yoshiaki Taniguchi, Yoshiaki Sofue, Ken-Ichi Wakamatsu, and Naomasa Nakai. CO emission from the polar-ring S0 galaxy NGC 2685 and origin of the ring structure. *The Astronomical Journal*, 100:1086, October 1990. ISSN 00046256. doi: 10.1086/115581. URL http://adsabs.harvard.edu/cgi-bin/bib_query?1990AJ....100.1086T.

Hubble Heritage Team. Ring around NGC 4650A, May 1999. URL https://esahubble.org/images/opo9916a/.

E. M. Di Teodoro and F. Fraternali. 3D barolo: a new 3D algorithm to derive rotation curves of galaxies. *Monthly Notices of the Royal Astronomical Society*, 451(3):3021–3033, August 2015. ISSN 1365-2966, 0035-8711. doi: 10.1093/mnras/stv1213. URL http://academic.oup.com/mnras/article/451/3/3021/1198172/3Dbarolo-a-new-3D-algorithm-to-derive-rotation.

W. Van Driel, F. Combes, F. Casoli, M. Gerin, N. Nakai, T. Miyaji, M. Hamabe, Y. Sofue, T. Ichikawa, S. Yoshida, Y. Kobayashi, F. Geng, T. Minezaki, N. Arimoto, T. Kodama, P. Goudfrooij, P. S. Mulder, K. Wakamatsu, and K. Yanagisawa. Polar ring spiral galaxy NGC 660. *The Astronomical Journal*, 109:942, March 1995. ISSN 00046256. doi: 10.1086/117333. URL http://adsabs.harvard.edu/cgi-bin/bib_query?1995AJ....109..942V.

Ken-Ichi Wakamatsu. Structure of polar ring galaxies - Shock waves in the gas of polar rings. *The Astronomical Journal*, 105:1745, May 1993. ISSN 00046256. doi: 10.1086/116551. URL http://adsabs.harvard.edu/cgi-bin/bib_query?1993AJ....105.1745W.

WALLABY. Overview, 2023. URL https://wallaby-survey.org/overview/.

T. Westmeier, S. Kitaeff, D. Pallot, P. Serra, J. M. van der Hulst, R. J. Jurek, A. Elagali, B. Q. For, D. Kleiner, B. S. Koribalski, K. Lee-Waddell, J. R. Mould, T. N. Reynolds, J. Rhee, and L. Staveley-Smith. SOFIA 2 - an automated, parallel H I source finding pipeline for the WALLABY survey. , 506(3):3962–3976, September 2021. doi: 10.1093/mnras/stab1881.

T. Westmeier, N. Deg, K. Spekkens, T. N. Reynolds, A. X. Shen, S. Gaudet, S. Goliath, M. T. Huynh, P. Venkataraman, X. Lin, T. O'Beirne, B. Catinella, L. Cortese, H. Dénes, A. Elagali, B. Q. For, G. I. G. Józsa,

C. Howlett, J. M. van der Hulst, R. J. Jurek, P. Kamphuis, V. A. Kilborn, D. Kleiner, B. S. Koribalski, K. Lee-Waddell, C. Murugeshan, J. Rhee, P. Serra, L. Shao, L. Staveley-Smith, J. Wang, O. I. Wong, M. A. Zwaan, J. R. Allison, C. S. Anderson, Lewis Ball, D. C. J. Bock, D. Brodrick, J. D. Bunton, F. R. Cooray, N. Gupta, D. B. Hayman, E. K. Mahony, V. A. Moss, A. Ng, S. E. Pearce, W. Raja, D. N. Roxby, M. A. Voronkov, K. A. Warhurst, H. M. Courtois, and K. Said. WALLABY pilot survey: Public release of H I data for almost 600 galaxies from phase 1 of ASKAP pilot observations. , 39:e058, November 2022. doi: 10.1017/pasa.2022.50.

B. C. Whitmore. The intrinsic orientation of S0 galaxies with polar rings. *The Astronomical Journal*, 89:618, May 1984. ISSN 00046256. doi: 10.1086/113557. URL `http://adsabs.harvard.edu/cgi-bin/bib_query?1984AJ....89..618W`.

Bradley C. Whitmore, Ray A. Lucas, Douglas B. McElroy, Thomas Y. Steiman-Cameron, Penny D. Sackett, and Rob P. Olling. New Observations and a Photographic Atlas of Polar-Ring Galaxies. *The Astronomical Journal*, 100:1489, November 1990. ISSN 00046256. doi: 10.1086/115614. URL `http://adsabs.harvard.edu/cgi-bin/bib_query?1990AJ...100.1489W`.

Appendices

A Moment Panel Plots

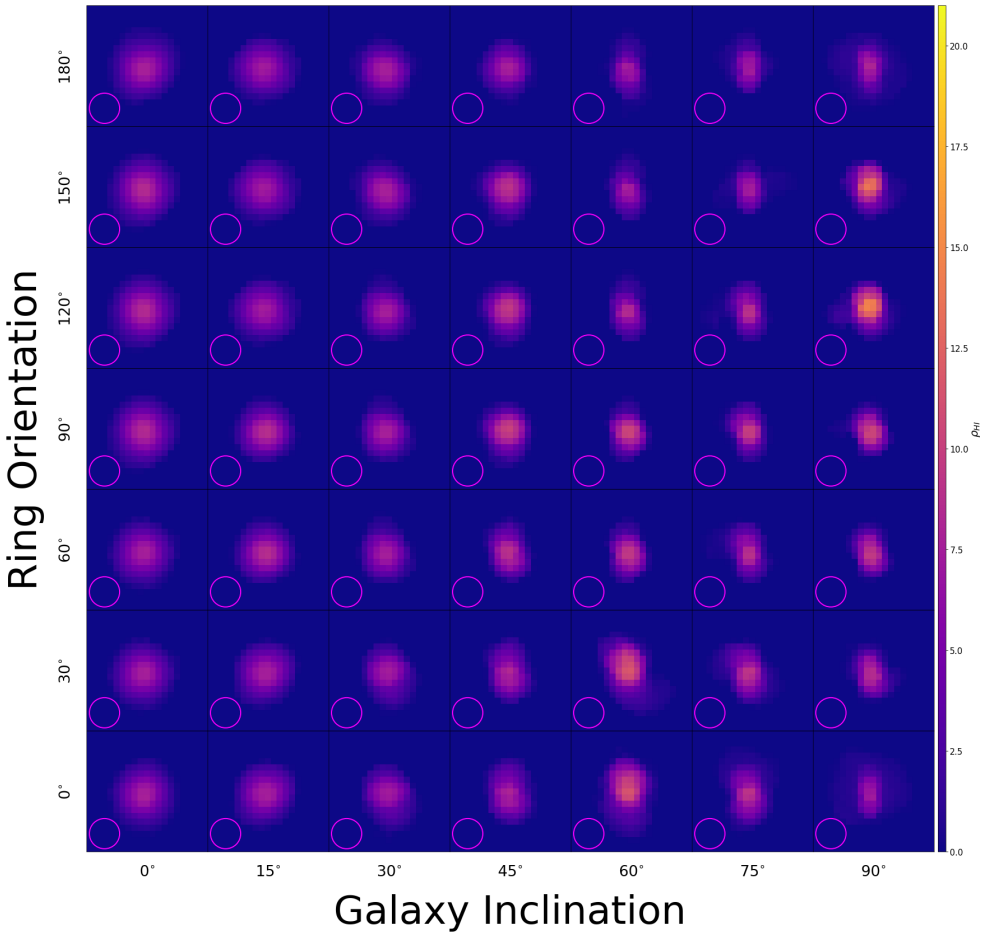

Figure A.1: Moment zero panel plot for the NGC 4632 model galaxy at a resolution of 3 BA. The colour bar on the y-axis depicts the HI density, ρ_{HI}, in units of $M_\odot/pc^2$.

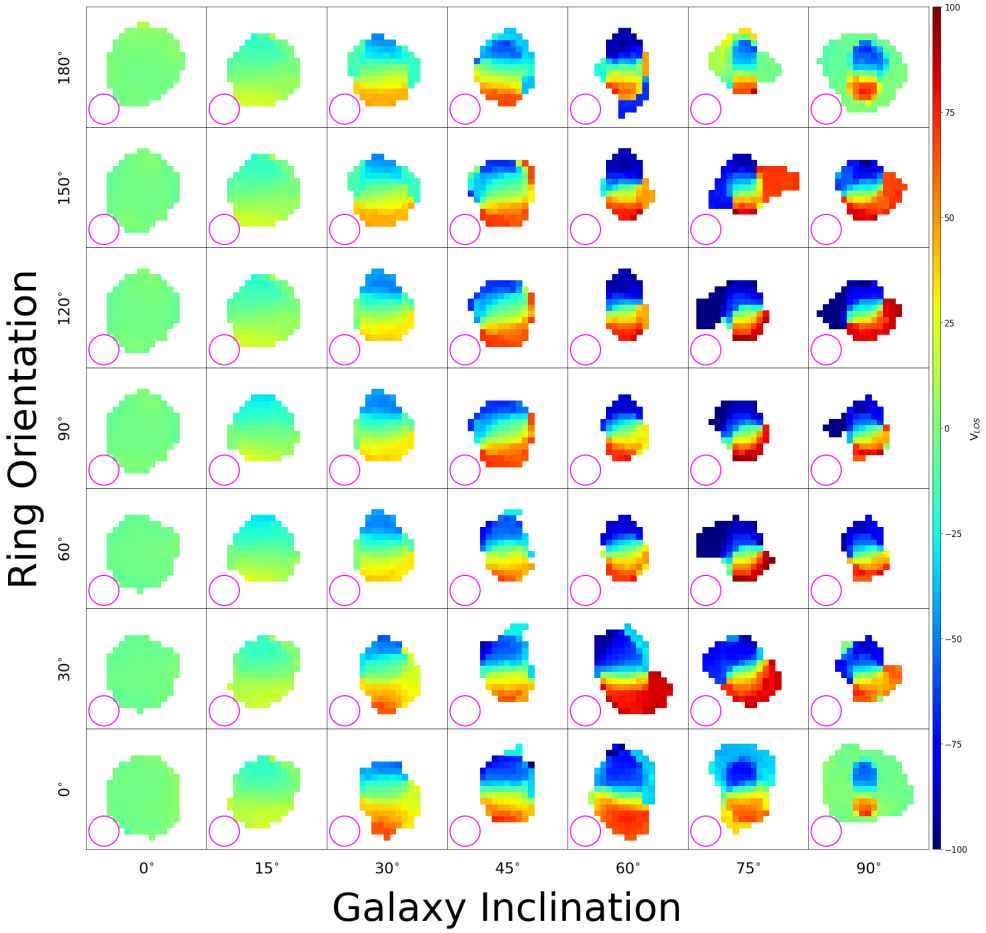

Figure A.2: Moment one panel plot for the NGC 4632 model galaxy at a resolution of 3 BA. The colour bar on the y-axis depicts the line of sight velocity, V_{LOS}, in units of km/s.

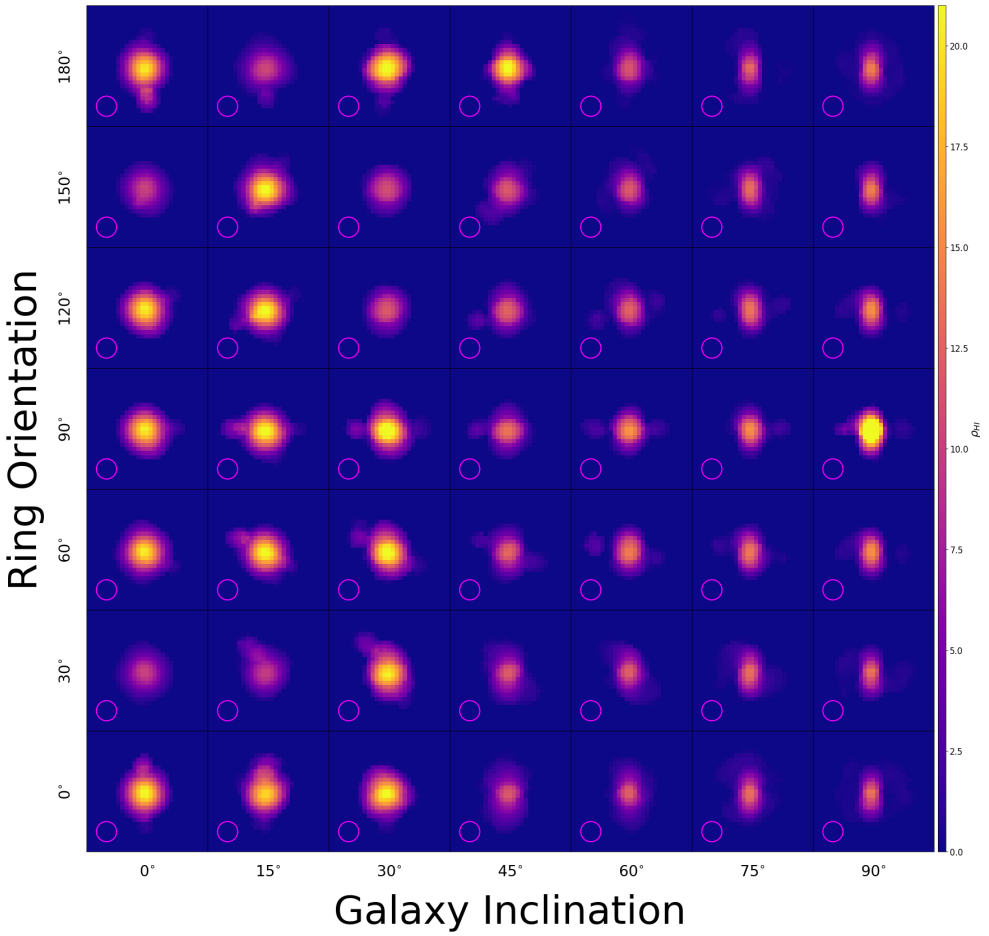

Figure A.3: Moment zero panel plot for the NGC 4632 model galaxy at a resolution of 4 BA. The colour bar on the y-axis depicts the HI density, ρ_{HI}, in units of $M_\odot/pc^2$.

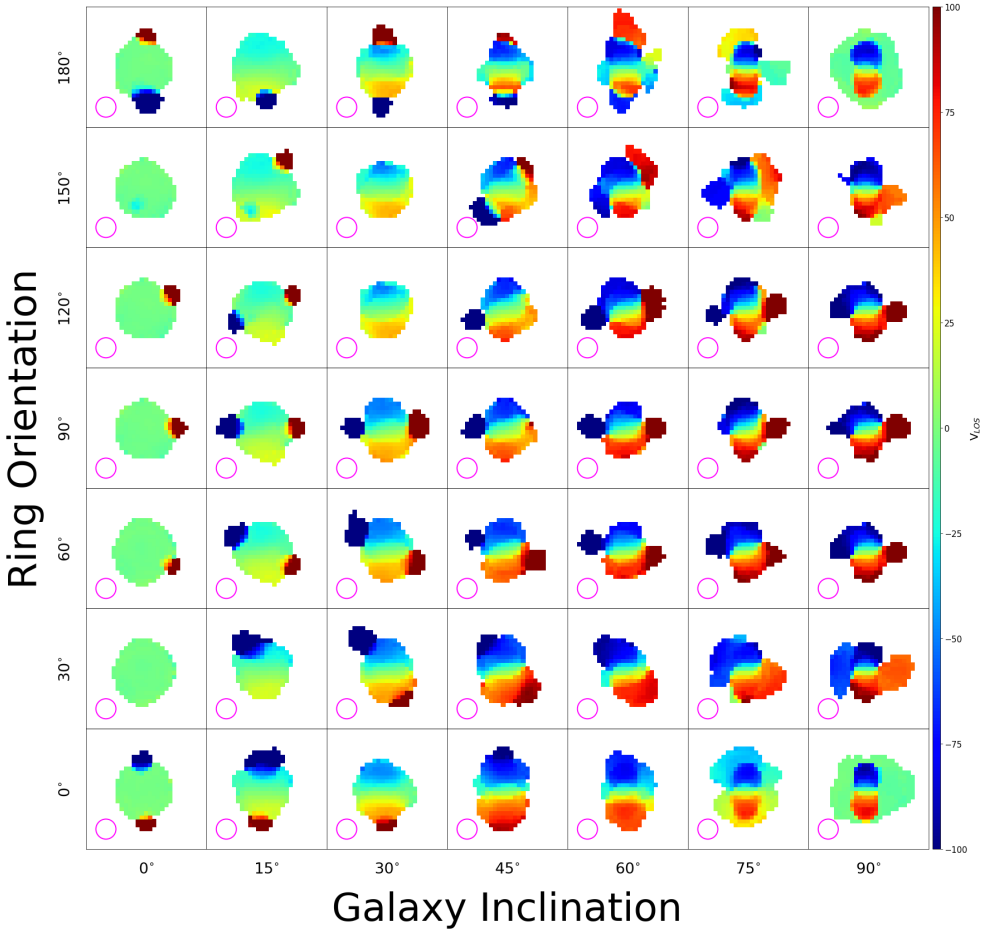

Figure A.4: Moment one panel plot for the NGC 4632 model galaxy at a resolution of 4 BA. The colour bar on the y-axis depicts the line of sight velocity, V_{LOS}, in units of km/s.

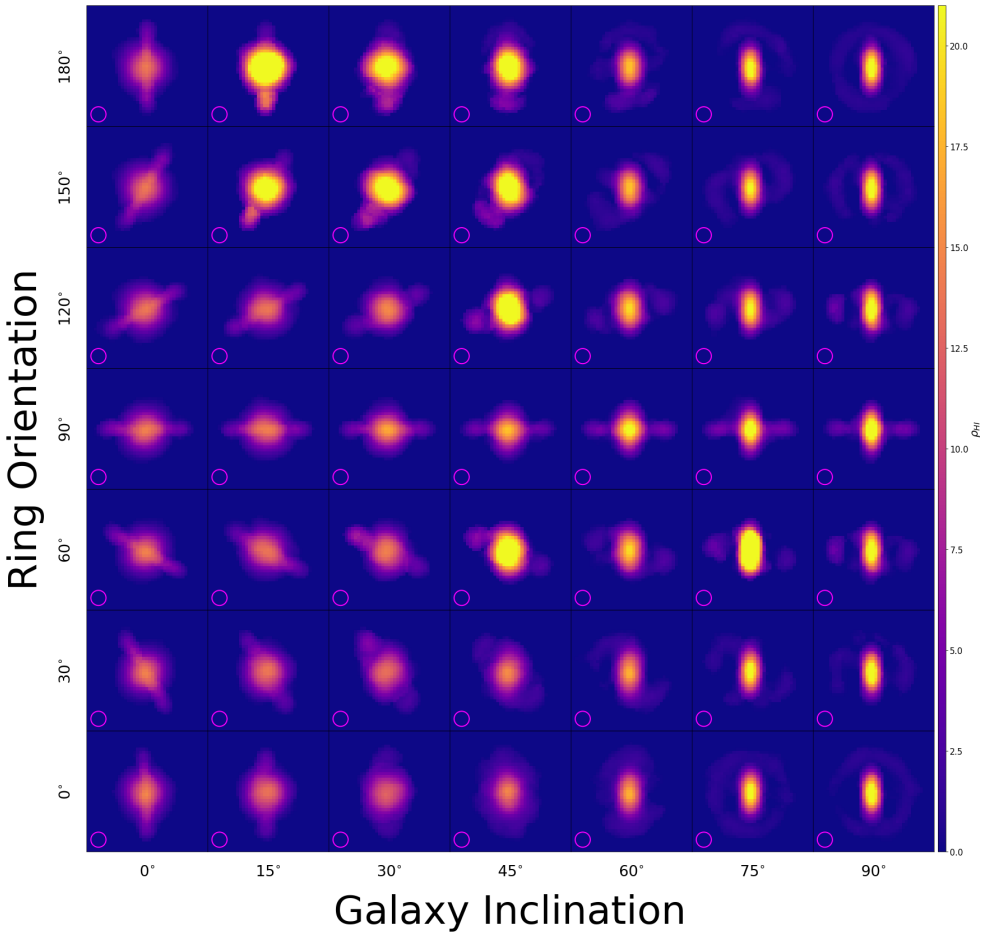

Figure A.5: Moment zero panel plot for the NGC 4632 model galaxy at a resolution of 6 BA. The colour bar on the y-axis depicts the HI density, ρ_{HI}, in units of $M_\odot/pc^2$.

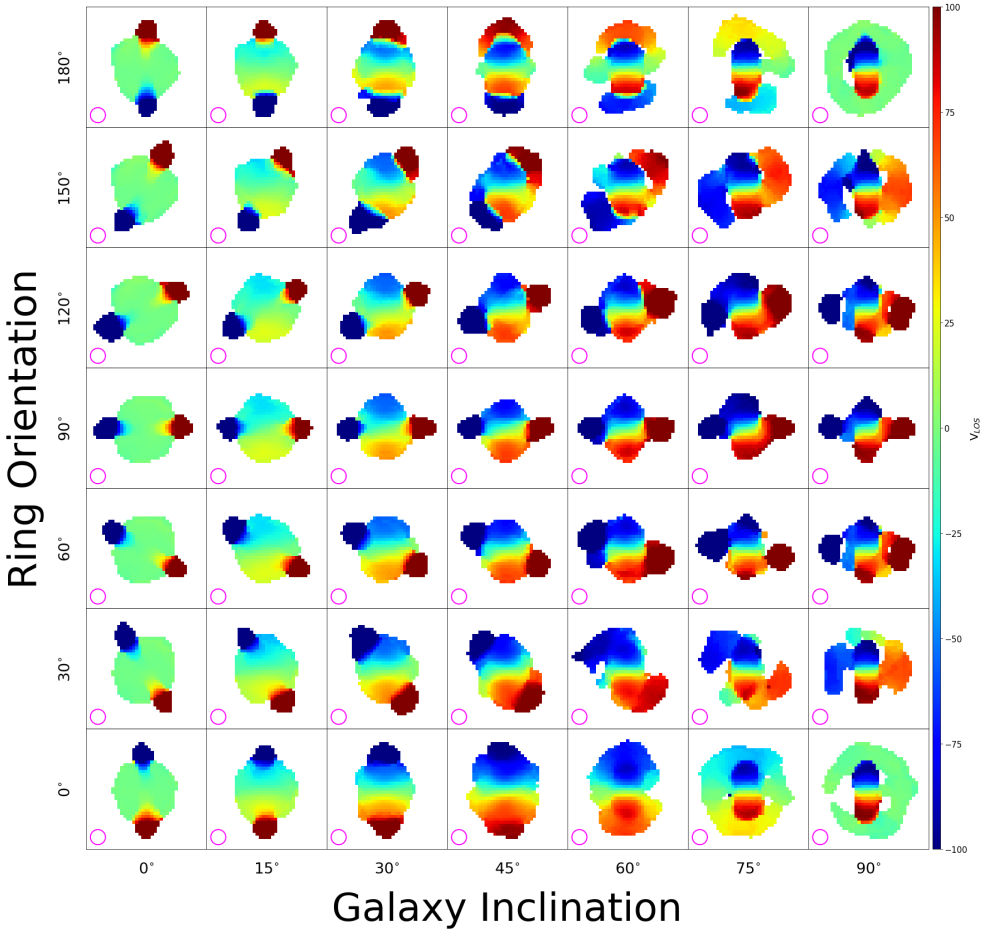

Figure A.6: Moment one panel plot for the NGC 4632 model galaxy at a resolution of 6 BA. The colour bar on the y-axis depicts the line of sight velocity, V_{LOS}, in units of km/s.

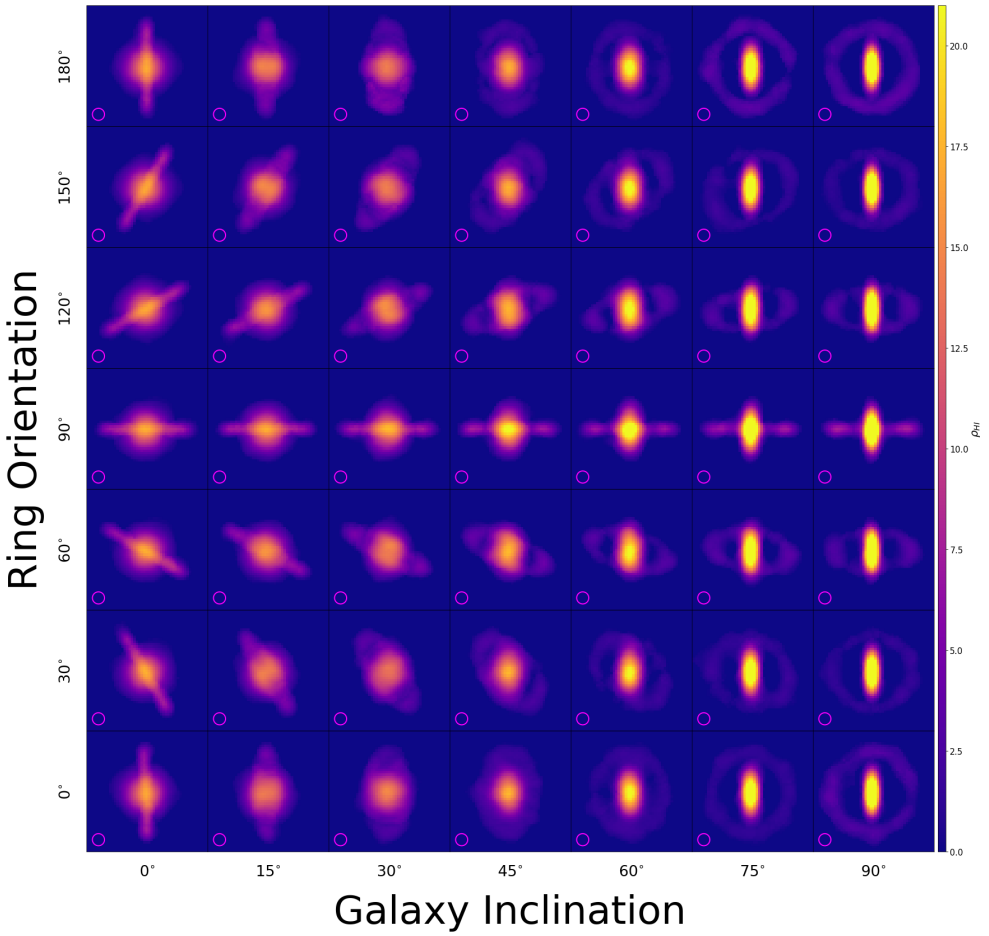

Figure A.7: Moment zero panel plot for the NGC 4632 model galaxy at a resolution of 8 BA. The colour bar on the y-axis depicts the HI density, ρ_{HI}, in units of $M_\odot/pc^2$.

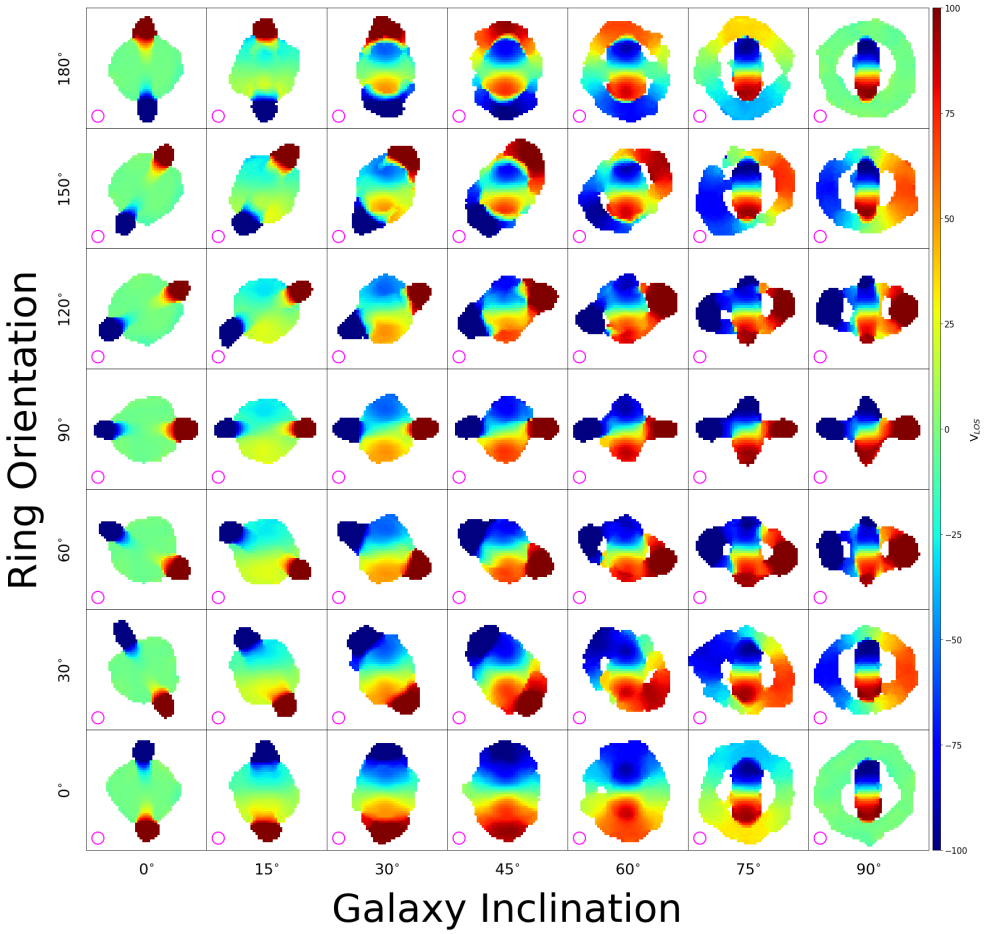

Figure A.8: Moment one panel plot for the NGC 4632 model galaxy at a resolution of 8 BA. The colour bar on the y-axis depicts the line of sight velocity, V_{LOS}, in units of km/s.

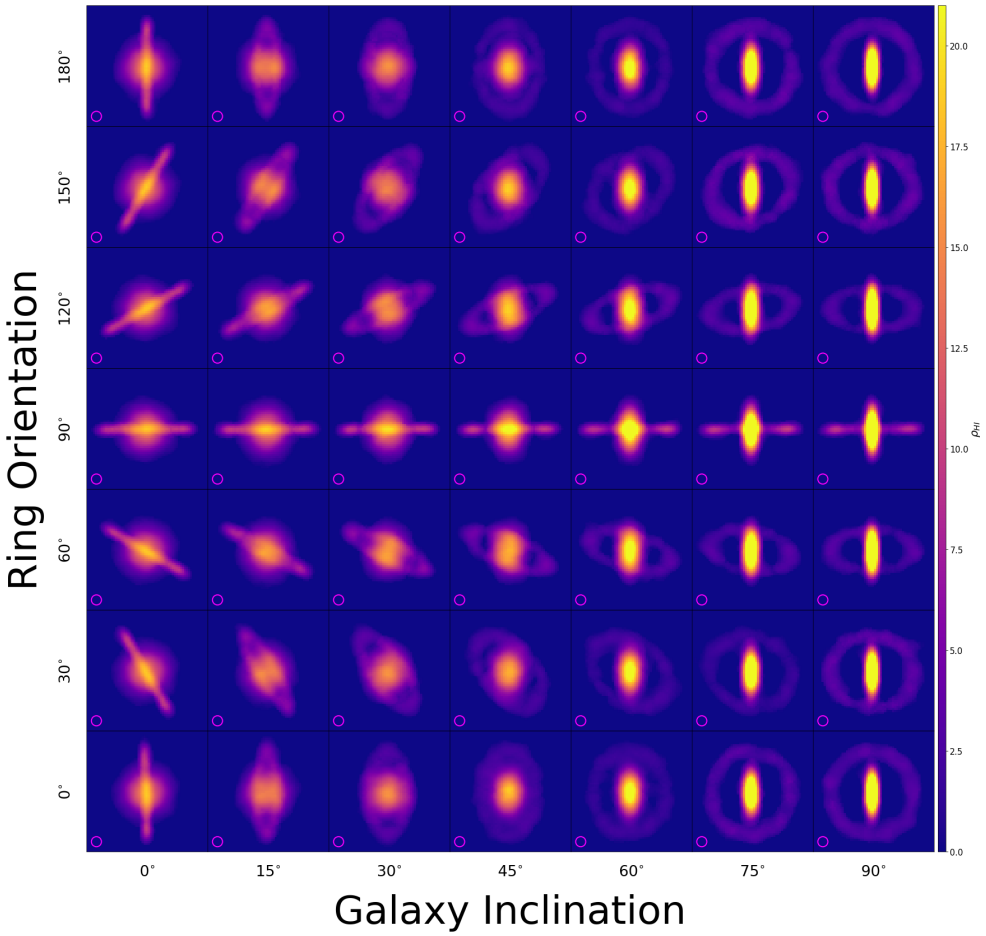

Figure A.9: Moment zero panel plot for the NGC 4632 model galaxy at a resolution of 10 BA. The colour bar on the y-axis depicts the HI density, ρ_{HI}, in units of $M_\odot/pc^2$.

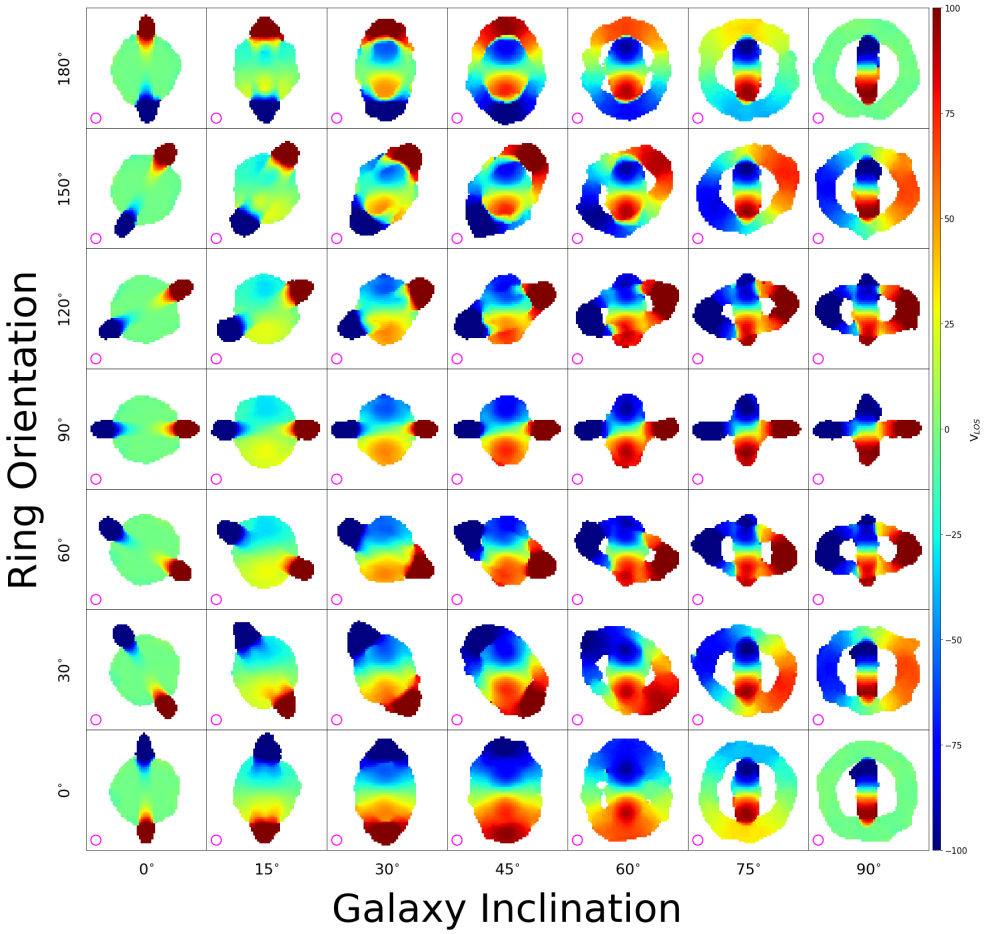

Figure A.10: Moment one panel plot for the NGC 4632 model galaxy at a resolution of 10 BA. The colour bar on the y-axis depicts the line of sight velocity, V_{LOS}, in units of km/s.

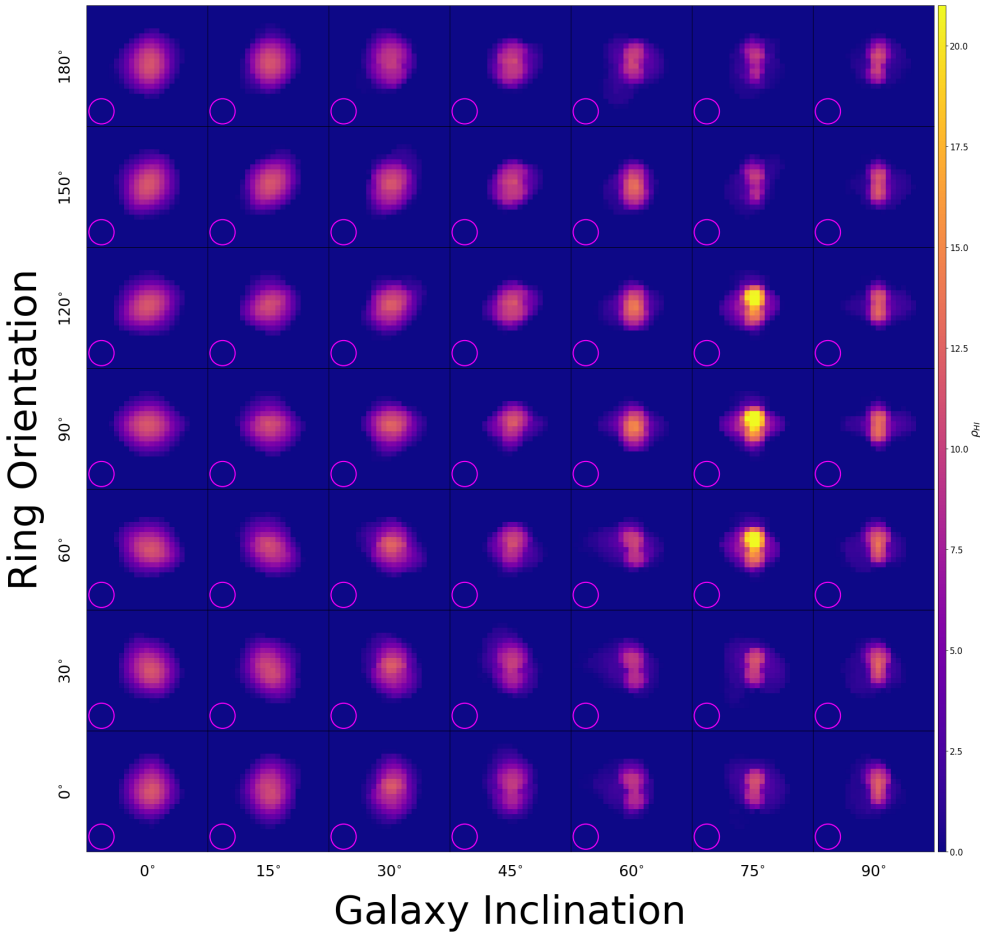

Figure A.11: Moment zero panel plot for the NGC 6156 model galaxy at a resolution of 3 BA. The colour bar on the y-axis depicts the HI density, ρ_{HI}, in units of $M_{\odot}/pc^2$.

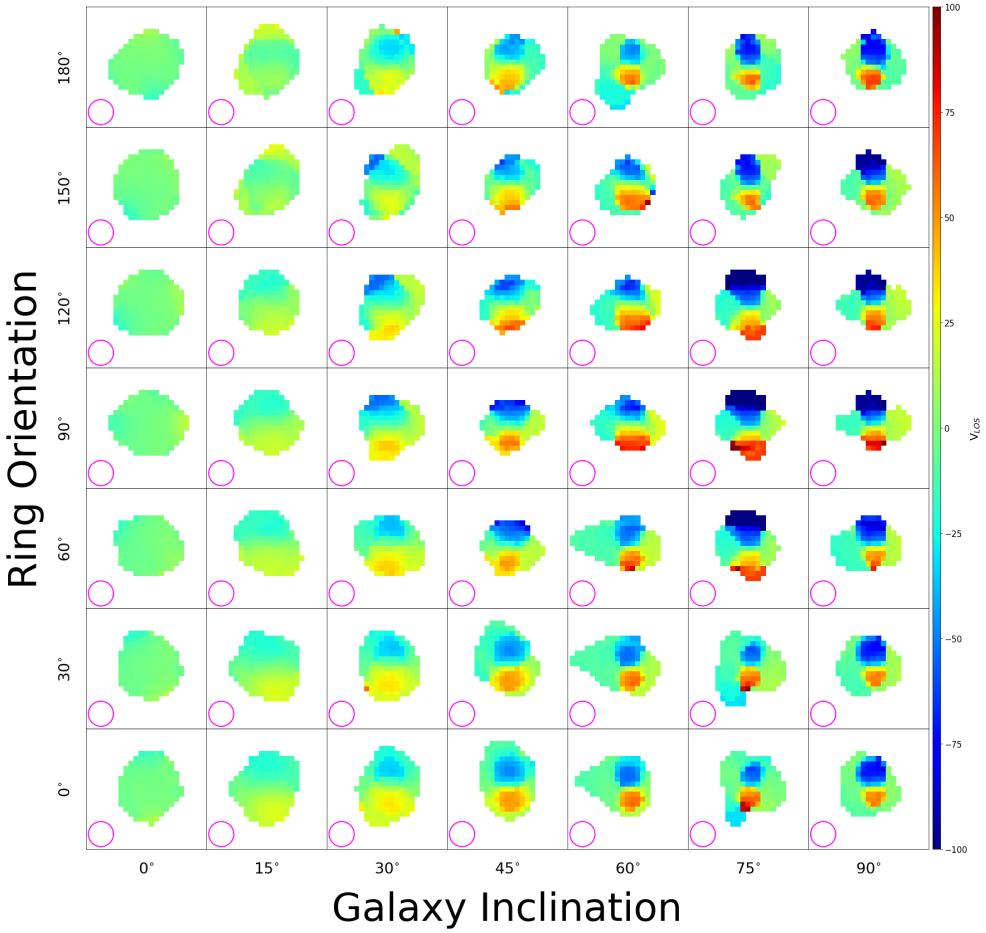

Figure A.12: Moment one panel plot for the NGC 6156 model galaxy at a resolution of 3 BA. The colour bar on the y-axis depicts the line of sight velocity, V_{LOS}, in units of km/s.

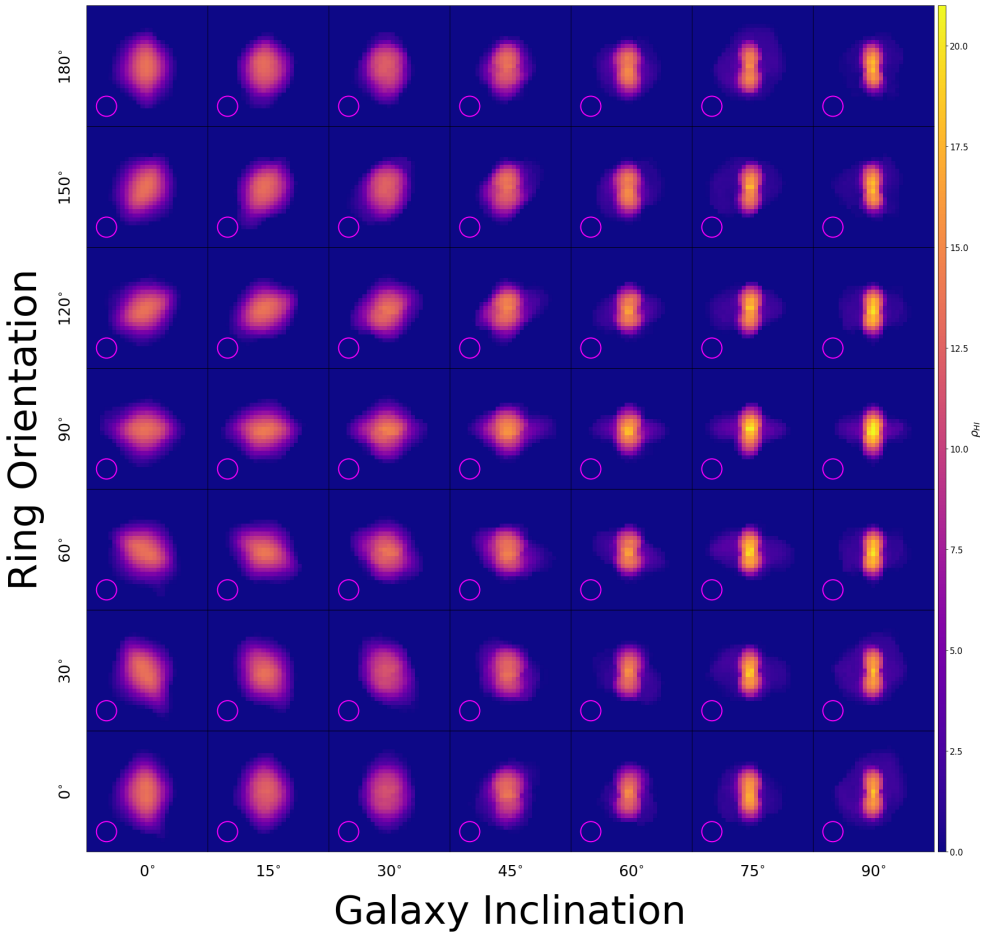

Figure A.13: Moment zero panel plot for the NGC 6156 model galaxy at a resolution of 4 BA. The colour bar on the y-axis depicts the HI density, ρ_{HI}, in units of $M_\odot/pc^2$.

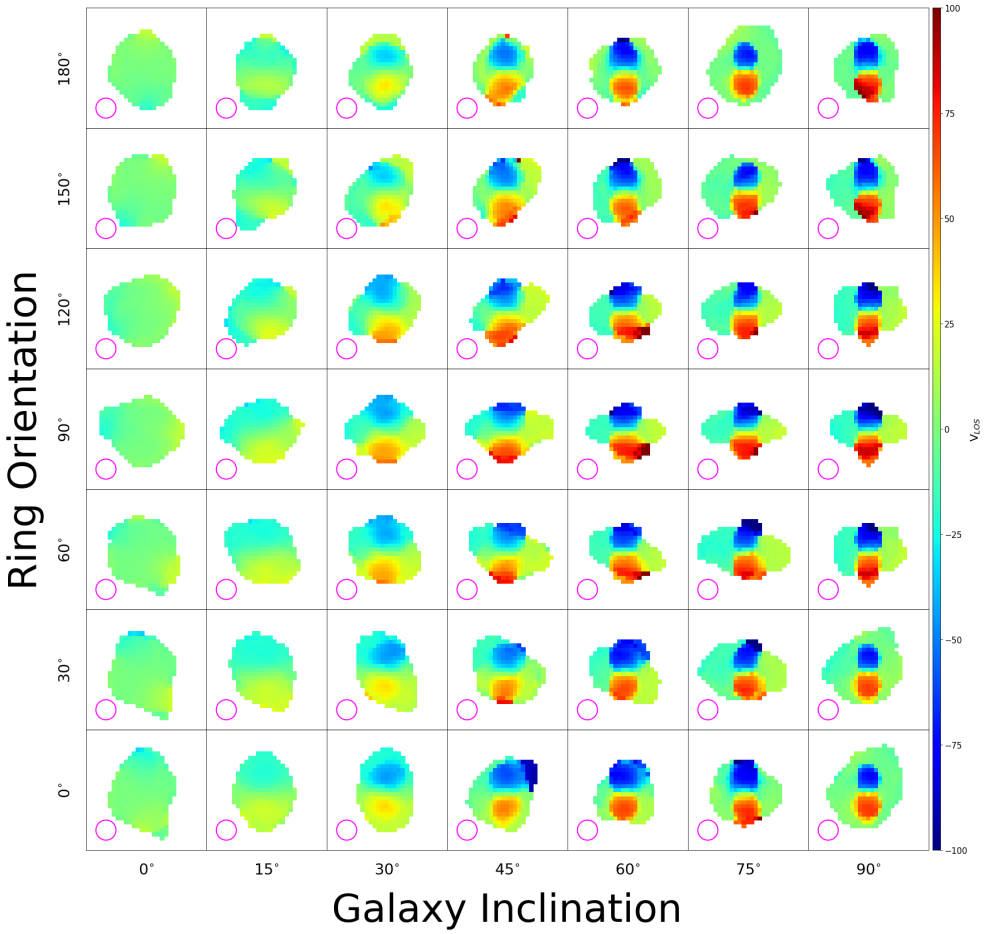

Figure A.14: Moment one panel plot for the NGC 6156 model galaxy at a resolution of 4 BA. The colour bar on the y-axis depicts the line of sight velocity, V_{LOS}, in units of km/s.

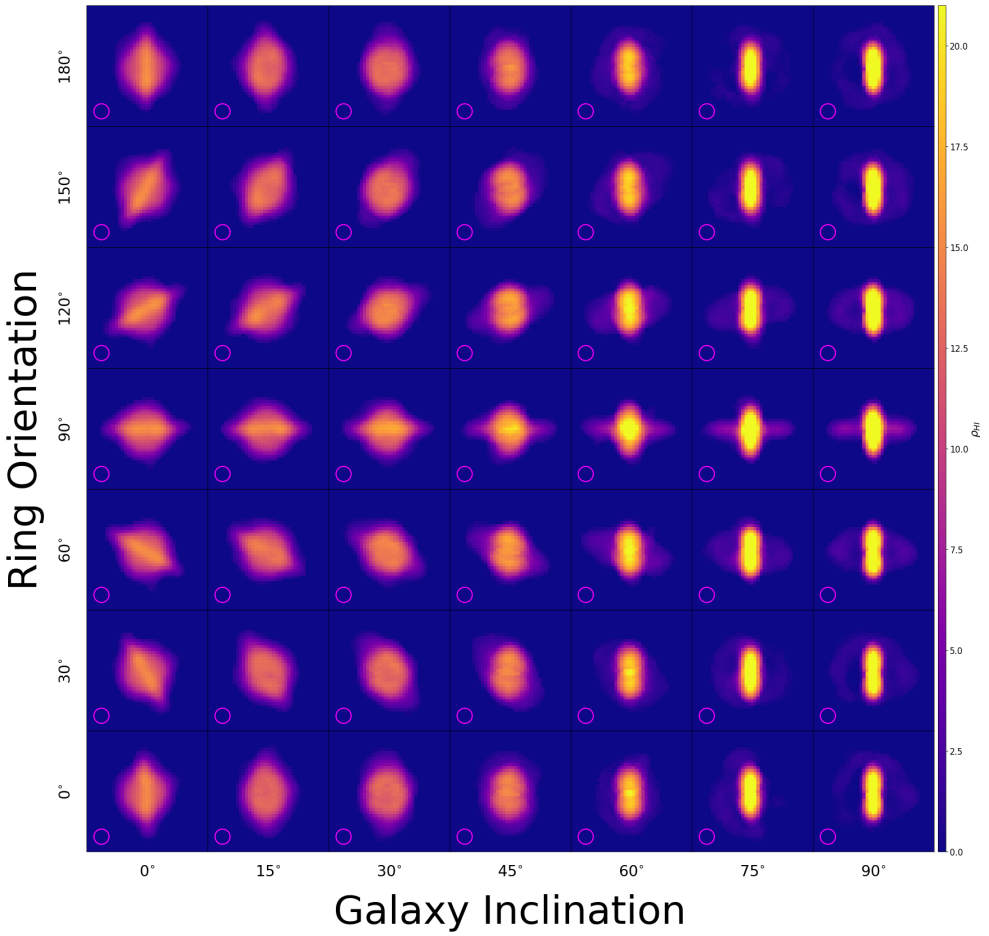

Figure A.15: Moment zero panel plot for the NGC 6156 model galaxy at a resolution of 6 BA. The colour bar on the y-axis depicts the HI density, ρ_{HI}, in units of $M_\odot/pc^2$.

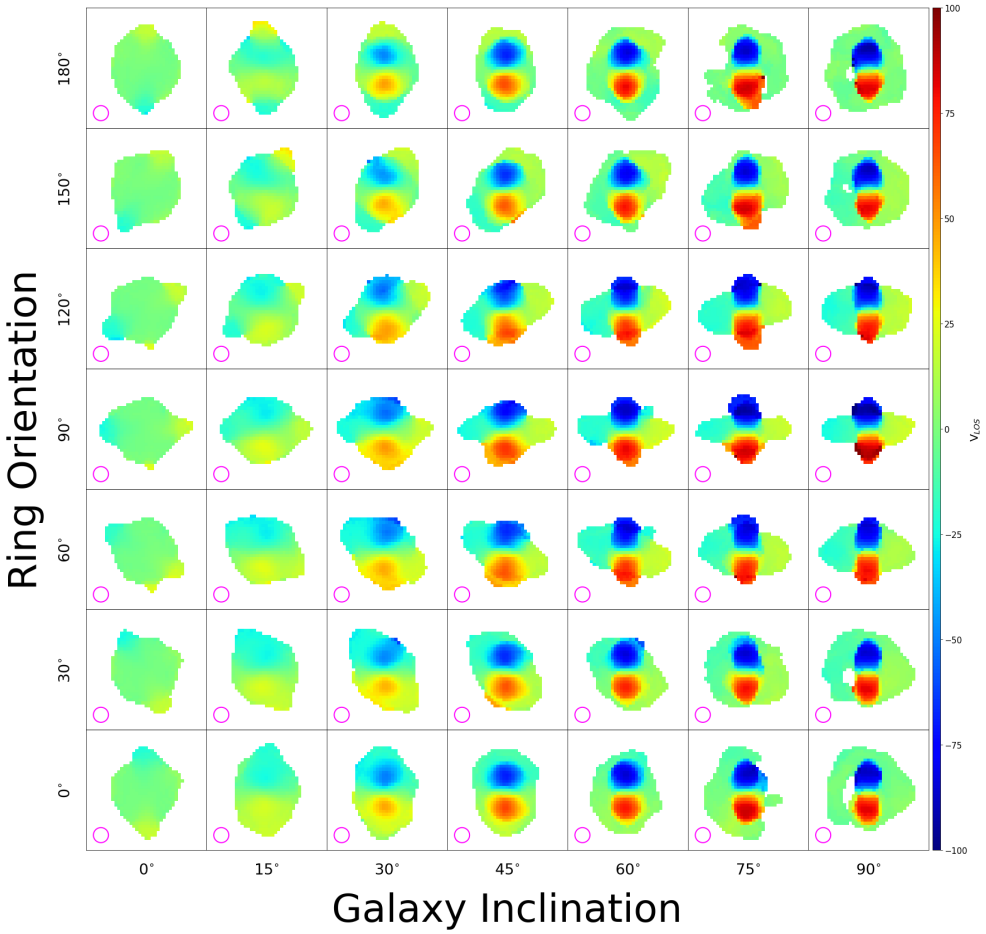

Figure A.16: Moment one panel plot for the NGC 6156 model galaxy at a resolution of 6 BA. The colour bar on the y-axis depicts the line of sight velocity, V_{LOS}, in units of km/s.

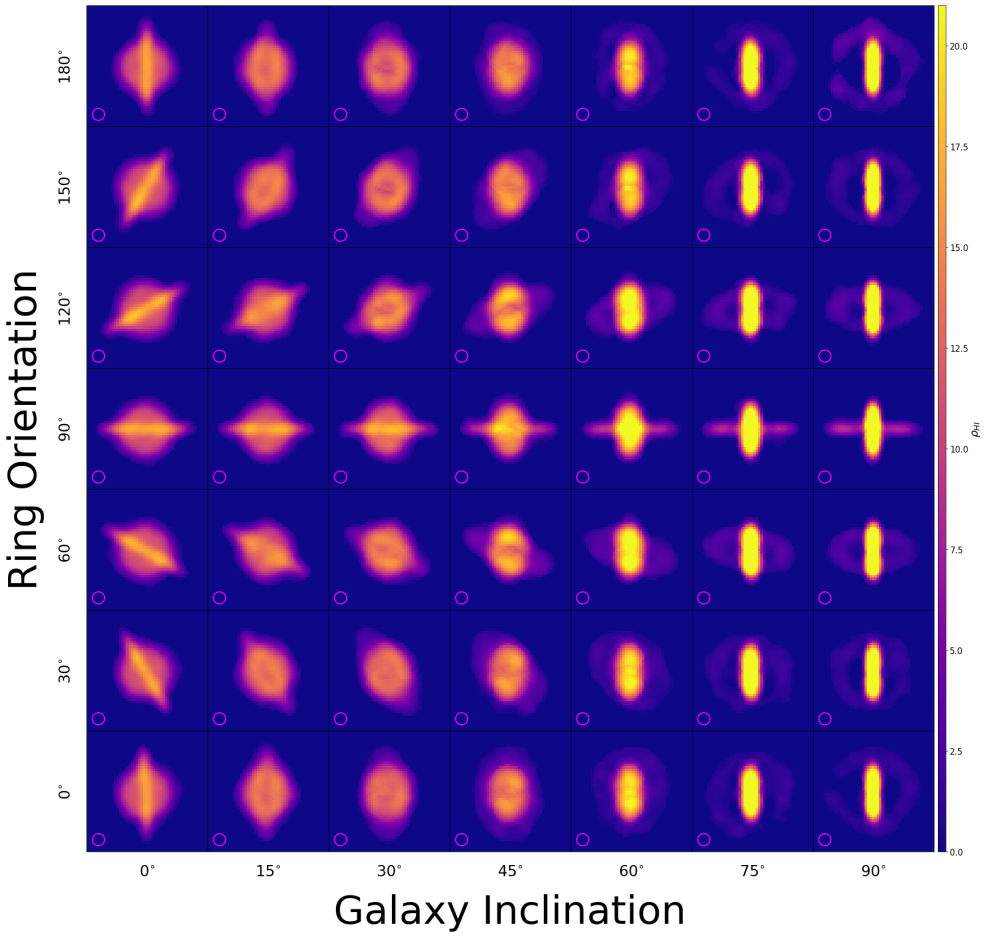

Figure A.17: Moment zero panel plot for the NGC 6156 model galaxy at a resolution of 8 BA. The colour bar on the y-axis depicts the HI density, ρ_{HI}, in units of $M_{\odot}/pc^2$.

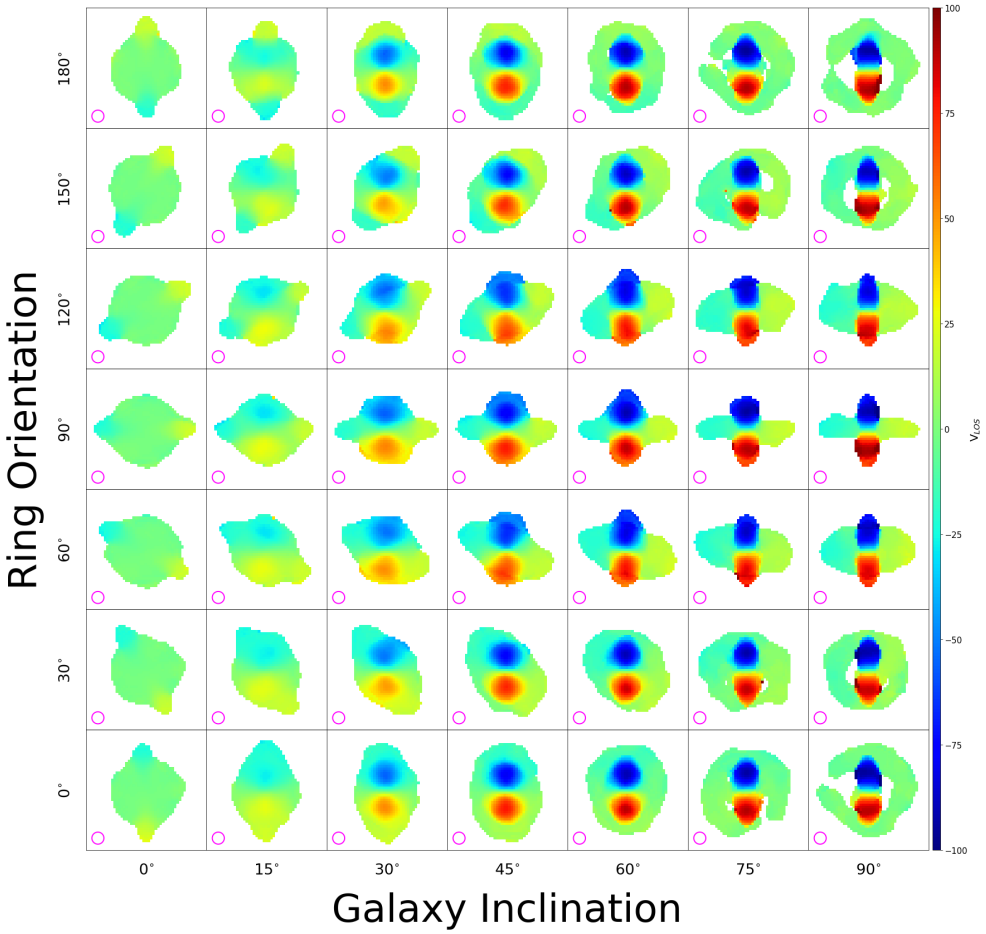

Figure A.18: Moment one panel plot for the NGC 6156 model galaxy at a resolution of 8 BA. The colour bar on the y-axis depicts the line of sight velocity, V_{LOS}, in units of km/s.

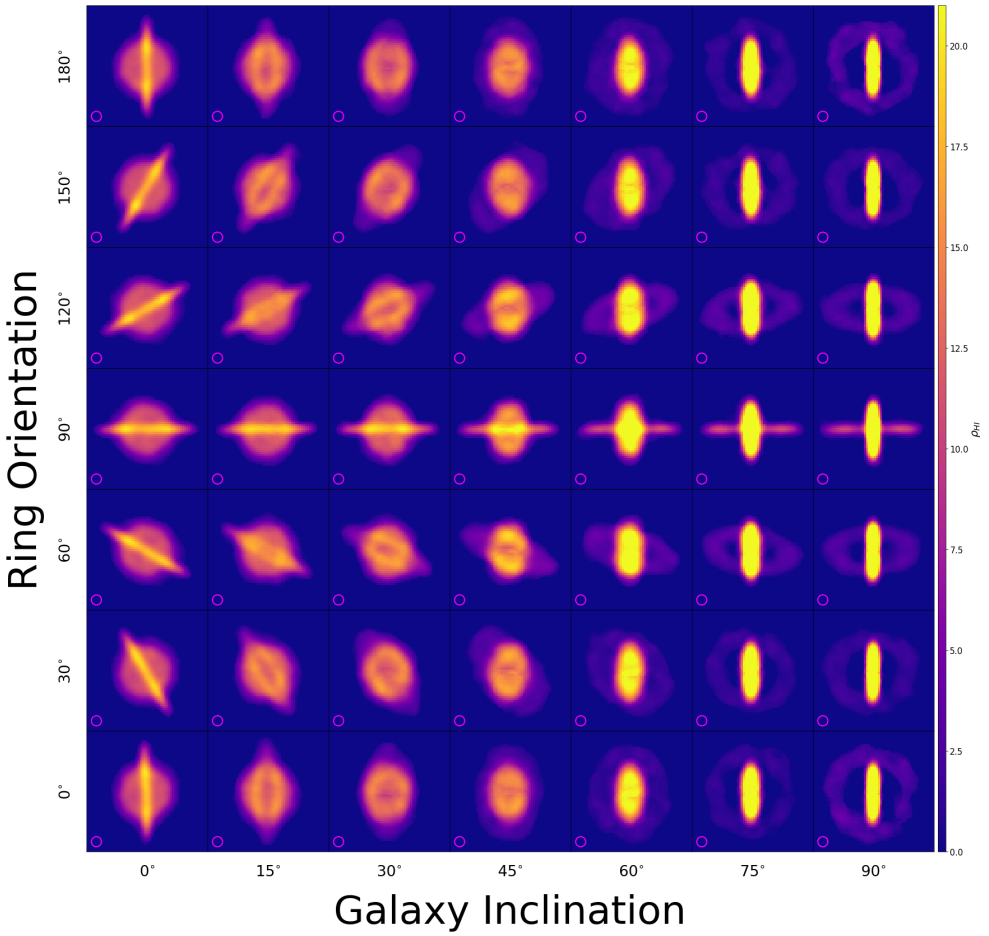

Figure A.19: Moment zero panel plot for the NGC 6156 model galaxy at a resolution of 10 BA. The colour bar on the y-axis depicts the HI density, ρ_{HI}, in units of $M_{\odot}/pc^2$.

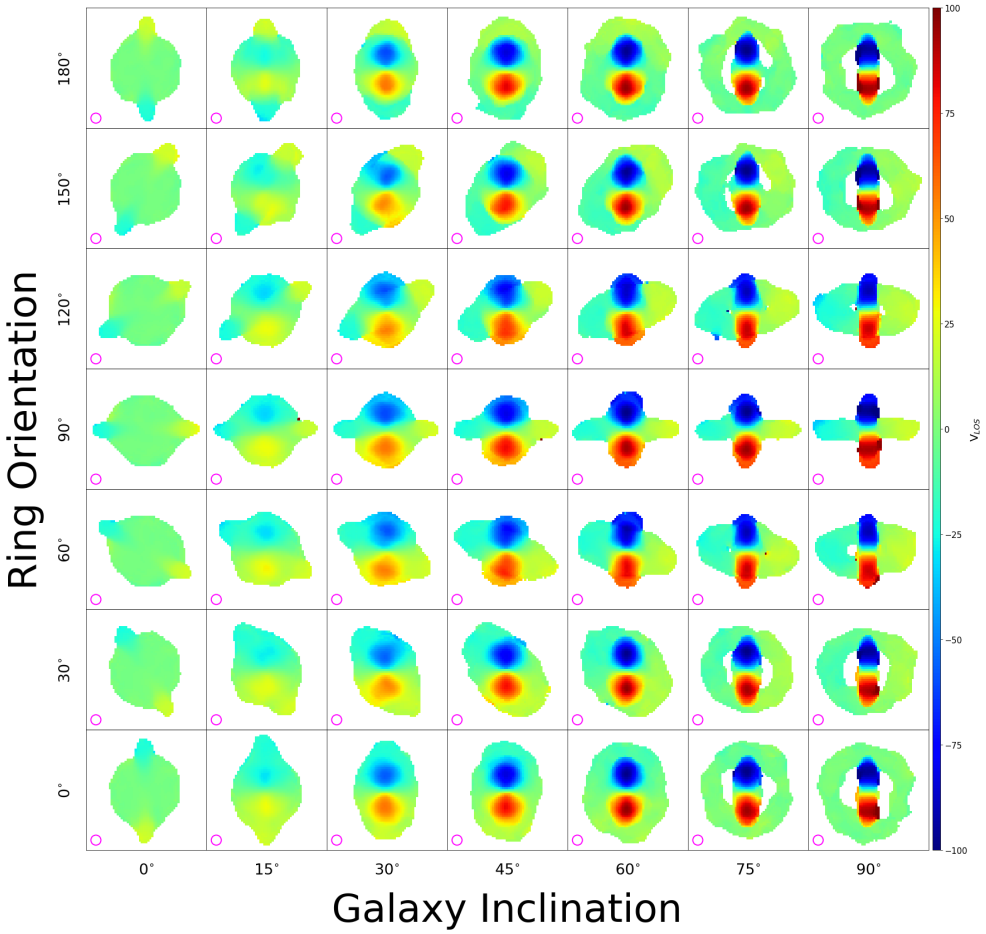

Figure A.20: Moment one panel plot for the NGC 6156 model galaxy at a resolution of 10 BA. The colour bar on the y-axis depicts the line of sight velocity, V_{LOS}, in units of km/s.

B Tentative PDR2 PRG Candidates

The following candidates displayed signatures that were deemed too unreliable to be included in the incidence analysis, primarily due to low resolution. They are presented nonetheless to demonstrate some of the challenges that accompany PRG identification in HI surveys.

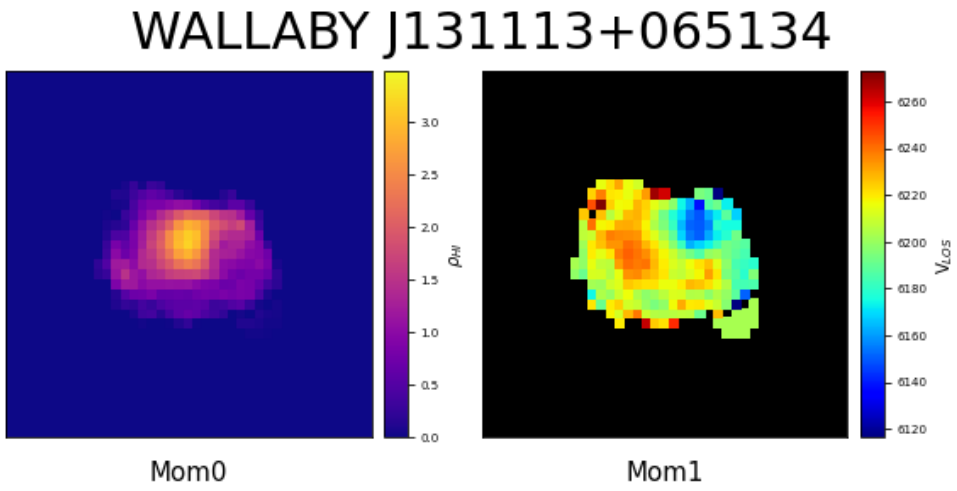

Figure B.1: WALLABY J131113+065134 detected at a resolution of ∼3.5 BA.

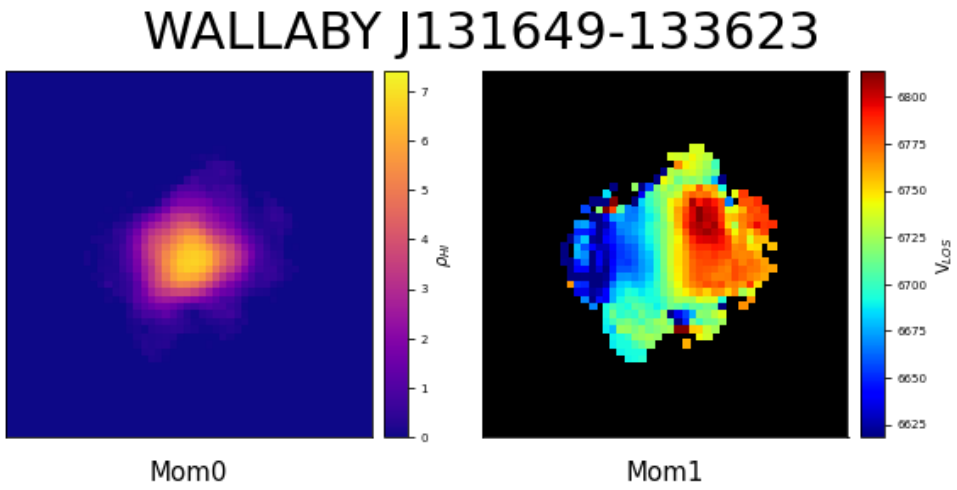

Figure B.2: WALLABY J131649-133623 detected at a resolution of ∼3.5 BA.

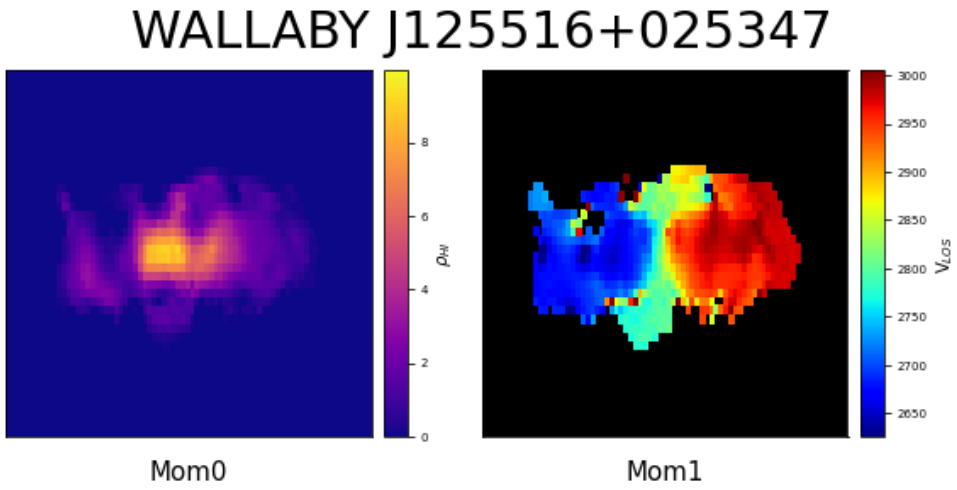

Figure B.3: WALLABY J125516+025347 detected at a resolution of ∼9 BA.

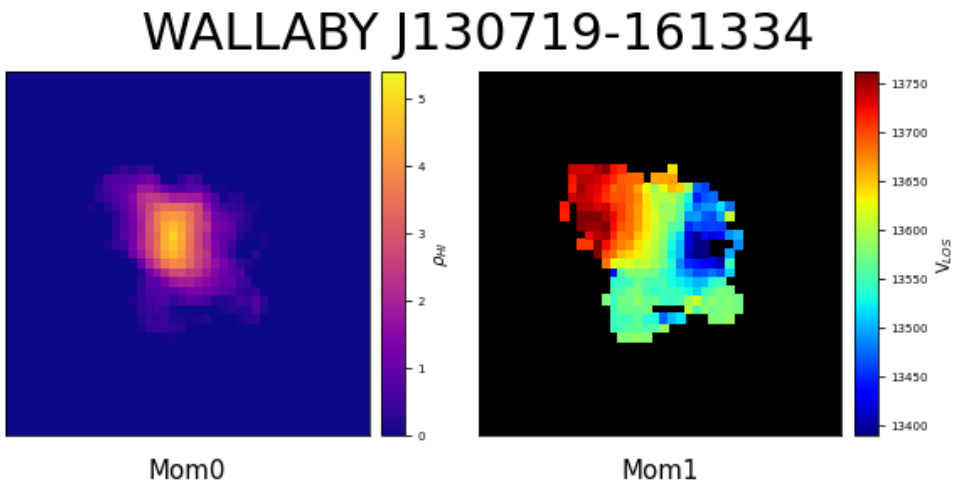

Figure B.4: WALLABY J130719-161334 detected at a resolution of ∼3 BA.

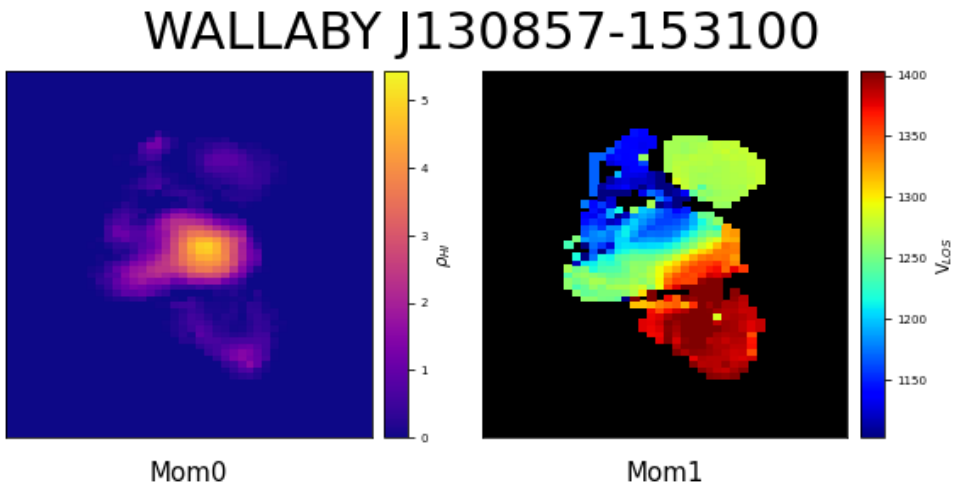

Figure B.5: WALLABY J130857-153100 detected at a resolution of ∼6 BA.

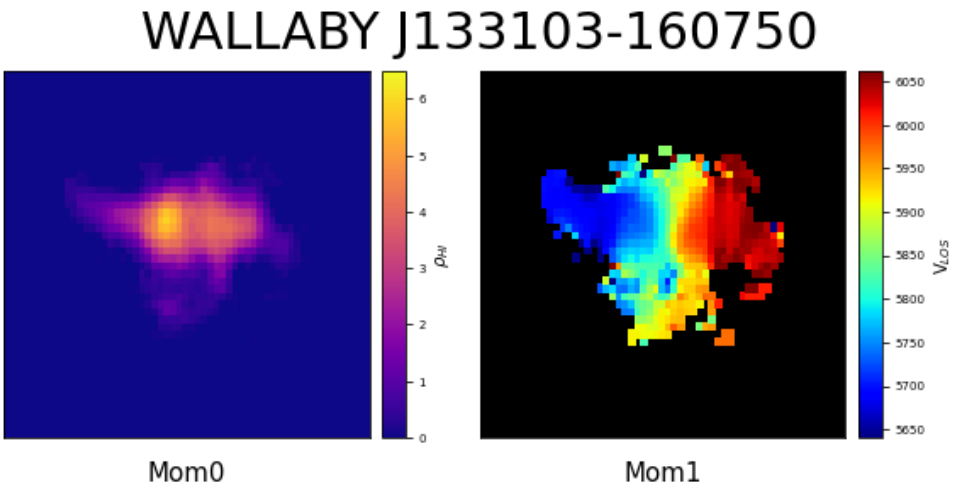

Figure B.6: WALLABY J133103-160750 detected at a resolution of ∼5.5 BA.